Institut für Mathematik
Arbeitsgruppe Semiklassik und Asymptotik

Modelling and simulation of light propagation in non-aged and aged step-index polymer optical fibres

Dissertation
zur Erlangung des akademischen Grades
"doctor rerum naturalium"
(Dr. rer. nat.)
in der Wissenschaftsdisziplin Mathematische Physik

eingereicht an der
Mathematisch-Naturwissenschaftlichen Fakultät
der Universität Potsdam

von
Łukasz Jankowski

Potsdam, den 16. August 2004

Vorsitzender:	Prof. Dr. Matthias Holschneider
Gutachter:	Prof. Dr. Markus Klein (Betreuer) Prof. Dr.-Ing. Werner Daum Prof. Dr.-Ing. Olaf Ziemann
Tag der Einreichung:	16.08.2004
Tag der Verteidigung:	29.10.2004

Acknowledgements

It is a great pleasure to thank the people who made this thesis possible.

I would like to express my deep gratitude to my advisor Prof. Dr. Markus Klein, University of Potsdam. With his enthusiasm, his insight, and his great efforts to explain things clearly and simply, he helped to make mathematics fun for me. He provided encouragement, sound advice and many good ideas. I would also like to thank Prof. Dr. Dieter Neher, University of Potsdam, and Prof. Dr. Olaf Ziemann University of Applied Sciences, Nuremberg, for their kind agreement to supervise this work.

This thesis is a result of my work in the Division S.1 ‘Measurement and Testing Technology; Sensors’ of the Federal Institute for Materials Research and Testing (BAM). I am deeply indebted to Prof. Dr. Werner Daum und Dr. Wolf Czepluch for their constant advice, warm encouragement and for providing me with excellent facilities to pursue my work. I am grateful for their insightful guidance.

I would like to thank my other colleagues from the Laboratory S.13 and Division S.1 for their continuous support and for providing a stimulating and fun environment in which to learn and grow. I am especially grateful to Anilkumar Appajaiah for numerous discussions of chemical aspects of POF aging.

I wish to thank all friends who supported me during those years, for their unselfish help and kindness.

Finally, I thank my family, especially my wife Dorota, parents and brothers. Without their love, nothing would have been possible. To them I dedicate this thesis.

Zusammenfassung

Kunststofflichtwellenleiter (POFs) stellen ein verhältnismäßig neues Medium zur optische Datenkommunikation über kurzen Strecken dar (bis zu einigen hundert Metern). Sie arbeiten im sichtbaren Wellenlängenbereich des elektromagnetischen Spektrums und werden auch für Beleuchtung und für Sensor-Anwendungen verwendet.

Während ihrer Einsatzdauer unterliegen POFs unterschiedlichen Arten von Umweltbeanspruchungen, hauptsächlich durch hohe Temperatur, hohe Feuchtigkeit und mechanischen Belastungen. Zahlreiche experimentelle Forschungen beschäftigten sich mit der standardisierten Prüfung der Zuverlässigkeit von im Handel erhältlichen Fasern. Jedoch gab es bisher wenig Erfolg bei der Bemühung, zwei grundlegende optische Erscheinungen, Absorption und Streuung, die die Lichtausbreitung in Fasern stark beeinflussen, zu verstehen und praktisch zu modellieren: Diese beiden Effekte beschreiben nicht nur die Qualität neuer Fasern, sondern sie werden auch stark durch die Alterungsprozess beeinflusst.

Der Hauptzweck dieser Doktorarbeit war es, ein praktisch verwendbares und theoretisch gut fundiertes Modell der Lichtausbreitung in nicht gealterten und gealterten POFs zu entwickeln und es durch optische Experimente zu verifizieren. Dabei wurden anwendungsorientierte Aspekte mit theoretischer POF-Modellierung kombiniert.

Die Arbeit enthält die erste bekannte Anwendung der Wellenanalyse zur Untersuchung der winkelabhängigen Eigenschaften der Streuung. Die Resultate der numerischen Beispiele stimmen mit den experimentell beobachteten Ergebnissen überein. Der Gebrauch der Wellenoptik war erforderlich, weil die vereinfachende Anwendung der geometrischen Optik zu einer den experimentellen Ergebnissen widersprechenden Winkelabhängigkeit führt. Die Resultate der Wellenanalyse wurden ausserdem dazu verwendet, ein generelles POF-Modell zu entwickeln, das auf dem Strahlverfolgungsverfahren basiert.

Für die praktischen Experimente wurden mehrere POF-Proben unterschiedlicher Hersteller künstlich gealtert, indem sie bis 4500 Stunden bei 100 °C gelagert wurden (ohne Feuchtekontrolle). Die Parameter der jeweiligen Simulationen wurden mittels einer systematischen Optimierung an die gemessen optischen Eigenschaften der gealterten Proben angeglichen. Die erreichte Übereinstimmung ist besser als in bisher vorliegenden Untersuchungen und bestätigt die Verwendbarkeit des Modells. Die Resultate deuten an, dass der Übertragungsverlust der gealterten Fasern in den ersten Tagen und Wochen der Alterung am stärksten durch eine wesentliche physikalische Verschlechterung der Kern-Mantel-Grenzfläche verursacht wird. Chemische Effekte des Alterungsprozesses scheinen im Faserkernmaterial zuerst nach einigen Monaten aufzutreten. Als Nebeneffekt dieser Arbeit wurde ein Kalibrierung- und Qualitätseinschätzungsverfahren für CCD-Kameras entwickelt.

Abstract

This thesis discusses theoretical and practical aspects of modelling of light propagation in non-aged and aged step-index polymer optical fibres (POFs). Special attention has been paid in describing optical characteristics of non-ideal fibres, scattering and attenuation, and in combining application-oriented and theoretical approaches. The precedence has been given to practical issues, but much effort has been also spent on the theoretical analysis of basic mechanisms governing light propagation in cylindrical waveguides.

As a result a practically usable general POF model based on the raytracing approach has been developed and implemented. A systematic numerical optimisation of its parameters has been performed to obtain the best fit between simulated and measured optical characteristics of numerous non-aged and aged fibre samples. The model was verified by providing good agreement, especially for the non-aged fibres. The relations found between aging time and optimal values of model parameters contribute to a better understanding of the aging mechanisms of POFs.

List of publications with regard to the present work

[1] L. Jankowski, *Explanation and modelling of angle-dependent scattering in polymer optical fibres*, Proceedings of the 13th POF-IC, Nuremberg 2004, pp. 195-202.

[2] A. Appajaiah, V. Wachtendorf, L. Jankowski, *Chemiluminescence Investigation of High Temperature and Humidity Aging of PMMA Based Polymer Optical Fibres (POF)*, Proceedings of the 12th POF-IC, Seattle 2003, pp. 152-155.

[3] L. Jankowski, A. Appajaiah, C.-A. Bunge, J. Zubia, *Modelling of Light Propagation Through Aged and Non-Aged POFs*, Proceedings of the 12th POF-IC, Seattle 2003, pp. 148-151.

[4] L. Jankowski, *Calibration procedure for low-end CCD cameras*, Proceedings of the TEST-IC, Nuremberg 2003, pp. 255-260.

[5] L. Jankowski, *Reliable measurements of POFs' optical properties with a low-end CCD camera*, Proceedings of the 11th POF-IC, Tokyo 2002, pp. 251-254.

[6] A. Appaiajah, L. Jankowski, *A review on aging or degradation of polymer optical fibres – Polymer chemistry and mathematical approach*, Proceedings of the 10th POF-IC, Amsterdam 2001, pp. 317-324.

List of important symbols

α	illumination angle
α_{max}	acceptance angle
α_{out}	output angle
β	relative wavenumber of a mode
$d(r,\varphi,z)$	refractive index perturbation
γ	propagation angle
g	Green's function of an ideal cylindrical waveguide
j_m	radial component of a modal field
k	free-space wavenumber
λ	free-space wavelength
m	azimuthal order number of a mode
$n(r)$	unperturbed refractive index profile
$n_p(r,\varphi,z)$	perturbed refractive index profile
n_0	refractive index of fibre's core
n_1	refractive index of fibre's clad
NA	numerical aperture
Ω	perturbation region
R	fibre radius
R_0	radius of the perturbation region
τ	transverse mode parameter
u	scalar field propagating in a waveguide
u_{inc}	incident field
u_{scat}	scattered field
V	normalised frequency of a fibre
w	fibre modal parameter
w_0	core modal parameter
w_1	clad modal parameter
z_0	length of the perturbation region

Contents

1 Introduction

Polymer optical fibres (POFs) are a new emerging medium for short-range optical data communication (up to a few hundred meters) in the visible region of the spectrum. POFs are also widely used for lighting and for sensor applications.

As a safe, inexpensive and reliable data transmission medium POFs are foremost used by the automotive industry, for home and office networks, and for in-device data transmission and control [58, 59]. Although their relatively high attenuation (approx. 150 dB/km) does not allow long-distance transmissions, they are in many other aspects (flexibility, low costs of production and wiring, ease of handling) in short-range applications superior to silica fibres.

In course of use POFs are subjected to different types of environmental stresses, mainly high temperature, humidity and mechanical stress. Great amount of experimental research has already been done to standardise, experimentally test and assess the durability of commercially available fibres [10, 26, 32, 48-56]. However, little effort has been directed towards understanding and practical modelling of two main optical mechanisms not occurring in idealised fibres but affecting light propagation in a real fibre: attenuation and scattering. Both represent the non-ideality not only for new fibres, but are also strongly involved in their aging process and thus critical for fibre's optical properties. Respective researches are important for developing more efficient fibre test methods and for assessing fibre performance under stress.

There has been much theoretical research devoted to fibre optics and wave-analysis of cylindrical waveguides [2, 28, 29, 30]. Nevertheless, it has been rarely rigorous in its mathematical contents. The major flaw seems to be the lack of conditions guaranteeing uniqueness of the solution to the scalar wave equation on a cylindrical fibre, a problem solved for open-space and a spherical wave by Rellich [25, 9]. On the other hand, results obtained in such theoretical investigations have been rarely systematically verified against real fibre measurement data.

There has also been much theoretical [1, 2, 62-67] but very little application-oriented analysis of scattering induced by small-size random irregularities of the refractive index, which is always present in real fibres, especially those subjected to environmental stress and aged. No basic analysis of angular characteristics of this scattering is known, an often met problem in analysis of scattering in open-space geometry but hardly tractable in the case of cylindrical waveguides with their not obvious relation between mode and its illumination, propagation or radiation angles. Analysis based on geometric optics and raytracing, although often referred to, cannot, contrary to expectations, explain some experimentally observed angular characteristics of scattering, thus the use of a constant [42-46, 60] or purely phenomenological relations [16, 41].

Therefore the primary task of this Ph.D. work is to develop a practically usable and theoretically well-rooted model of light propagation in POFs, to investigate the influence of aging effects on it, and to verify it by optical experiments. To achieve a more general understanding of the POF aging process, parallel to this work a Ph.D. thesis of another BAM employee, A. Appajaiah, is prepared, it investigates chemical aspects of aging on the same and similar POF samples [17, 33-36].

Now the outline of the following thesis will be given in respect to its essential parts:

In Part 2.1 of Chapter 2 the scalar wave equation is solved for the case of a cylindrical waveguide. The uniqueness of the solution (i.e. the counterpart of Rellich's radiation condition [25, 9]) is stated without proof as a hypothesis. The representation theorem of Alexandrov and Ciraolo [2] is stated and used to define the relations between illumination angle, excited modes and output angle. Wave analysis of scattering processes in 2D slab waveguides of Magnanini and Santosa [8] is expanded in Part 2.1.4 to 3D cylindrical waveguides. Convergence of a critical series of this part, the one representing the scattered field, is stated as a hypothesis only. Appendix A4 contains considerations concerning a possible proof.

Part 2.2 of Chapter 2 describes the geometric optics approach to fibre modelling and introduces raytracing model with mechanisms mostly absent in the previous research:

- scattering mechanism (Part 2.2.2) based on the results of the theoretical investigations of Part 2.1 and the numerical simulations of scattering intensity in dependence on illumination angle (reported in Appendix A2);
- implemented Fresnel reflection law (Part 2.2.3) in the form of a random choice between reflection and transmission for each ray incident on the core-clad interface. This mechanism, although intuitively obvious, requires astonishingly much effort to prove its validity.

Part 2.3 of Chapter 2 introduces two basic characteristics of an optical fibre: far-field profiles and near-field profiles.

Chapter 3 describes the software developed to implement the raytracing model of Part 2.2. It includes simulation software as well as the software allowing comparison of simulated and measured far-field profiles and semi-automatic parameter optimisation.

Fibres used for practical investigations, their technical specifications, aging conditions and preparation of the samples for further measurements are described in Chapter 4. Fibres from three manufacturers have been used. The high temperature aging process (100 °C/<<50 % RH (dry heat)) has been selected; the fibres used in further investigations were subjected to six different aging times (ranging from no aging, i.e. 0 h, up to half a year, i.e. approx. 4500 h in oven).

Chapter 5 discusses the setup used for far-field profile measurements. Part 5.3 describes the developed procedure, necessary for quality assessment and calibration of CCD cameras [14].

Chapter 6 discusses the measurement process and the procedure for far-field profile extraction from obtained measurements. Part 6.4 presents sample measurement results: far-field profiles of non-aged and aged fibres.

The results of the parameter optimisation by comparison of simulated and measured far-fields are presented in Chapter 7. This systematic approach to model validation and parameter fitting can be considered superior to earlier research, because here:

- Both bulk and interface attenuation coefficients are used to trace separately aging of the bulk material and physical degradation of the core-clad interface.
- Fibres of different lengths are measured and compared. The amount of the scattering understandably depends on fibre length, thus using fibre samples of different length allows for significantly more control over the scattering parameters and ensures model validity for not only one fibre length.
- Semi-automatic numerical optimisation procedure is applied.

Appendix A2 contains the results of numerical wave analysis of two sample cylindrical waveguides. It directly uses the notation and results of Part 2.2. For both cases it was found that scattering intensity clearly decreases with increasing illumination angle, an explanation for the relations experimentally observed before. This is a pure wave-effect and probably cannot be satisfactorily explained on the basis of geometric optics and simple raytracing model only, which suggest the opposite scattering – angle relation.

Appendix A3 shows several graphs comparing simulated and measured far-field profiles of fibres used in this research.

2 Modelling of light propagation in POF

In this chapter two most important approaches used for analysis and modelling of optical fibres will be discussed: the wave optics (Part 2.1) and the raytracing approach (Part 2.2). We will concentrate mainly on the property of an optical fibre that is most aging-related, i.e. scattering and, in the case of the raytracing approach, also attenuation (see also Part 4.1). The fibre simulations (Chapter 7, Appendix A3) performed within this research are made with self-implemented software (Chapter 3) using the raytracing model described here. At the end of this chapter we will discuss basic measurable characteristics of an optical fibre: near- and far-field profiles (Part 2.3).

For the analysis of light propagation in optical fibres both the Cartesian and the cylindrical coordinate systems will be used (*Fig. 2.1*).

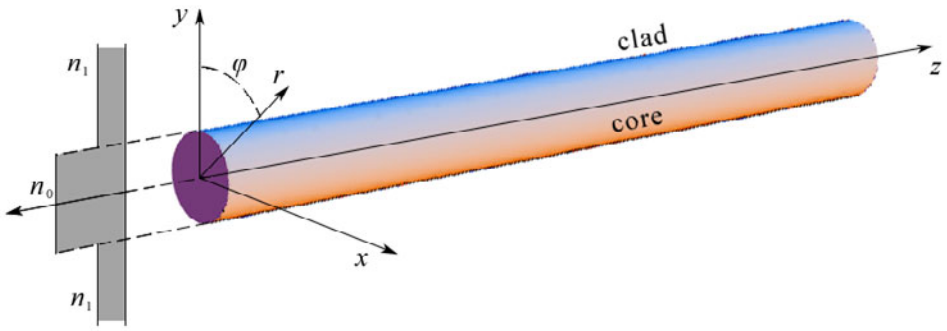

Fig. 2.1 *The nomenclature for describing the optical fibre. The fibre axis lies along the z axis of both Cartesian and cylindrical coordinate systems. The clad will be assumed to extend infinitely, as in Eq. (2.16), or to end at some finite distance, as in Eq. (2.74), where air of refractive index 1 begins.*

2.1 Wave-optics model

Wave approach takes into account the wave nature of propagating light and requires solving the vector wave equation or its simplified version, the scalar wave equation. As the scalar wave equation is generally considered valid (so called *weak guidance approximation*) and broadly used for optical fibres modelling due to small variations of a refractive index in a typical fibre, in this analysis only the scalar description of propagating fields will be used.

Within the wave-optics approach, light propagating in an optical waveguide is described in terms of a set of discrete solutions of wave equations (vector or scalar), called *guided modes*, and a set of continuous solutions, called *radiating modes*. Those modes (in the scalar case considered here) are eigenvalue functions of the scalar wave equation and each finite energy solution of this equation is a unique superposition of guided and radiating modes, as the representation theorem of Alexandorv and Ciraolo [2] states (Part 2.1.3.1).

In this Part 2.1 we will solve the scalar wave equation (Part 2.1.2), cite the representation theorem (Part 2.1.3.1), relate the inclination of an input beam to the excitation of particular modes (Part 2.1.3.2) and finally discuss scattering of propagating light between modes

caused mainly by perturbations of the refractive index of the waveguide (Part 2.1.4). The obtained angle-dependence of the scattering intensity will then be used in the raytracing approach (Part 2.2).

As it is common in the context of the wave analysis, mainly the term 'waveguide' instead of 'fibre' will be used in this part.

2.1.1 Maxwell's, vector and scalar wave equations

Propagation of an electromagnetic field is exactly described by the set of *Maxwell's equations* [1, 4]. For the case of non-magnetic materials, which normally constitute an optical waveguide, and assuming an implicit time dependence $exp(-i\omega t)$, they are expressible using MKS units in the following form [1]:

$$\begin{aligned} &\nabla \cdot \left(n^2 \mathbf{E}\right) = \frac{\sigma}{\varepsilon_0} \\ &\nabla \times \mathbf{E} = i\left(\frac{\mu_0}{\varepsilon_0}\right)^{\frac{1}{2}} k\mathbf{H} \\ &\nabla \cdot \mathbf{H} = 0 \\ &\nabla \times \mathbf{H} = \mathbf{J} - i\left(\frac{\varepsilon_0}{\mu_0}\right)^{\frac{1}{2}} k n^2 \mathbf{E} \end{aligned} \qquad (2.1)$$

where $\mathbf{E}(x,y,z)$ and $\mathbf{H}(x,y,z)$ are the electric and magnetic field vectors, $\mathbf{J}$ is the current density, σ is the charge density, μ_0 and ε_0 are respectively the permeability and permittivity (dielectric constant) of free space and the free-space wavenumber k is related to the wavelength λ of light in free space and to the angular frequency ω by:

$$k = \frac{2\pi}{\lambda} = \frac{\omega}{c} \,. \qquad (2.2)$$

n in Eq. (2.1) is the refractive index of the medium, related to its permittivity ε and the permittivity of free space ε_0 by [1, 4]:

$$\varepsilon = n^2 \varepsilon_0 \,. \qquad (2.3)$$

For the *translationally invariant* waveguides, i.e. for the waveguides with refractive index profiles $n = n(x,y)$ not varying with the distance ***z*** along the waveguide, both electric and magnetic fields of the waveguide are according to [1] expressible as superpositions of fields with the following separable forms:

$$\begin{aligned} \mathbf{E}(x, y, z) &= \mathbf{e}(x, y)\exp(i\beta kz) \\ \mathbf{H}(x, y, z) &= \mathbf{h}(x, y)\exp(i\beta kz) \end{aligned}, \qquad (2.4)$$

where β is the relative wavenumber and βk is the propagation constant. After decomposing the fields into their longitudinal and transverse components

$$\begin{aligned}\mathbf{E}(x,y,z) &= \left[\mathbf{e_t}(x,y)+\hat{\mathbf{z}}e_z(x,y)\right]\exp(i\beta kz)\\ \mathbf{H}(x,y,z) &= \left[\mathbf{h_t}(x,y)+\hat{\mathbf{z}}h_z(x,y)\right]\exp(i\beta kz)\end{aligned}, \tag{2.5}$$

where $\hat{\mathbf{z}}$ is the unit vector parallel to the waveguide axis. Substituting those representations into the source-free Maxwell's equations (i.e. with $\mathbf{J}\equiv 0$, $\sigma\equiv 0$) we can relate other field components to the transverse electric field $\mathbf{e}_t$ [1]:

$$\begin{aligned} e_z &= \frac{i}{\beta}\left(\nabla\mathbf{e_t}+\mathbf{e_t}\cdot\nabla\ln n^2\right),\\ \mathbf{h_t} &= \left(\frac{\varepsilon_0}{\mu_0}\right)^{\frac{1}{2}}\frac{1}{k}\hat{\mathbf{z}}\times\left(\beta k\mathbf{e_t}+i\nabla e_z\right),\\ h_z &= \frac{i}{\beta}\nabla\mathbf{h_t}. \end{aligned} \tag{2.6}$$

Eliminating either electric or magnetic field from Eq. (2.1), the *inhomogeneous* vector wave equations [1] can be obtained:

$$\begin{aligned}\Delta\mathbf{E}+n^2k^2\mathbf{E} &= -\nabla\left(\mathbf{E}\cdot\nabla\ln n^2\right)-i\left(\frac{\mu_0}{\varepsilon_0}\right)^{\frac{1}{2}}\left(k\mathbf{J}+\frac{1}{k}\nabla\left(\frac{\nabla\cdot\mathbf{J}}{n^2}\right)\right),\\ \Delta\mathbf{H}+n^2k^2\mathbf{H} &= \left(\nabla\times\mathbf{H}-\mathbf{J}\right)\times\nabla\ln n^2-\nabla\times\mathbf{J}.\end{aligned} \tag{2.7}$$

With no sources present, both fields satisfy the *homogenous* vector wave equation, obtained from Eq. (2.7) by setting $\mathbf{J}\equiv 0$:

$$\begin{aligned}\Delta\mathbf{E}+n^2k^2\mathbf{E} &= -\nabla\left(\mathbf{E}\cdot\nabla\ln n^2\right)\\ \Delta\mathbf{H}+n^2k^2\mathbf{H} &= \left(\nabla\times\mathbf{H}\right)\times\nabla\ln n^2.\end{aligned} \tag{2.8}$$

Solving equations Eq. (2.8) even in the relatively simple case of the step-index waveguide profile is difficult [1, 6] and only few other profiles are known to have exact solutions [1]. Pronounce simplification is possible, if variations of the waveguide refractive index Δn are considered enough small (like in the case of POF with $\Delta n \approx 6$ % at the core-clad interface) to neglect the right-hand-side of Eq. (2.8), i.e. assume

$$\nabla\ln n^2 = 0. \tag{2.9}$$

Optical waveguides with $\Delta n \approx 0$ and consequently with $n_0 \approx n_1$ are called *weakly guiding* [5], although, as Snyder and Love in [1, page 281] state, *the terminology is somewhat misleading since both strong guidance and total containment of light within the core are possible*. Both Cartesian coordinates of the transverse component $\mathbf{e}_t$ of the electric field propagating in such waveguide may be found by solving the *scalar wave equation*:

$$\Delta u+n^2k^2u = 0, \tag{2.10}$$

where u denote one of the Cartesian coordinates of $\mathbf{e}_t$. The longitudinal components $e_z \approx 0$ and $h_z \approx 0$ (i.e. all fields are TEM waves) due to the weak guidance approximation, the transversal component $\mathbf{h}_t$ of the magnetic field may be computed using the formulae Eq. (2.6).

For a detailed discussion of the derivation of the weak guidance approximation and the relations between solutions of Eq. (2.8) and Eq. (2.10) see Snyder and Love [1, Chapter 32 and 33], and Gloge [5].

2.1.2 Modes

We will look for basic, simply expressible solutions of Eq. (2.10), called modes. As the representation theorem of Alexandrov and Ciraolo [2] states, each finite energy field propagating in a weakly guiding waveguide is a unique superposition of such modes.

Rewriting the equation Eq. (2.10) in cylindrical coordinates (r, φ, z) we obtain:

$$\frac{\partial^2}{\partial z^2}u + \frac{1}{r}\frac{\partial}{\partial r}\left(r\frac{\partial u}{\partial z}\right) + \frac{1}{r^2}\frac{\partial^2}{\partial r^2}u + k^2 n^2 u = 0 \quad . \tag{2.11}$$

We will look for solutions in separated variables only:

$$u(r,\varphi,z) = \exp(i\beta kz)\cdot\exp(im\varphi)\cdot j_m\left(r,\beta^2\right), \tag{2.12}$$

where j_m: $\mathbf{R}\to\mathbf{R}$ is the radial component of the propagating mode depending on β^2, β is the relative wavenumber of the mode (βk is the mode propagation constant) and $m\in\mathbf{Z}$ due to the conservation condition. After substituting Eq. (2.12) into Eq. (2.11) and eliminating the variables φ and z we obtain:

$$j_m'' + \frac{1}{r}j_m' + j_m\left[k^2\left(n^2-\beta^2\right) - \frac{m^2}{r^2}\right] = 0 \quad . \tag{2.13}$$

For notational clarity from now on τ will be used for β^2:

$$\tau := \beta^2 \ . \tag{2.14}$$

The form of the general solution to Eq. (2.13) depends on the relation between n^2 and $\beta^2 = \tau$:

$$j_m(r,\tau) = \begin{cases} a_m(\tau)\cdot J_m\left(kr\sqrt{n^2-\tau}\right) + b_m(\tau)\cdot Y_m\left(kr\sqrt{n^2-\tau}\right) & ,\ \tau < n^2 \\ a_m(\tau)\cdot r^{-|m|} + b_m(\tau)\cdot r^{|m|} & ,\ \tau = n^2,\ |m| > 0 \\ a_m(\tau)\cdot \ln r & ,\ \tau = n^2,\ m = 0 \\ a_m(\tau)\cdot I_m\left(kr\sqrt{\tau-n^2}\right) + b_m(\tau)\cdot K_m\left(kr\sqrt{\tau-n^2}\right) & ,\ \tau > n^2 \end{cases} \tag{2.15}$$

where J_m and Y_m are m-th order real Bessel functions of the first and second kind, I_m and K_m are m-th order real modified Bessel functions of the first and second kind and $a_m(\tau)$, $b_m(\tau)$ are arbitrary but real coefficients.

In the case of the step-index waveguide two values of the refractive index must be considered: n_0 for the core and n_1 for the infinitely extended clad:

$$n(r) = \begin{cases} n_0 & , r \in [0, R\,] \\ n_1 < n_0 & , r \in (R, \infty), \end{cases} \tag{2.16}$$

where R is the radius of the waveguide. Thus, the equation Eq. (2.13) has to be solved separately for the core and separately for the clad. The general solution for the whole waveguide, across its core and clad, has then to be expressed as:

$$j_m(r,\tau) = \begin{cases} {}_0 j_m(r,\tau) & , r \in [0, R\,] \\ {}_1 j_m(r,\tau) & , r \in (R, \infty), \end{cases} \tag{2.17}$$

where ${}_0j_m$ and ${}_1j_m$ are the solutions of Eq. (2.13) in the core and in the clad, respectively. Both have to satisfy the following conditions:

$$\begin{aligned} {}_0 j_m(R,\tau) &= {}_1 j_m(R,\tau), \\ {}_0 j'_m(R,\tau) &= {}_1 j'_m(R,\tau), \\ {}_0 j_m &\text{ and } {}_1 j_m \text{ are bounded.} \end{aligned} \tag{2.18}$$

First two of them are boundary conditions; the continuity of j_m and its first derivative across the core-clad interface follows directly from Eq. (2.10) and Eq. (2.16). Third condition is an obvious physical requirement. Functions building the solutions Eq. (2.15) are bounded or unbounded on $[0, R\,]$ and (R, ∞) according to *Table 2.1*:

Table 2.1 *Properties of the solutions to equation Eq. (2.13) in waveguide's core and clad.*

	bounded	*unbounded*
$r \in [0, R\,)$	$J, I, r^{\lvert m\rvert}$	$Y, K, r^{-\lvert m\rvert}, \lvert m\rvert>0$
$r \in [R, \infty)$	$J, K, Y, r^{-\lvert m\rvert}$	$I, r^{\lvert m\rvert}, \lvert m\rvert>0$

For notational clarity we introduce the following modal parameters:

$$\begin{aligned} w_0 &:= k\sqrt{\left|n_0^2 - \tau\right|}, \\ w_1 &:= k\sqrt{\left|n_1^2 - \tau\right|}, \\ w &:= k\sqrt{\left|n_0^2 - n_1^2\right|}, \\ V &:= wR. \end{aligned} \tag{2.19}$$

Note that V is a mode-independent waveguide parameter (often called waveguide's *normalised frequency*), for a typical POF $V \approx 4000$. In the literature often not τ but w_0^2 is treated as an independent, mode-specific variable. This approach lacks a bit of the conceptual clarity of the relative wavenumber β, but leads to simpler mode-angle relation and occasionally will be used also here.

Taking into account the third requirement from Eq. (2.18), the data in *Table 2.1*, the relations between n_0^2, n_1^2, $\tau = \beta^2$ and combining separate solutions Eq. (2.15) for the core and the clad, potential solutions to Eq. (2.13) may be written as:

(2.20)

for $\tau < n_1^2$	$j_m(r,\tau) = \begin{cases} J_m(w_0 r) & , r \in [0, R] \\ a_m(\tau)\cdot J_m(w_1 r) + b_m(\tau)\cdot Y_m(w_1 r) & , r \in (R, \infty), \end{cases}$	
for $\tau = n_1^2$	$j_m(r,\tau) = \begin{cases} J_m(w_0 r) & , r \in [0, R] \\ a_m(\tau)\cdot r^{-\lvert m\rvert} & , \lvert m\rvert > 0 \\ & , r \in (R, \infty), \end{cases}$	
for $\tau \in (n_1^2, n_0^2)$	$j_m(r,\tau) = \begin{cases} J_m(w_0 r) & , r \in [0, R] \\ b_m(\tau)\cdot K_m(w_1 r) & , r \in (R, \infty), \end{cases}$	
for $\tau = n_0^2$	$j_m(r,\tau) = \begin{cases} r^{\lvert m\rvert} & , r \in [0, R] \\ b_m(\tau)\cdot K_m(w_1 r) & , r \in (R, \infty), \end{cases}$	
for $\tau > n_0^2$	$j_m(r,\tau) = \begin{cases} I_m(w_0 r) & , r \in [0, R] \\ b_m(\tau)\cdot K_m(w_1 r) & , r \in (R, \infty), \end{cases}$	

where $a_m(\tau)$, $b_m(\tau)$ are arbitrary real coefficients.

All potential solutions Eq. (2.20) have to be checked against the first two requirements of Eq. (2.18), the boundary conditions. It turns out, that:

- For $\tau \geq n_0^2$: There are no propagating modes, i.e. the boundary conditions Eq. (2.18) are satisfied by $j_m(r,\tau)$ for none $\tau \geq n_0^2$ and none $b_m(\tau)$.
- For $\tau \in (n_1^2, n_0^2)$: For each $m \in \mathbf{Z}$ there is a discrete (maybe empty) set of solutions, the solutions exist if and only if $\tau \in \left\{ \tau_k^m \middle| k = 0,1,\ldots,P_m \right\}$ and have the following form:

(2.21)
$$j_m(r,\tau_k^m) = \begin{cases} J_m(w_0 r) & , r \in [0, R] \\ \dfrac{J_m(w_0 R)}{K_m(w_1 R)} K_m(w_1 r) & , r \in (R, \infty), \end{cases}$$

where $\left\{ \tau_k^m \middle| k = 0,1,\ldots,P_m \right\}$ is the set of the solutions of the following equation:

(2.22)
$$w_0 R \frac{J_{m+1}(w_0 R)}{J_m(w_0 R)} = w_1 R \frac{K_{m+1}(w_1 R)}{K_m(w_1 R)}.$$

where w_0 and w_1 are defined in Eq. (2.19) and $w_0^2 R^2 + w_1^2 R^2 = V^2$. Note that all the functions $\sqrt{r} \cdot j_m\left(r, \tau_k^m\right)$ are in $L^2(0,\infty)$ and the powers carried by the corresponding modes Eq. (2.12) may be computed as:

$$2\pi \int_0^\infty r \cdot j_m^2\left(r, \tau_k^m\right) dr = \tag{2.23}$$

$$= \frac{R^2 \pi}{K_m^2(w_1 R)} \left[J_m^2(w_0 R) K_{m-1}(w_1 R) K_{m+1}(w_1 R) - K_m^2(w_1 R) J_{m-1}(w_0 R) J_{m+1}(w_0 R) \right].$$

- For $\tau = n_1^2$: For each $|m| > 0$ the existence of the solution depends on the identity

$$wR \frac{J_{m+1}(wR)}{J_m(wR)} = m + |m|. \tag{2.24}$$

The solution exists if and only if the identity holds, and then it has the form:

$$j_m\left(r, n_1^2\right) = \begin{cases} J_m(wr) & , r \in [0, R] \\ R^{|m|} J_m(wR) \cdot r^{-|m|} & , r \in (R, \infty). \end{cases} \tag{2.25}$$

The function $\sqrt{r} \cdot j_m\left(r, n_1^2\right)$ belongs to $L^2(0, \infty)$ if and only if $|m| > 1$ and then the corresponding mode Eq. (2.12) carries finite power:

$$2\pi \int_0^\infty r \cdot j_m^2\left(r, n_1^2\right) dr = R^2 \pi \frac{|m|}{|m|-1} J_m^2(wR). \tag{2.26}$$

Note that in this case $w_0 = w$.

- For $\tau < n_1^2$: For each $m \in \mathbf{Z}$ and for each $\tau \in \left(-\infty, n_1^2\right)$ there exists a solution to Eq. (2.13) with a form listed in Eq. (2.20):

$$j_m(r, \tau) = \begin{cases} J_m(w_0 r) & , r \in [0, R] \\ a_m(\tau) \cdot J_m(w_1 r) + b_m(\tau) \cdot Y_m(w_1 r) & , r \in (R, \infty). \end{cases} \tag{2.27}$$

Using the identity Eq. (A1.1) we can obtain the formulae for $a_m(\tau)$ and $b_m(\tau)$:

$$a_m(\tau) = \frac{1}{2} R\pi \left[w_0 J_{m+1}(w_0 R) Y_m(w_1 R) - w_1 J_m(w_0 R) Y_{m+1}(w_1 R) \right],$$

$$b_m(\tau) = \frac{1}{2} R\pi \left[w_1 J_{m+1}(w_1 R) J_m(w_0 R) - w_0 J_m(w_1 R) J_{m+1}(w_0 R) \right]. \tag{2.28}$$

Functions $\sqrt{r} \cdot j_m\left(r, n_1^2\right)$ are not in $L^2(0, \infty)$.

The existence of the solutions to Eq. (2.13) in dependence on τ can be schematically summarised as on the *Fig. 2.2*.

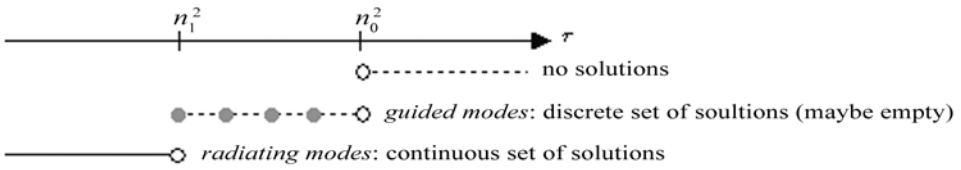

Fig. 2.2 *Diagram of solutions to the radial component of a scalar field propagating in a waveguide, equation Eq. (2.13).*

According to the terminology used on *Fig. 2.2*, modes with the radial component j_m of the form either Eq. (2.21) or Eq. (2.25) with $|m| > 1$, so propagating with $\tau \in [n_1^2, n_0^2)$, are called *guided modes*. They decay exponentially in the clad with the radius and carry finite power (for examples see *Fig. A2.4*, *Fig. A2.5* and *Fig. A2.7*). Alexandrov and Ciraolo have proved in [2, Theorem 8.2] the following:

THEOREM 2.1. [2] The total number of guided modes (in all $m \in \mathbf{Z}$) is finite. ■

Modes with the radial component j_m of the form Eq. (2.27), propagating with $\tau < n_1^2$ are called *radiating modes*. Radiating modes extend oscillating with the radius into the clad much farer than guided modes (no exponential decay, for examples see *Fig. A2.6*). As $\sqrt{r} \cdot j_m\left(r, n_1^2\right) \notin L^2(0,\infty)$, finite power propagating in the waveguide may be distributed among radiating modes only continuously.

Note that Eq. (2.12) implies that both guided and radiating modes with positive τ are oscillating with distance z along the waveguide, while radiating modes with $\tau < 0$ exponentially decay or grow, depending on the direction of the propagation. Such exponentially decaying or growing modes are called *evanescent modes*.

For given $m \in \mathbf{Z}$ let $j_{0m}(r, \tau_0)$ and $j_{1m}(r, \tau_1)$ be two different solutions of Eq. (2.13), not both radiating. It can be easily checked that the functions $r^{1/2} j_{0m}(r, \tau)$ and $r^{1/2} j_{1m}(r, \tau)$ are orthogonal: Under the substitution $v_{0m}(r, \tau_0) := r^{1/2} j_{0m}(r, \tau_0)$ and $v_{1m}(r, \tau_1) := r^{1/2} j_{1m}(r, \tau_1)$ equation Eq. (2.13) gives the two following equations:

$$v_{0m}''(r, \tau_0) + v_{0m}(r, \tau_0)\left[k^2\left(n^2 - \tau_0\right) - \frac{m^2 - 0.25}{r^2}\right] = 0,$$

(2.29)

$$v_{1m}''(r, \tau_1) + v_{1m}(r, \tau_1)\left[k^2\left(n^2 - \tau_1\right) - \frac{m^2 - 0.25}{r^2}\right] = 0.$$

Multiplying the first equation by $v_{1m}(r, \tau_1)$, the second by $v_{0m}(r, \tau)$, subtracting the products and integrating the result over $[0,\infty)$ yields:

(2.30) $$k^2\left(n^2 - \tau_1\right) \int_0^\infty v_{0m}(r, \tau_0) \cdot v_{1m}(r, \tau_1)\, dr =$$

$$= \int_0^\infty \left[v_{0m}(r,\tau_0)\cdot v''_{1m}(r,\tau_1) - v''_{0m}(r,\tau_0)\cdot v_{1m}(r,\tau_1) \right] dr =$$

$$= \lim_{\substack{r_0\to 0 \\ r_\infty\to\infty}} \left[v_{0m}(r,\tau_0)\cdot v'_{1m}(r,\tau_1) - v'_{0m}(r,\tau_0)\cdot v_{1m}(r,\tau_1) \right]\Big|_{r=r_0}^{r=r_\infty} =$$

$$= \lim_{r\to\infty} r\cdot \left[j_{0m}(r,\tau_0)\cdot j'_{1m}(r,\tau_1) - j'_{0m}(r,\tau_0)\cdot j_{1m}(r,\tau_1) \right] = 0\,,$$

for the expression in the parenthesis converges to zero quicker than r^{-1}, if at least one of $j_{0m}(r,\tau_0)$ and $j_{1m}(r,\tau_1)$ is not radiating, see Eq. (A1.2).

Example computations and graphs of modal fields for two waveguides with normalised frequency parameter $V = 8$ and $V = 20$ may be found in Appendix A2.1.

2.1.3 Modal representation of an input field

In the previous part we have solved the scalar wave equation in separated variables for the case of a step-index waveguide and obtained the set of basic configurations of the propagating field, called modes. It turns out that each finite-power field propagating in such a waveguide can be uniquely represented as a superposition of modal fields, as the representation theorem of Alexandrov and Ciraolo [2] states. We now will cite the theorem (Corollary 2.4) and use it to obtain the modal representation of the angle-dependent uniform lighting of the fibre input face, in order to approximate the laser lighting used for the measurements of far-field profiles in the experimental part of this work (Chapters 5 and 6). We will also state the assumptions that will allow calculating fibre output far-field out of modal fields.

2.1.3.1 Representation theorem

Alexandrov and Ciraolo, proving in [2] the two following theorems, have showed that the radial components j_m, $m\in\mathbf{Z}$, may be viewed as transform kernels, with the corresponding sets of τ as the transform variable.

THEOREM 2.2. [2] Let $g:\mathbf{R}_+\to\mathbf{C}$ be such a function that $\sqrt{r}\cdot g(r)\in L^2(0,\infty)$. For each $m\in\mathbf{Z}$ the following integral converge:

(2.31) $$G_m(\tau) := \int_0^\infty r\cdot j_m(r,\tau)\cdot g(r)\,dr$$

and there exists a non-decreasing function $\chi_m:\mathbf{R}\to\mathbf{R}$ such that:

(2.32) $$g(r) = \frac{1}{\pi}\int_{-\infty}^{\infty} j_m(r,\tau)\cdot G_m(\tau)\,d\chi_m(\tau).$$

The Parseval identity holds:

$$2\pi\int_0^\infty r\cdot|g(r)|^2\,dr = 2\int_{-\infty}^{\infty}|G_m(\tau)|^2\,d\chi_m(\tau). \tag{2.33}$$

■

THEOREM 2.3. [2] Let $g{:}\mathbf{R}_+\to\mathbf{C}$ be such a function such that $\sqrt{r}\cdot g(r)\in L^2(0,\infty)$ and let $\chi_m{:}\mathbf{R}\to\mathbf{R}$ be the non-decreasing function from Theorem 2.2. Then

$$d\chi_m(\tau) = \frac{1}{2}k^2\pi\frac{d\tau}{a_m^2(\tau)+b_m^2(\tau)} \qquad \text{for} \quad \tau\in\left(-\infty, n_1^2\right). \tag{2.34}$$

For $\tau\in[n_1^2, n_0^2)$ function χ_m is constant between the discontinuity points $\{\tau_k^m \mid k=0,1,...,P_m\}$, where n_1^2 is the first discontinuity point if and only if the equation Eq. (2.24) holds and the rest τ_k^m are the roots of the equation Eq. (2.22). In each discontinuity point τ_k^m function χ_m has a jump r_k^m, where

$$r_k^m := \pi\left(\int_0^\infty r\cdot j_m^2\left(t,\tau_k^m\right)dr\right)^{-1}. \tag{2.35}$$

For $\tau\in[n_1^2, n_0^2)$ function χ_m is constant. Using Eq. (2.34) the formula Eq. (2.32) for the back transform can be rewritten as:

$$g(r) = \frac{1}{\pi}\sum_{k=0}^{P_m} r_k^m\cdot j_m(r,\tau)\cdot G_m(\tau) + \frac{1}{2}k^2\int_{-\infty}^{n_1^2}\frac{j_m(r,\tau)\cdot G_m(\tau)}{a_m^2(\tau)+b_m^2(\tau)}\,d\tau. \tag{2.36}$$

■

Both theorems directly imply the following corollary:

COROLLARY 2.4. Let $u(r,\varphi,z)$ be a finite-power solution of the scalar wave equation Eq. (2.10), Eq. (2.11) with the refractive index n defined in Eq. (2.16), i.e. let for each z

$$2\pi\int_0^{2\pi}\int_0^\infty r\cdot|u(r,\varphi,z)|^2\,dr\,d\varphi < \infty. \tag{2.37}$$

Let $u_m(r, z)$ be the Fourier coefficients of $u(r,\varphi,z)$:

$$u_m(r,z) := \frac{1}{2\pi}\int_0^{2\pi} e^{-im\varphi}u(r,\varphi,z)\,d\varphi. \tag{2.38}$$

Then u at each distance z along the waveguide is the superposition of guided and radiating modes $j_m(r,\tau)$, $m\in\mathbf{Z}$ with weights $G_m(\tau, z)$:

$$u(r,\varphi,z) = \frac{1}{\pi}\sum_{m\in\mathbf{Z}}\exp(im\varphi)\cdot\int_{-\infty}^{\infty} j_m(r,\tau)\cdot G_m(\tau,z)\,d\chi_m(\tau), \tag{2.39}$$

where $d\chi_m(\tau)$ is defined in Eq. (2.34) and Eq. (2.35). The coefficients $G_m(\tau, z)$ contain all z-dependence and are defined by:

$$G_m(\tau, z) := \int_0^\infty r \cdot j_m(r, \tau) \cdot u_m(r, z)\, dr \tag{2.40}$$

and satisfy

$$G_m(\tau, z) = G_m(\tau, 0) \cdot \exp(i\beta\, kz)\,. \tag{2.41}$$

The Parseval identity holds, too:

$$\int_0^\infty r \cdot \int_0^{2\pi} |u(r, \varphi, z)|^2\, d\varphi\, dr = 2 \sum_{m \in \mathbf{Z}} \int_{-\infty}^{\infty} |G_m(\tau, z)|^2\, d\chi_m(\tau)\,. \tag{2.42}$$

■

PROOF:

Eq. (2.37) and the standard Parseval identity for Fourier series imply that $\sqrt{r} \cdot u_m(r, z) \in L^2(0, \infty)$ with $u_m(r,z)$ defined in Eq. (2.38). Thus, $u_m(r,z)$ matches the assumptions of both Theorem 2.2 and Theorem 2.3. According to Theorem 2.2, the integral Eq. (2.40) defining $G_m(\tau, z)$ converges. Eq. (2.32) and the inverse Fourier transform imply Eq. (2.39). Eq. (2.41) holds due to Eq. (2.12). The Parseval identity Eq. (2.42) holds due to Eq. (2.33) and the standard Parseval identity for Fourier series. ■

2.1.3.2 Illumination, modal fields and fibre output

For fibre lighting purposes in the experimental part of this work a red laser (Part 5.2) illuminating the whole fibre input face was used. Using the approach from [1], we will assume the following simplifications:

- The fibre input face is uniformly illuminated. This assumption is justified, as the beam diameter (half width of a Gaussian energy distribution) of the laser used for measurements is 3 mm to 4 mm, while the fibre diameter is 1 mm only.
- Fields at the input face are approximately those at the boundary between two semi-infinite media of refractive indices 1 (air) and n_0 (core).
- Weak guidance assumption, i.e. $\Delta n \approx 0$.
- Modal fields in considered case of a semi-infinite waveguide are the same as in the case of an infinite waveguide.

Those simplifications will allow finding relatively simple formulae for angle-dependent mode excitation.

Let the input face of the fibre be lighted by a plane wave with the direction of propagation contained in the x-z surface, uniformly polarized in y-axis direction and with incident angle α with the fibre axis (*Fig. 2.3*).

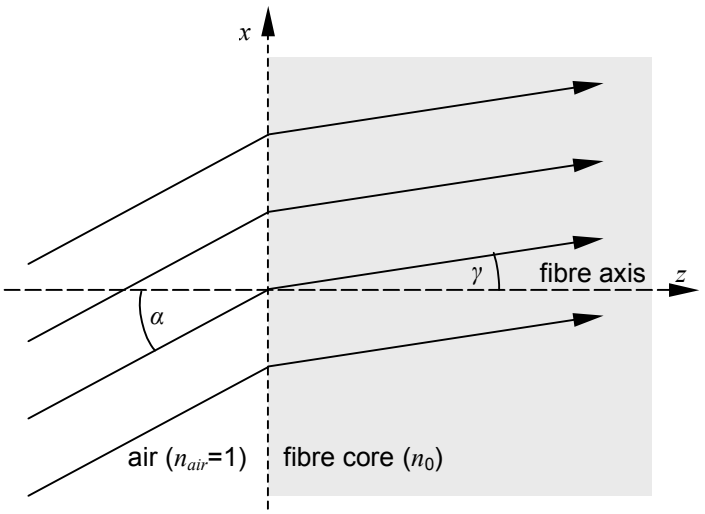

Fig. 2.3 *Refraction of a beam at the input face of a weakly guiding fibre.*

According to the second assumption, the field u at the input face can be computed from standard formulae for plane-wave refraction at a dielectric interface [4]. Normalising, to keep the total power illuminating the waveguide core constant, and using the Snell's law Eq. (2.79), we get the following expression for the field u at the input face $z = 0$ inside the fibre:

$$u(r,\varphi,0) = \sqrt{p(\alpha)} \cdot \mathbf{1}_{core}\left[\exp(ikn_0 x \sin\gamma)\right] = \\ = \sqrt{p(\alpha)} \cdot \mathbf{1}_{core}\left[\exp(ikx\sin\alpha)\right] = \sqrt{p(\alpha)} \cdot \mathbf{1}_{r\in[0,R)}\left[\exp(ikr\cos\varphi \cdot \sin\alpha)\right], \tag{2.43}$$

where $p(\alpha)$ is the Fresnel transmission coefficient Eq. (2.96). Now, using the series expansion Eq. (A1.3) and Eq. (A1.4) we obtain:

$$u(r,\varphi,0) = \mathbf{1}_{r\in[0,R)}\left[\sqrt{p(\alpha)} \cdot \sum_{m\in Z} i^m J_m(kr\sin\alpha)\cdot\exp(im\varphi)\right]. \tag{2.44}$$

According to Eq. (2.38):

$$u_m(r,0) = \sqrt{p(\alpha)} \cdot i^m \cdot \mathbf{1}_{r\in[0,R)}\left[J_m(kr\sin\alpha)\right] \tag{2.45}$$

Use the formula Eq. (A1.5) and Eq. (2.21), Eq. (2.25), Eq. (2.27) to compute the definite integral Eq. (2.40) and obtain:

$$(G_0)_m(\alpha;\tau,0) = i^m\sqrt{p(\alpha)}\cdot\int_0^R r\cdot J_m(w_0 r)\cdot J_m(kr\sin\alpha)\,dr = \\ = \frac{i^m R\sqrt{p(\alpha)}}{w_0^2 - k^2\sin^2\alpha}\left[k\sin\alpha\cdot J_m(w_0R)\cdot J_{m-1}(kR\sin\alpha) - w_0 J_m(kR\sin\alpha)\cdot J_{m-1}(w_0R)\right]\cdot \tag{2.46}$$

The Parseval identity Eq. (2.42) allows to write the following formula for the power contained in a guided mode:

$$p_m^{(0)}\left(\alpha;\tau_k^m\right) := 2r_k^m \left|\left(G_0\right)_m\left(\alpha;\tau_k^m,0\right)\right|^2 , \tag{2.47}$$

where r_k^m is defined in Eq. (2.35), Eq. (2.23) and Eq. (2.26). The total power in radiating modes is given by:

$$p_r^{(0)}(\alpha) := k^2\pi \sum_{m\in\mathbf{Z}} \int_{-\infty}^{n_1^2} \frac{\left|\left(G_0\right)_m(\alpha;\tau,0)\right|^2}{a_m^2(\tau)+b_m^2(\tau)}\, d\tau , \tag{2.48}$$

where $a_m(\tau)$ and $b_m(\tau)$ are defined in Eq. (2.28). The total incident power equals:

$$p_{inc} := \pi R^2 . \tag{2.49}$$

Sample computations and graphs for angle-dependent mode excitations of two waveguides with parameter $V = 8$ and $V = 20$ can be found in Appendix A2. In Part A2.2 we define, basing on the simulations results, the optimal illumination angle for a guided mode, i.e. the illumination angle maximising the power Eq. (2.47) entering the mode, and call it further the *external propagating angle* of the mode (as relative to the outside environment, so α and not γ on *Fig. 2.3*).

Using Eq. (2.46) and the assumptions stated at the beginning of this part, modal fields dependent on the illumination angle can be accurately found (as on *Fig. A2.8*). The opposite construction, i.e. the precise build-up of fibre angular output characteristics from its modal fields is not possible within the scalar wave equation approach as the scalar wave equation does not retain the vector properties of propagating fields. However for investigations of scattering and mode mixing the angular representation of modal fields is necessary. Thus, we will adopt a simplified procedure and assume that each mode at the fibre end produces the angular power output per solid radian (FFP, i.e. far-field profile, see Part 2.3.1) of the same shape as its normalised excitation characteristics Eq. (2.47):

$$output\left(\alpha_{out};m,\tau_k^m\right) := \frac{p_m^{(0)}\left(\alpha_{out};\tau_k^m\right)}{2\pi \int_0^{0.5\pi} p_m^{(0)}\left(\alpha;\tau_k^m\right)\sin\alpha\, d\alpha} . \tag{2.50}$$

Therefore, if $p_m\left(\tau_k^m\right)$ equals the power contained in LP_{mk} mode at the fibre's end, then fibre output is assumed to be the $\{p_m\left(\tau_k^m\right)\}$-weighted superposition of curves Eq. (2.50), i.e. the angular density of output energy per unit time is assumed to equal:

$$output(\alpha_{out}) := \sum_{m\in Z}\sum_{k=0}^{P_m} p_m\left(\tau_k^m\right) output\left(\alpha_{out};m,\tau_k^m\right), \tag{2.51}$$

where only guided modes were taken into account, as they carry most of the propagating power, an assumption that will be justified on examples in Appendix A2.2 and henceforth used. Note that Eq. (2.51) can be easily put down in vector notation as

$$output(\alpha_{out}) = \left[p_m\left(\tau_k^m\right)\right]^{\mathrm{T}} \cdot \left[output\left(\alpha_{out}; m, \tau_k^m\right)\right], \tag{2.52}$$

where both vectors contain respective values computed for all modes in the same order.

2.1.4 Scattering and mode mixing

Even if the illuminating beam has a very small divergence (as it is the case with a laser beam) and the angular input characteristic of the waveguide contains only one narrow peak around the beam inclination angle, the angular characteristic of the output usually is much more diffused. This process is referred to as scattering, mode mixing or mode coupling; its most important reason are minute perturbations of the waveguide's refractive index, which are inevitable in a real waveguide and give rise to the continuous power flow between propagating modes (Part 2.1.4.2). Another, often neglected reason, are the field transitions: illuminating to modal and modal to output (Part 2.1.4.1). According to Eq. (2.46) even the most parallel beam excites several guided modes, whose diffuse input/output characteristics superposed in Eq. (2.52) build-up a diffuse output.

2.1.4.1 Scattering on input and end faces

Under the assumption of no power transfer between modes, due to Eq. (2.46) and Eq. (2.52), the angular output power distribution can be expressed as:

$$output(\alpha_{out}, \alpha) := \left[p_m^{(0)}\left(\alpha; \tau_k^m\right)\right]^{T} \cdot \left[output\left(\alpha_{out}; m, \tau_k^m\right)\right], \tag{2.53}$$

where α and α_{out} are the input and output angles[1], respectively. *Fig. A2.14* in Appendix A2 shows sample angular output distributions for few inclinations of the input beam and for two sample waveguides. Numerical analysis described there showed that this kind of scattering (in investigated waveguides) practically does not depend on the illumination angle (see *Fig. A2.15*).

2.1.4.2 Refractive index perturbations

In an ideal non-absorbing waveguide the refractive index profile as well as the power distribution between modes are steady along the waveguide's length. Slight refractive index perturbations, inevitable in a real waveguide, give rise to the continuous power flow between modes, usually referred to as the mode mixing or coupling. We will follow the analysis of scattering of Magnanini and Santosa [8] and expand it to the three-dimensional case of an optical fibre using the approach of Alexandrov and Ciraolo [2].

The refractive index n in Eq. (2.10) of an ideal waveguide depends only on the radius r. The perturbed waveguide in our analysis will have a refractive index $n_p(r,\varphi,z)$, defined by the perturbation function $d(r,\varphi,z)$:

$$\begin{aligned} n_p^2(r,\varphi,z) &= n^2(r) + d(r,\varphi,z) \\ \operatorname{supp} d(r,\varphi,z) &= \Omega = [0,R_0]\times[0,2\pi)\times[0,z_0] \end{aligned}, \tag{2.54}$$

[1] The angles between the waveguide's axis and the direction of propagation.

for some finite R_0 and z_0. Substituting Eq. (2.54) into Eq. (2.10) gives the Helmholtz equation, discussed in the case of a 3-D waveguide in [2]:

$$\Delta u + n^2(r)k^2 u = -k^2 d(r,\varphi,z)u \,; \tag{2.55}$$

the total field u can be decomposed to the sum of the incident and scattered fields:

$$u(r,\varphi,z) = u_{inc}(r,\varphi,z) + u_{scat}(r,\varphi,z) \,. \tag{2.56}$$

Substituting Eq. (2.56) into Eq. (2.55) and using the homogenous scalar wave equation Eq. (2.10) satisfied by u_{inc} we obtain a variant of the Helmholtz equation:

$$\Delta u_{scat} + n^2(r)k^2 u_{scat} = -k^2 d(r,\varphi,z)u \,, \tag{2.57}$$

where the scattered field must obey some form of radiation conditions guaranteeing its uniqueness. As the exact form of those conditions is not known, we will state as a hypothesis the radiation conditions used by Alexandrov, Ciraolo [2] in solving a version of Eq. (2.57), adapted from the open-space scattering problem [9, 25], modified to reflect the waveguide geometry:

HYPOTHESIS 1 [2] If the following conditions are satisfied for all $m \in \mathbf{Z}$

$$\begin{aligned}
&u_{scat} \in C^1(\mathbf{R}^3), \\
&d(r,\varphi,z) \text{ is continuous and with compact support,} \\
&\lim_{r\to\infty}\left[\sqrt{r}\,j_m(r,\tau)\frac{\partial}{\partial r}\left[\sqrt{r}(u_{scat})_m(r,z)\right] - \sqrt{r}(u_{scat})_m(r,z)\frac{\partial}{\partial r}\left[\sqrt{r}\,j_m(r,\tau)\right]\right] = 0 \text{, for } d\chi_m(\tau) \neq 0 \\
&\lim_{|z|\to\infty}\left[\frac{\partial}{\partial|z|}(G_{scat})_m(z,\tau) - ik\beta\cdot(G_{scat})_m(z,\tau)\right] = 0 \text{, for } \tau = \beta^2 \geq 0 \text{ with } d\chi_m(\tau) \neq 0 \\
&\lim_{|z|\to\infty}(G_{scat})_m(z,\tau) = 0 \text{, for } \tau = \beta^2 < 0 \,,
\end{aligned} \tag{2.58}$$

where $(u_{scat})_m$ is defined analogously to u_m (Eq. (2.38)):

$$(u_{scat})_m(r,z) = \frac{1}{2\pi}\int_0^{2\pi} e^{-im\varphi}\cdot u_{scat}(r,\varphi,z)\,d\varphi \,, \tag{2.59}$$

and $(G_{scat})_m$ analogously to G_m (Eq. (2.40)):

$$(G_{scat})_m(\tau,z) = \int_0^{\infty} r\cdot j_m(r,\tau)\cdot(u_{scat})_m(r,z)\,dr \,, \tag{2.60}$$

and u_{inc}, d, j_m, $d\chi_m$ are defined in Eq. (2.56), Eq. (2.54), Eq. (2.21), Eq. (2.25), Eq. (2.27) and Eq. (2.34) then there exists at most one complex function u_{scat} on $\mathbf{R}^3$ satisfying the equation Eq. (2.57). ■

The meaning of the first two conditions of Eq. (2.58) is obvious; the third signifies a fast decay of the field as radius $r \to \infty$, the last two mean that the energy going to $|z| = \infty$ may be divided into two parts: one oscillatory and one decaying.

The (assumed to be unique under Hypothesis 1) solution to Eq. (2.57) can be written as:

$$u_{scat}(r,\varphi,z) = -k^2 \int_\Omega d(\rho,\eta,\xi) u(\rho,\eta,\xi) g(r,\varphi,z;\rho,\eta,\xi) dV \tag{2.61}$$

and rewritten in the form of an integral equation:

$$u(r,\varphi,z) = u_{inc}(r,\varphi,z) - k^2 \int_\Omega d(\rho,\eta,\xi) u(\rho,\eta,\xi) g(r,\varphi,z;\rho,\eta,\xi) dV\ , \tag{2.62}$$

where $g(r,\varphi,z;\rho,\eta,\xi)$ is the Green's function of a homogenous waveguide, found in [2] (with the assumption that the conditions Eq. (2.58) hold) to be equal to:

$$g(r,\varphi,z;\rho,\eta,\xi) = -\frac{i}{4\pi^2 k} \sum_{m\in\mathbf{Z}} e^{im(\varphi-\eta)} \int_{-\infty}^{\infty} \frac{1}{\beta} e^{i|z-\xi|k\beta} \cdot j_m(r,\tau) \cdot j_m(\rho,\tau)\, d\chi_m(\tau) \tag{2.63}$$

Equation Eq. (2.62) is satisfied by the von Neumann series [13]:

$$u(r,\varphi,z) = \sum_{l=0}^{\infty} u_l(r,\varphi,z)\ , \tag{2.64}$$

where

$$\begin{aligned} u_0(r,\varphi,z) &= u_{inc}(r,\varphi,z) \\ u_{l+1}(r,\varphi,z) &= T u_l(r,\varphi,z) \end{aligned}\ , \tag{2.65}$$

and the operator T is defined as:

$$Tu(r,\varphi,z) = -k^2 \int_\Omega d(\rho,\eta,\xi) u(\rho,\eta,\xi) g(r,\varphi,z;\rho,\eta,\xi) dV\ . \tag{2.66}$$

The scattered field can be finally computed as:

$$u_{scat}(r,\varphi,z) = \sum_{l=1}^{\infty} u_l(r,\varphi,z)\ . \tag{2.67}$$

Appendix A4 contains considerations concerning a possible proof of the convergence of the series Eq. (2.67) in the supremum norm. If brought to the end, they would prove the existence and continuity of Eq. (2.67) and hence confirm that found u_{scat} is (under Hypothesis 1) the solution of Eq. (2.57) in the distribution space. Here the convergence will be formulated as a hypothesis only:

HYPOTHESIS 2 The series Eq. (2.64) converges in the supremum norm. ■

As Magnanini and Santosa did in [8], we will use in further computations the Born approximation, i.e. we will use only the first term of the von Neumann series Eq. (2.64) in the right hand side of Eq. (2.62) to get:

$$u_{scat}(r,\varphi,z) \approx -k^2 \int_{\Omega} d(\rho,\eta,\xi)\cdot u_{inc}(\rho,\eta,\xi)\cdot g(r,\varphi,z;\rho,\eta,\xi)\,dV\,. \tag{2.68}$$

Next, to investigate the waveguide's mode mixing properties, we will use Eq. (2.39), Eq. (2.40), Theorem 2.3, Eq. (2.30) and the orthogonality of $\{\exp(im\varphi)|m\in\mathbf{Z}\}$ to obtain the scattered field and excitations of guided modes *after* the perturbation, i.e. for $z \ge z_0$:

$$\begin{aligned}&(G_{scat})_m(z,\tau) = \\ &= \frac{ik}{4\pi\beta}\exp(i\beta kz)\cdot\int_{\Omega} d(\rho,\eta,\xi)\cdot u_{inc}(\rho,\eta,\xi)\exp(-im\eta)\exp(-i\beta k\xi)\cdot j_m(\rho,\tau)dV\end{aligned} \tag{2.69}$$

If assumed that the incident field consists of exactly one guided mode, i.e. that

$$u_{inc}(r,\varphi,z) = \exp(i\beta_0 kz)\exp(im_0\varphi)\cdot j_m(r,\tau_0)\,, \tag{2.70}$$

where $\tau_0 = \beta_0^2$, then Eq. (2.69) can be rewritten for $z \ge z_0$ in the following form:

$$\begin{aligned}&(G_{scat})_m(z,\tau) = \\ &= \frac{ik}{4\pi\beta}\exp(i\beta kz)\cdot\int_{\Omega} d(\rho,\eta,\xi)\cdot e^{i(m_0-m)\eta}e^{i(\beta_0-\beta)k\xi}\cdot j_{m_0}(\rho,\tau_0)\cdot j_m(\rho,\tau)dV = \\ &= e^{i\beta k(z-z_0)}\cdot(G_{scat})_m(z_0,\tau)\,.\end{aligned} \tag{2.71}$$

This form, given the form of refractive index perturbations $d(r,\varphi,z)$, together with the Parseval identity Eq. (2.33) and under the Born approximation may be used to compute the power transfer coefficients between modes caused by the refractive index perturbations. If Eq. (2.70) is the incident field, then the *r*elative *s*cattered *p*ower in LP_{mk} mode equals:

$$rsp(m_0,k_0;m,k) := \frac{r_k^m r_{k_0}^{m_0}}{\pi^2}\left|(G_{scat})_m(z_0,\tau_k^m)\right|^2\,. \tag{2.72}$$

Eq. (2.53) describes the angular output power distribution of an ideal waveguide, depending on the illumination angle. In a similar way we can write down the formula in the case of a waveguide containing a perturbed fragment of length z_0:

$$outputMix(\alpha_{out},\alpha) := \left[p_m^{(0)}(\alpha;\tau_k^m)\right]^T\cdot\left[rsp(m_0,k_0;m,k)\right]\cdot\left[output(\alpha_{out};m,\tau_k^m)\right], \tag{2.73}$$

where the middle term denotes the power coupling matrix obtained from Eq. (2.72), whose rows represents ordered all incidence modes (indices m_0, k_0 of Eq. (2.72)) and columns all ordered output modes (indices m, k). The mode order should be the same as in the cases of both vectors representing mode excitations by the illuminating beam and the superposed mode output characteristics.

Results of numerical computations for two waveguides and random perturbations of the refractive index are presented in Appendix A2.3. Apparent relation between the scattered field and the illuminating angle found there will be assumed to hold for all waveguides and used in the raytracing model and the modelling software.

2.1.5 POF and transition to modal continuum

A huge number of guided modes (more than 10^6 for a standard 1 mm POF), increasingly unique guided mode – propagation angle correspondence (Appendix A2.2) and the smooth scattering characteristics of Appendix A2.3 suggest the transition to modal continuum and to geometric optics, which is the topic of the following Part 2.2. Within this approach a propagating mode is represented by a bunch of rays (i.e. local plane waves), see [1, Chapter 36] for a discussion of local mode – ray correspondence.

2.2 Raytracing model

The raytracing model is based on geometric optics, and considered valid in the limiting case of the wave optics, i.e. for $\lambda \to 0$ compared to system dimensions (in typical POF applications $\lambda \approx 653$ nm, fibre diameter is 1 mm). It makes use of the concept of a ray, refraction and total internal reflection [10]. The general ideas behind modelling and raytracing through an ideal step-index fibre within the framework of geometric optics are as follow:

- The fibre is considered to consist of a core and an infinite clad with the refractive index $n(r)$ defined by Eq. (2.16) or of a core and a finite clad immersed in air with the refractive index of

(2.74)
$$n(r) = \begin{cases} n_0 & , r \in [0, R_1] \quad \text{(core)}, \\ n_1 < n_0 & , r \in (R_1, R_2] \quad \text{(clad)}, \\ 1 < n_1 & , r \in (R_2, \infty) \quad \text{(air)}. \end{cases}$$

- The angular power distribution of the light source is used as a probability distribution to generate rays incident on the fibre input face.
- Each generated incident ray is traced (*Fig. 2.4*) through the fibre according to the Snell's law via successive total internal reflections on the core-clad and/or clad-air (jacket) interface until it leaves the fibre end or is transmitted through the interfaces and lost outside the fibre. According to the Fresnel law, each transmission of a ray through an interface is accompanied by its non-total reflection, which is usually neglected in the basic raytracing model (see Part 2.2.3).
- After a sufficient number of rays is traced, required average characteristics (such as attenuation or near- and far-field profiles, see Part 2.3) are computed at the fibre endface.

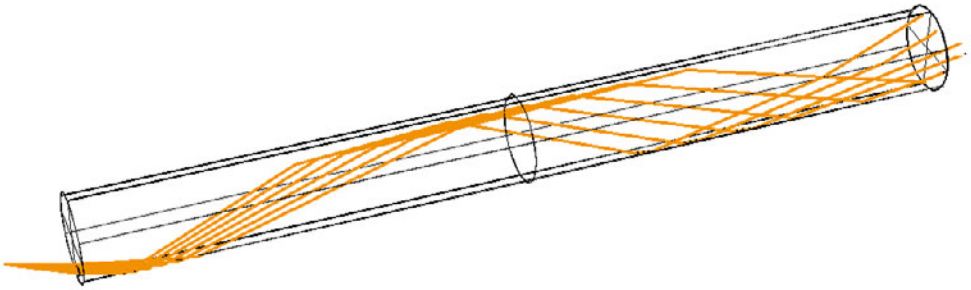

Fig. 2.4 *An example of raytracing of six rays through a fragment of an ideal step-index fibre.*

The Snell's law, refraction and total internal reflection are illustrated on *Fig. 2.5*.

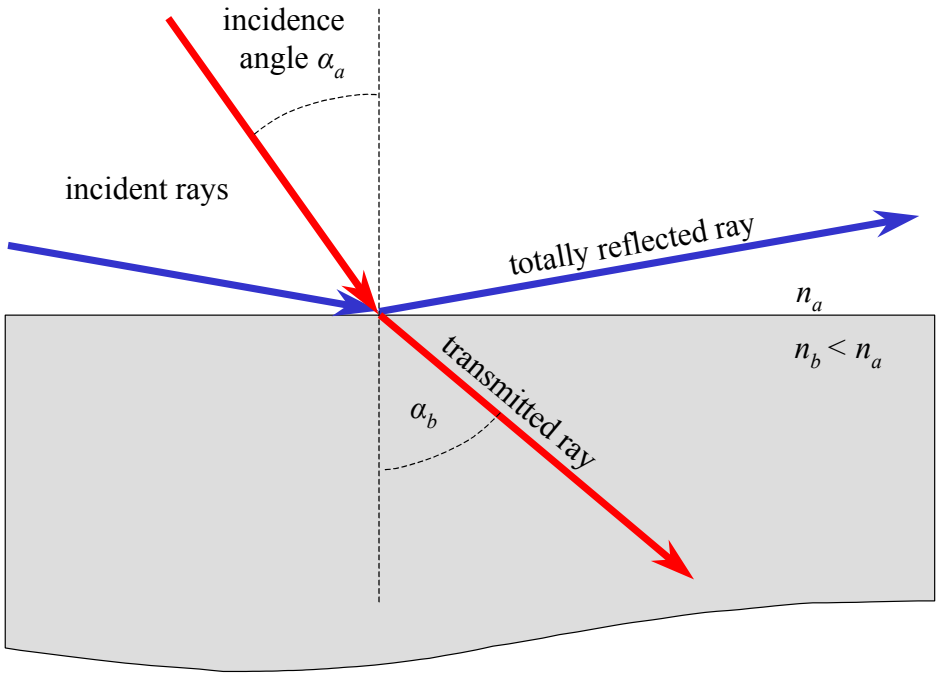

Fig. 2.5 *Snell's law: ray transmission and total internal reflection on the interface between two media of different refractive indices.*

According to the Snell's law (neglecting absorption and partial reflection), the ray incident on a flat interface between two media of different refractive indices is either totally transmitted or totally reflected, depending on the values of the refractive indices of both media and the incidence angle of the ray. The incidence and transmission angles of the transmitted ray are governed by the following identity:

(2.75) $$n_a \sin\alpha_a = n_b \sin\alpha_b \,.$$

Dividing both sides by n_a we get the condition for the angle α_a of the incident ray:

(2.76) $$\sin\alpha_a = \frac{n_b}{n_a}\sin\alpha_b .$$

And as $\sin\alpha_b \le 1$ we get the following relation

(2.77) $$\sin\alpha_a \le \frac{n_b}{n_a} .$$

From Eq. (2.77) follows that for $n_a > n_b$, so when the ray comes from the media with a higher refractive index (like in the case of a ray incident from within the fibre core), not all incident rays can be transmitted into the second medium. Thus, according to the Snell's law, an incident ray is transmitted through the interface if and only if

(2.78) $$\alpha_a \in [0,\alpha_T), \text{ where } \alpha_T = \arcsin\left(\min(1,\frac{n_b}{n_a})\right) \le \frac{\pi}{2} .$$

If the incidence angle α_a exceeds α_T, the total internal reflection occurs and the ray is reflected back into the media it originates from. This simple, binary approach (ray is either transmitted or reflected back) forms the basis for the simple raytracing model. In such a model the fibre accepts incident *meridional rays* (i.e. the rays crossing its axis) only within its *acceptance angle*.

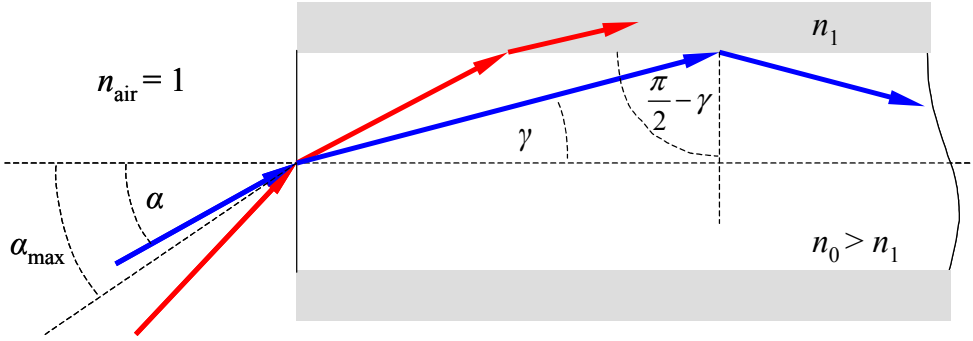

Fig. 2.6 *Light acceptance of a step-index optical fibre.*

Applying the Snell's law to the meridional ray confined to the core (the blue ray on *Fig. 2.6*), inverting the inequality Eq. (2.77) (the ray has to be reflected back into the core) and knowing that $n_1 < n_0$, we can obtain:

$$\sin\alpha = n_0 \sin\gamma ,$$

(2.79) $$\sin\left(\frac{\pi}{2} - \gamma\right) > \frac{n_1}{n_0} .$$

Taking into account

(2.80) $$\cos\gamma = \sin\left(\frac{\pi}{2} - \gamma\right)$$

we finally get the guidance condition for incident meridional rays

(2.81) $$\sin\alpha \le \sin\alpha_{\max} = \sqrt{n_0^2 - n_1^2}\ .$$

The maximum incidence angle α_{max} is called the *acceptance angle* of the fibre, while its sine is called fibre's *numerical aperture* NA:

(2.82) $$NA = \sin\alpha_{\max} = \sqrt{n_0^2 - n_1^2} = n_0\sqrt{\frac{n_0 + n_1}{n_0}\frac{n_0 - n_1}{n_0}} \approx n_0\sqrt{2\Delta}\ ,$$

where Δ is the relative index difference.

Rays traced exactly according to the Snell's law happens only in the ideal fibre case. To enable modelling of fibre aging processes, two important imperfection-related phenomena have to be introduced: *attenuation* and *scattering*. Moreover, as the total internal reflection, according to the Snall's law, ceases to occur above the critical angle, the fibre abruptly looses all of its guidance properties above its acceptance angle Eq. (2.72). But in reality, the limit between total internal reflection and transmission of a ray is not abrupt and incident rays are rather splitted on the core-clad interface than totally transmitted, as the Fresnel law states. Although the simple binary approach is often used, it is only a rough approximation of the reality. Due to the Fresnel reflection approx. 4 % of the power of an incident beam is lost (reflected back) already at the input face of a fibre, while the Snell's law predicts no reflection there. Modelling of attenuation and scattering properties of an optical fibre within the geometric optics approach and modelling the Fresnel reflection are discussed in Part 2.2.1 to Part 2.2.3.

Raytracing model, besides its intuitive interpretation, has three main advantages that make it particularly useful for simulating aging effects on light propagation:

- Aging-related characteristics (attenuation and scattering) are direct model parameters.
- Total fibre attenuation and relatively easy-to-measure far- and near-field profiles can be simply computed.
- Fibre geometry distortions (e.g. imperfections of a core-clad interface) can be easily modelled.

2.2.1 Attenuation

The material causes of attenuation are briefly discussed in Part 4.1, devoted to fibre aging processes. Here it will be considered only within the framework of fibre modelling and the raytracing approach.

In an ideal raytracing system each ray carries a unit power and is not attenuated along its way through fibre. But light transmitted in a real fibre is attenuated, i.e. the rays lose their

power along the way. Within the raytracing approach this process can be modelled by decreasing the power of each ray due to the fibre bulk material absorption (according to the path length) or after each ray reflection/transmission on the core-clad or clad-air interface. A ray is traced until it leaves the fibre or its power falls below a given cut-off level.

Table 2.2 *Attenuation parameters.*

bulk attenuation	interface attenuation coefficients
core attenuation	*core-clad reflection*
clad attenuation	*core-clad transmission*
	clad-air reflection
	clad-air transmission

Therefore, two obvious groups of attenuation parameters will be used, as listed in *Table 2.2*: the *bulk attenuation* of fibre core and clad and the *interface attenuation coefficients* related to ray reflection and transmission on the interface:

- *Bulk core attenuation* parameter a_{b0} and *bulk clad attenuation* a_{b1}. Power P of each ray is decreased due to the bulk material absorption and depends on the ray path lengths l_0 and l_1 covered respectively within the fibre core and clad:

(2.83) $$P = P_0 \exp\left(-a_{b0} l_0 - a_{b1} l_1\right),$$

  where P_0 is the initial power of the ray.

- *Interface attenuation* parameters model ray attenuation on the core-clad and clad-air interface (inter alia the Goos-Hänchen shift, i.e. the penetration of the reflecting ray into the other medium, see [2]). After each ray reflection or transmission on one of those interfaces the power of the ray is decreased:

(2.84) $$P_{after\ reflection\ or\ transmission} = \alpha_i \cdot P_{before\ reflection\ or\ transmission},$$

  where a_i is one of the four interface attenuation coefficients (*Table 2.2*).

In a fibre of length L, without scattering, a ray incident on the input face under the angle α and propagated through fibre with the internal angle γ (Eq. (2.70)) towards the fibre axis covers a path of $L/\cos\gamma$ length and undergoes at least $L \cdot \tan\gamma / 2R$ reflections (in the case of a meridional ray). Both values depend on the incidence angle and thus the total attenuation of a specific ray also depends on its incidence angle. Therefore, it may not be equal to the general 'attenuation' parameter of the fibre, which is given in fibre's technical data and which characterises only fibre's average attenuating properties. The real measured attenuation, especially of a short fibre, often depends very much on the illumination conditions (see *Fig. 6.5*).

2.2.2 Scattering

The material causes of scattering are briefly discussed in Part 4.1, devoted to fibre aging processes. Here it will be considered only within the framework of fibre modelling and the raytracing approach. The wave optics approach to scattering was discussed in Part 2.1.4,

here we will use only the results of the numerical experiments concerning the angle dependence of the scattering intensity from Appendix A2.3.

In an ideal step-index fibre ray path between successive reflections is straight, Snell's (or Fresnel, see Part 2.2.3) law and total reflection exactly governs ray reflections and define its path. However, in a real fibre, there are several scattering effects distorting the ray path. As showed in *Table 2.3*, all scattering parameters in principle may be categorised into three groups: *interface*, *bulk* and *endface scattering*.

Table 2.3 *Scattering parameters*[2].

bulk scattering	interface scattering	endface scattering
core bulk scattering scale	*core-clad interface axial scattering*	*endface scattering*
core bulk scattering slope	*core-clad interface azimuthal scattering*	
core bulk scattering slope location	*clad-air interface axial scattering*	
core bulk scattering axial dispersion	*core-air interface azimuthal scattering*	
core bulk scattering azimuthal dispersion		
clad bulk scattering scale		
clad bulk scattering slope		
clad bulk scattering slope location		
clad bulk scattering axial dispersion		
clad bulk scattering azimuthal dispersion		

Endface scattering models imperfections of the fibre endfaces and the scattering effects of the conversion between illuminating/output fields and the modal fields discussed in Part A2.1 and Appendix A2.3.1. The examples investigated there suggest a constant *endface scattering* coefficient, not dependent on the illumination angle. Thus a ray, when transmitted through fibre input or endface, is randomly redirected and the redirection angle is drawn each time from the centred Gaussian distribution with standard deviation equal to the *endface scattering* coefficient.

Interface scattering models imperfections of the core-clad and clad-air interfaces. Their axial and azimuthal imperfections are modelled as minute deformations of the ideal cylindrical shape in both directions, along and across the fibre. The tilt of the tangent plane

[2] The term dispersion in *Table 2.3* and henceforth refers to the angular broadening of peaks in the far-field profile and not to the time-related pulse broadening affecting the bandwidth of a fibre.

in the point where a ray hits the interface is described by two parameters: the standard deviations of axial and azimuthal tilt angles. The actual tilt at each reflection/transmission point is found by drawing two random numbers from the corresponding normal distributions. The mean number of undergone reflections is proportional to the tangent of the propagation angle γ and thus the total interface scattering increases with the incidence angle α and the propagation angle γ of a ray.

Bulk scattering models two main different scattering processes: one due to minute intrinsic nonuniformities of the fibre refractive index[3] and the second caused by extrinsic impurities and defects of the core and clad bulk material. The interface scattering occurs only on interfaces encountered by the ray on its way, while the bulk scattering distorts the direction of a ray in discrete points along its way *in* the bulk fibre material itself, due to abstract scattering obstacles representing impurities, defects or local irregularities of the refractive index. Two groups of parameters are required: one to decide *when* and the second to decide *how* a ray should be scattered:

- *Mean free path* (*fmp*) length. Similarly to Arrue et al. [11], we will use the concept of a *mean free path* length: each ray travels free within the fibre core or clad between successive scattering points; the distance of its free path is determined using the free mean path parameter. Arrue et al. [11] propose the deterministic model where the free path of a ray is always of the same length (1 mm, i.e. the diameter of a typical POF), not depending on the ray propagation angle. We will expand this model in two important aspects:

    I. We will use a probabilistic model; the free mean path will be the *mean* of each time randomly drawn free path distance. As the probability of encountering a scattering obstacle by a ray is assumed to be constant per unit length of ray path, the actual distance is modelled by the exponential random distribution. Besides this simple rationale, the choice of the exponential distribution has two other important advantages:

        - The exponential distribution is the only continuous random distribution that *does not have memory*, i.e. for an exponential random variable X

(2.85)
$$P[X > z] = P[X > x + z | X > x] .$$

          This feature makes the bulk scattering process not dependent on ray reflections/transmissions on the core-clad and clad-air interfaces, so that they can occur in-between successive ray bulk scatterings, without disturbing the exponential bulk scattering process itself.

        - Ray path lengths between successive redirection points form a stochastic Poisson process with intensity being the reciprocal of the mean free path. The overlay of a finite number of Poisson

[3] Often referred to as Rayleigh or Mie scattering, which are not quite precise descriptions here, because the terms originally describe the scattering of a plane wave and not of modal waves.

processes is also a Poisson process, so should it in future be necessary to differentiate between diverse causes of bulk scattering, the *joint* scattering process due to *all* of the causes will be also governed by the exponential random distribution with the intensity being the sum of the intensities of all component processes. This way the model stays open and easily expendable: several additional defect-related scattering processes may be separately added, removed and modelled, while the exponential (Poisson) characteristic of the *joint* bulk scattering process remains the same.

II. In Appendix A2.3.2 the total scattered power Eq. (A2.12) is on numerical examples found to be decreasing with the illumination angle α (see *Fig. A2.17*), and so also with the propagating angle γ of the ray. Thus, to include this scattering property in the raytracing model, the *free mean path* has to be made angle-dependent, so that the average number of ray redirections *per fibre unit length* has a similar shape to the curves from *Fig. A2.17*. They have been fitted with the following formula

(2.86) $$\exp\left[-\left(\frac{\sin\alpha}{\sin\theta}\right)^{\kappa}\right],$$

where the meaning of the parameters κ and θ could be intuitively explained as follows: the *slope* of the curve depends on κ, while θ defines the *slope's location*. Formula Eq. (2.86) expresses scattering properties of a fibre in terms of the angle-dependent scattered power *per fibre unit length*, as it is the case with Eq. (A2.12) and *Fig. A2.17*. However, the average number of undergone scatterings depends on the total path length of a ray, so not only on the fibre length but also on the internal propagation angle γ of a ray. Thus, the formula Eq. (2.86) before implementing it in software as the normalised average number of ray redirections *per ray path unit length* has to be multplied by

(2.87) $$\cos\gamma = n_0^{-1}\sqrt{n_0^2 - \sin^2\alpha}$$

and additionally divided by $2\pi\sin\gamma$ to account for the spherical geometry of the system. Finally the following formula is obtained for its reciprocal, i.e. the angle-dependent free mean path of a ray:

(2.88) $$fmp(\alpha) := \frac{2\pi A\sin\alpha}{\sqrt{n_0^2 - \sin^2\alpha}}\exp\left[\left(\frac{\sin\alpha}{\sin\theta}\right)^{\kappa}\right],$$

where A (*bulk scattering scale* parameter of *Table 2.3*) had to be added because Eq. (2.86) describes only normalised total scattered power (as on *Fig. A2.17*). *Fig. 2.7* shows graphs from *Fig. A2.17* (the blue dashed lines) and curves of Eq. (2.86) for few values of the fitting parameters.

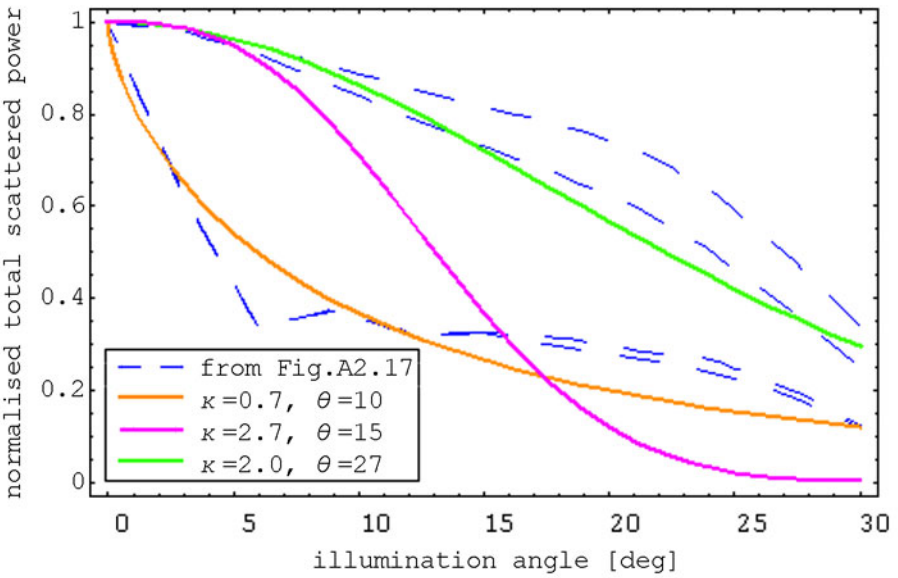

Fig. 2.7 *Total scattered power (or normalised number of ray redirections per fibre unit length) in dependence on the illumination angle. Four curves numerically computed in Appendix A2.3 (Fig. A2.17) and few sample fitting curves of Eq. (2.86).*

- At each scattering point the ray has to be redirected according to four bulk scattering *dispersion* parameters (axial and azimuthal, for core and clad). On the analogy to the interface scattering, the ray is redirected by changing its axial and azimuthal direction angle. The actual redirection angle each time is drawn from the normal distributions with the mean zero and the standard deviation being the respective *scattering dispersion* parameter of the model.

2.2.3 Fresnel reflection

According strictly to the Snell's law, the meridional ray from *Fig. 2.6* will be guided if and only if it is incident within the cone defined by Eq. (2.81). However, more exact analysis shows that the boundary of the cone is diffused and leads to the Fresnel formulae. Treating rays as local plane waves, and because the fields' components tangential to the interface are continuous across the interface [4], the following two conditions can be written:

$$E_{i\perp} + E_{r\perp} = E_{t\perp}\,, \qquad H_{i\perp} + H_{r\perp} = H_{t\perp}\,, \tag{2.89}$$

where E and H denote respectively the amplitudes of the electric and magnetic fields at the interface, the subscripts i, r and t denote incident, reflected and transmitted fields and $\perp$ denote the field component perpendicular to the plane of incidence, so tangential to the interface. From Eq. (2.1) follows

$$H_\perp = E_\parallel \sqrt{\frac{\varepsilon}{\mu}}\,, \tag{2.90}$$

and, using Eq. (2.3), equations Eq. (2.89) can be rewritten as

$$E_{i\perp} + E_{r\perp} = E_{t\perp}\,,$$

$$E_{i\|} + E_{r\|} = \sqrt{\frac{\varepsilon_b}{\varepsilon_a}} E_{t\|} = \frac{n_b}{n_a} E_{t\|}\,, \tag{2.91}$$

where the subscript $\|$ denotes the field component parallel to the plane of incidence. As the power incident on a unit area of the interface must equal the sum of the transmitted and reflected powers, and using the fact that power is proportional to $\sqrt{\varepsilon}E^2$ (and so to nE^2), one can obtain:

$$\sqrt{\varepsilon_1} E_i^2 \cos\alpha_a = \sqrt{\varepsilon_1} E_r^2 \cos\alpha_a + \sqrt{\varepsilon_2} E_t^2 \cos\alpha_b \tag{2.92}$$

and after simple transformation, using Eq. (2.3)

$$E_i^2 - E_r^2 = E_t^2 \frac{n_b}{n_a} \frac{\cos\alpha_b}{\cos\alpha_a}\,, \tag{2.93}$$

what is valid for both perpendicular ($\perp$) and parallel ($\|$) field components. From Eq. (2.91) and Eq. (2.93) we easily get the following formulae for amplitudes of the transferred and reflected fields:

$$\begin{aligned} E_{r\perp} &= E_{i\perp} \frac{n_a \cos\alpha_a - n_b \cos\alpha_b}{n_a \cos\alpha_a + n_b \cos\alpha_b}\,, & E_{t\perp} &= E_{i\perp} \frac{2n_a \cos\alpha_1}{n_a \cos\alpha_a + n_b \cos\alpha_b}\,, \\ E_{r\|} &= E_{i\|} \frac{n_b \cos\alpha_a - n_a \cos\alpha_b}{n_b \cos\alpha_a + n_a \cos\alpha_b}\,, & E_{t\|} &= E_{i\|} \frac{2n_a \cos\alpha_a}{n_b \cos\alpha_a + n_a \cos\alpha_b}\,, \end{aligned} \tag{2.94}$$

as well as the following coefficients for the transferred power $p_\perp$, $p_\|$ and the reflected power $q_\perp$, $q_\|$ (related to the power incident on a unit area of the interface):

$$\begin{aligned} p_\perp &= \frac{n_b \cos\alpha_b}{n_b \cos\alpha_b} \left(\frac{E_{t\perp}}{E_{i\perp}}\right)^2 = \frac{4d \cos\alpha_a \cos\alpha_b}{(\cos\alpha_a + d\cos\alpha_b)^2}\,, \\ q_\perp &= 1 - p_\perp\,, \\ p_\| &= \frac{n_b \cos\alpha_b}{n_a \cos\alpha_a} \left(\frac{E_{t\|}}{E_{i\|}}\right)^2 = \frac{4d \cos\alpha_a \cos\alpha_b}{(d\cos\alpha_a + \cos\alpha_b)^2}\,. \\ q_\| &= 1 - p_\|\,, \end{aligned} \tag{2.95}$$

where $d = \frac{n_b}{n_a}$.

As geometric optics and the raytracing approach do not take into account light polarisation effects, in the following the average of $p_\perp$ and $p_\parallel$ will be used for the power transfer coefficient p:

(2.96) $$p = \frac{1}{2}\left(p_\perp + p_\parallel\right),. \qquad q = 1 - p$$

Fig. 2.8 shows graphs of the three average Fresnel power transmission coefficients p in dependence on the incidence angle α_a for a ray incident from both sides on the core-clad interface and on the input face of a typical POF fibre (for the values of the refractive indices see Eq. (A2.1)). The red line ('air→core') runs for lower incidence angles below the other two, which illustrates the fact that the first loss occurs already on the input face of the fibre, where approx. 4 % of the incident power is reflected back and does not even enter the fibre. Note that rays incident on the core-clad interface from within the core under the angle greater than the critical angle (approx. 70°) are totally reflected back into the core (the blue line 'core→clad' and the blue ray on *Fig. 2.6*), exactly as it is stated by the Snell's law.

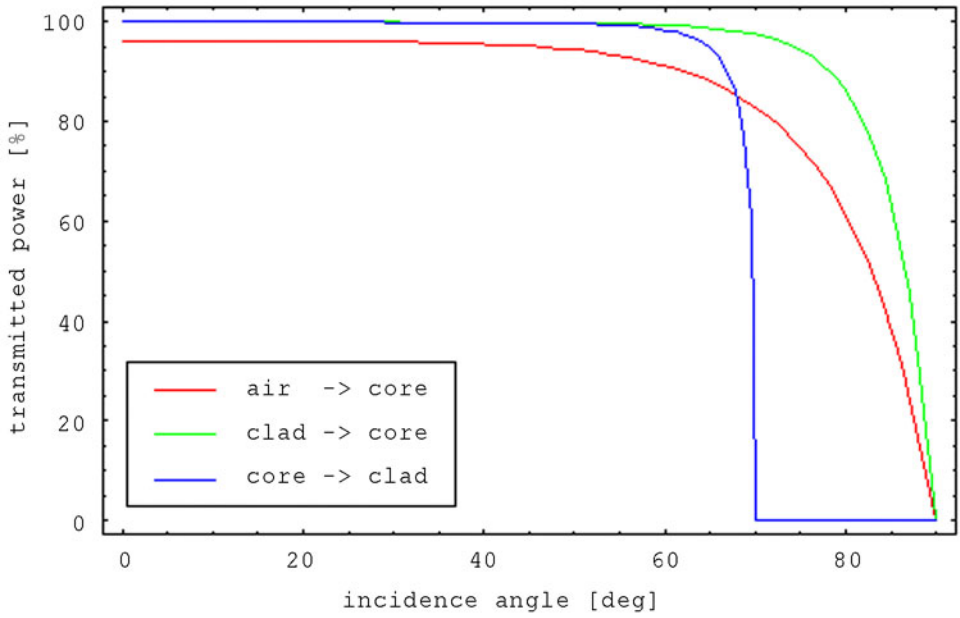

Fig. 2.8 *Average Fresnel power transmission coefficients.*

Raytracing through a fibre within the binary model bases on a simple procedure: a ray incident on the core-clad interface is either transmitted into the fibre clad or reflected back into the core. If the contribution of the partly reflected rays to the optical properties of POF has to be considered, the Fresnel mechanism for ray reflection/transmission must be implemented. Its exact implementation would however require splitting the ray at each interface, unless it was incident under the critical angle or greater. But if rays were actually splitted, the total number of rays to trace would increase exponentially and quickly become computationally unmanageable. To avoid it, each traced ray can be on each encountered interface not splitted but randomly either fully reflected or fully transmitted with probabilities

equal to the relative powers Eq. (2.96) of the respective (reflected and transmitted) rays. For example: let, according to Eq. (2.95) and Eq. (2.96), the reflected ray retain 15 % and the transmitted 85 % of the incident power; such case will be modelled with one ray, either reflected (with 15 % probability) or transmitted (with 85 % probability). Although this solution is intuitively simple and obvious, the proof of its soundness astonishingly turns out not to be as straightforward as it could be expected. Both raytracing processes (i.e. the exact one, with splitting, and the other, modelling probabilistically the splitting) will be redefined as stochastic processes with their values at each step corresponding to the power and configurations (position, direction, etc.) of the traced ray(s) *before* successive Fresnel reflections or at the fibre output. The proof of soundness of the probabilistic raytracing model will be reduced to the proof of *power equivalence* of both stochastic processes, in the meaning defined later.

First we need to define the space of all possible configurations (position, direction, tilt of the splitting interface, arrival time) of the traced ray that are important, i.e. just *before* the Fresnel reflection ($\mathbf{\Theta_0}$ in the definition below) or *leaving* the fibre ($\mathbf{\Theta \backslash \Theta_0}$ below).

DEFINITION 2.5. Let $\mathbf{\Theta_0} \subset \mathbf{\Theta} \subset \mathbf{R}^{11}$, where

$$\begin{aligned}\mathbf{\Theta_0} = \{&(\theta_1,\theta_2,\theta_3,\theta_4,\theta_5,\theta_6,\theta_7,\theta_8,\theta_9,\theta_{10},\theta_{11}) \mid \\ &(\theta_1,\theta_2,\theta_3,\theta_4) \in \Theta_f \times \{0,1\}, \Theta_f \subset \mathbf{R}^3, (\theta_5,\theta_6,\theta_7) \in S^2 \subset \mathbf{R}^3, \\ &(\theta_8,\theta_9,\theta_{10}) \in \Theta_{df} \subset S^2 \subset \mathbf{R}^3, \theta_{10} \in \mathbf{R}\}\end{aligned}$$

and $\mathbf{\Theta \backslash \Theta_0} = \{(\theta_1,\theta_2,\theta_3,\theta_4,\theta_5,\theta_6,\theta_7,\theta'_8,\theta'_9,\theta'_{10},\theta_{11}) \mid$

$$(\theta_1,\theta_2,\theta_3,\theta_4) \in \Theta_f \times \{0,1\}, \Theta_f \subset \mathbf{R}^3, (\theta_5,\theta_6,\theta_7) \in S^2 \subset \mathbf{R}^3, (\theta'_8,\theta'_9,\theta'_{10}) \in S^2 \subset \mathbf{R}^3, \theta_{11} \in \mathbf{R}\},$$

be called the *fibre space* of a given step-index fibre if and only if:

- $\Theta_f \subset \mathbf{R}^3$ is the set of all points of all fibre interfaces (input face, endface, core-clad and clad-air interface) and $\theta_4 \in \{0,1\}$ codes one of the both sides of the interface.
- $\overline{\mathbf{n}} = (\theta_5,\theta_6,\theta_7) \in S^2 \subset \mathbf{R}^3$ is a unit vector normal to the interface at the point $(\theta_1,\theta_2,\theta_3)$ representing its tilt.
- $(\theta_8,\theta_9,\theta_{10}) \in \Theta_{df} \subset S^2 \subset \mathbf{R}^3$ is a unit vector describing the direction of a ray at the point $(\theta_1,\theta_2,\theta_3,\theta_4)$ of the interface with tilt $(\theta_5,\theta_6,\theta_7)$. The set of possible directions Θ_{df} depends on θ_4 and $\overline{\mathbf{n}} = (\theta_5,\theta_6,\theta_7)$, and consists of only such directions, that the Fresnel reflection (and not the total internal reflection) occurs, i.e. that $\sin(\angle(\overline{\mathbf{n}},(\theta_8,\theta_9,\theta_{10}))) \le d_n$, where d_n is the ratio of the refractive index of the target medium to the refractive index of the medium the ray originates from, where the media are differentiated by θ_4.
- $(\theta'_8,\theta'_9,\theta'_{10}) \in \Theta_{do} \subset S^2 \subset \mathbf{R}^3$ is also a unit vector describing the direction of the ray at the point $(\theta_1,\theta_2,\theta_3,\theta_4)$ of the outer fibre interface and pointing *outside* the fibre. The set of possible directions Θ_{do} depends on $(\theta_1,\theta_2,\theta_3,\theta_4)$: is not empty only for $(\theta_1,\theta_2,\theta_3,\theta_4)$ lying on the outside side of the fibre input or end face or clad-air

interface and consists of exactly all such directions that point *outwards* the fibre, i.e. the point $(\theta_1,\theta_2,\theta_3,\theta_4)$ and the direction $(\theta'_8,\theta'_9,\theta'_{10})$ constitute a possible output point and direction for the traced ray.

- $\theta_{11}\in\mathbf{R}$ is the time at which a traced ray reaches the location described by the previous coordinates θ_1 to θ_{10}. ■

The traced ray at each step of the raytracing procedure can be described as a point in the set $\mathbf{\Theta}\times[0,1]$, i.e. by its configuration (position, direction, etc.) and its power.

DEFINITION 2.6. Let $\mathbf{\Theta}$ be the fibre space of a given step-index fibre, defined in Definition 2.5. The set $\mathbf{\Theta}\times[0,1]$, where the interval $[0,1]$ stands for the power of a ray, will be called the *ray space* of the fibre. ■

The successive steps of the raytracing procedure can be described by finite (or one-element, with probabilistic modelling of Fresnel reflections) subsets of $\mathbf{\Theta}\times[0,1]$. Initial illumination of the fibre can be then represented by a subset of $\mathbf{\Theta_0}\times[0,1]$, while the output of the fibre by a subset of $(\mathbf{\Theta}\backslash\mathbf{\Theta_0})\times[0,1]$. Both raytracing processes are schematically depicted on *Fig. 2.9*.

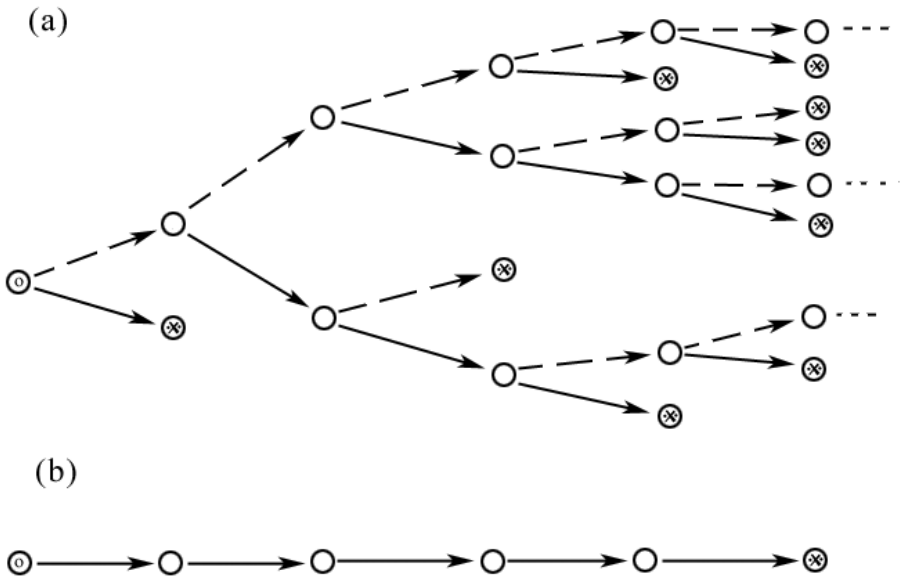

Fig. 2.9 *Few steps of both raytracing procedures. The circles symbolise the points of the ray space. The circles with dot mark the ray input point; the circles with 'x' mark the ray output, i.e. the elements of* $(\mathbf{\Theta}\backslash\mathbf{\Theta_0})\times[0,1]$.

(a) The exact raytracing procedure. At each point of Fresnel reflection the power of the incident ray is splitted into the reflected (solid line) and the transmitted (dashed line) part. The input ray falls on the fibre input face, so the first reflected ray goes back into free space and is marked with 'x'.

(b) The probabilistic modelling of Fresnel reflections. Instead of tracing both reflected and transmitted rays, only one of them is randomly chosen (with the probability proportional to the power split coefficients in the process (a)) and further traced with full power of the incident ray.

Before the processes can be formally defined, few auxiliary definitions and symbols should be introduced:

DEFINITION 2.7. Let $\boldsymbol{\Theta}$ be the fibre space and $\boldsymbol{\Theta}\times[0,1]$ be the ray space of a given step-index fibre.

- Let $p,q:\boldsymbol{\Theta}\to[0,1]$ be two deterministic functions on $\boldsymbol{\Theta}$ defined by:

$$p(\theta) = \begin{cases} \text{Fresnel power transmission coefficient} & , \theta\in\boldsymbol{\Theta}_0 \\ 1 & , \theta\in\boldsymbol{\Theta}\backslash\boldsymbol{\Theta}_0, \end{cases} \tag{2.97}$$

$$q(\theta) = 1 - p(\theta).$$

- Let $X^R, X^T:\boldsymbol{\Theta}\to\boldsymbol{\Theta}$ be two random mappings such that
  - for each $\theta\in\boldsymbol{\Theta}_0$ the random variables X_θ^R and X_θ^T are the Fresnel reflection or output points reached by the respectively reflected and transmitted rays in the successive steps of the raytracing procedure.
  - For $\theta\in(\boldsymbol{\Theta}\backslash\boldsymbol{\Theta}_0)$ let $X_\theta^R \equiv X_\theta^T \equiv \theta$ with probability 1.
- Let $A^R, A^T:\boldsymbol{\Theta}\to[0,1]$ be two random mappings such that
  - for each $\theta\in\boldsymbol{\Theta}_0$ the random variables A_θ^R and A_θ^T equal the relative power remaining in the reflected and transmitted rays at the points X_θ^R and X_θ^T, respectively, not taking into account the Fresnel power transmission coefficient $p(\theta)$ and the power reflection coefficient $q(\theta)$. A^R and A^T represent the bulk and interface attenuation of the traced ray in-between points θ and X_θ^R or X_θ^T.
  - For $\theta\in(\boldsymbol{\Theta}\backslash\boldsymbol{\Theta}_0)$ let $A_\theta^R \equiv 0$ and $A_\theta^T \equiv 1$ with probability 1.
- Let $Z:\boldsymbol{\Theta}\to\{0,1\}$ be a random mapping such that Z_θ is for each $\theta\in\boldsymbol{\Theta}$ a binary random variable with the probability of success $p(\theta)$, independent of X_ζ^R, X_ζ^T, A_ζ^R and A_ζ^T for each $\theta,\zeta\in\boldsymbol{\Theta}$. Note that

$$\mathrm{E}[Z_\theta] = p(\theta) \tag{2.98}$$

and that $Z_\theta \equiv 1$ with probability 1 for $\theta\in(\boldsymbol{\Theta}\backslash\boldsymbol{\Theta}_0)$. ■

NOTATIONAL CONVENTION As we will need deterministic rays as well as randomised rays, the random variables in the following will be told from the deterministic values by an underline or a capital letter, i.e. all random variables will be denoted with a capital letter (as in Definition 2.7) or will be underlined. According to this notation a deterministic ray $r = (\theta,\varepsilon)$ is an element of $\boldsymbol{\Theta}\times[0,1]$, while a random ray $\underline{r} = (\underline{\theta},\underline{\varepsilon})$ is a random variable on $\boldsymbol{\Theta}\times[0,1]$, which generally can but need not take a given value r with probability 1. ■

In the following, it will be assumed that each random ray is independent of X_ϑ^R, X_ϑ^T, A_ϑ^R, A_ϑ^T and Z_θ, so that fibre illumination does not depend on the raytracing mechanism.

Both raytracing processes of *Fig. 2.9* can be now formally defined using Definition 2.7:

DEFINITION 2.8. For each $\underline{r} = (\underline{\theta}, \underline{\varepsilon})$ (being a random variable in $\boldsymbol{\Theta} \times [0,1]$) let random variables $T(\underline{r})$, $R(\underline{r})$ and $S(\underline{r})$ be defined as follows:

$$\begin{aligned} T(\underline{r}) &:= \left(X_{\underline{\theta}}^{T}, \underline{\varepsilon} \cdot p(\underline{\theta}) A_{\underline{\theta}}^{T}\right), \\ R(\underline{r}) &:= \left(X_{\underline{\theta}}^{R}, \underline{\varepsilon} \cdot q(\underline{\theta}) A_{\underline{\theta}}^{R}\right), \\ S(\underline{r}) &:= \left(X_{\underline{\theta}}, \underline{\varepsilon} \cdot A_{\underline{\theta}}\right), \end{aligned} \tag{2.99}$$

where

$$\begin{aligned} X_{\theta} &:= Z_{\theta} X_{\theta}^{T} + (1 - Z_{\theta}) X_{\theta}^{R}, \\ A_{\theta} &:= Z_{\theta} A_{\theta}^{T} + (1 - Z_{\theta}) A_{\theta}^{R}. \end{aligned} \tag{2.100}$$

For each starting ray $\underline{r} = (\underline{\theta}, \underline{\varepsilon})$ the *exact raytracing process* P_n, $n \in \mathbf{N}$ is defined by:

$$\begin{aligned} P_0 &:= \{\underline{r}\}, \\ P_{n+1} &:= \bigcup_{\underline{r} \in P_n} \{T(\underline{r}), R(\underline{r})\}. \end{aligned} \tag{2.101}$$

And the *probabilistic raytracing process* Q_n, $n \in \mathbf{N}$ is defined as:

$$\begin{aligned} Q_0 &:= \underline{r}, \\ Q_{n+1} &:= S(Q_n). \end{aligned} \tag{2.102}$$

■

The random variables $T(\underline{r})$ and $R(\underline{r})$ are represented on *Fig. 2.9(a)* by the dashed and the solid arrows, respectively. The only kind of an arrow on *Fig. 2.9(b)* represents the variable $S(\underline{r})$. Now, when the processes are formally defined, its time to define what it does mean that the probabilistic process *soundly* models the exact one. Intuitively, it is enough that their measurable characteristics are the same. And this means mainly (see Part 2.3) the equality of the mean output power per endface area or per spherical angle in the same periods of time, which generalised leads to the mean output power per any borel subset of $\boldsymbol{\Theta}$.

DEFINITION 2.9. Two finite sets of random rays $\left\{ \underline{r_k^{(l)}} \middle| \underline{r_k^{(l)}} = \left(\underline{\theta_k^{(l)}}, \underline{\varepsilon_k^{(l)}}\right), k = 1,2,\ldots,N^{(l)} \right\}$, $l \in \{1,2\}$, are called *power equivalent* if and only if for each $n \in \mathbf{N}$ and each $M \in B(\boldsymbol{\Theta})$

$$\sum_{k=1}^{N^{(1)}} E\left[\underline{\varepsilon_k^{(1)}} \cdot \mathbf{1}_M\left(\underline{\theta_k^{(1)}}\right)\right] = \sum_{k=1}^{N^{(2)}} E\left[\underline{\varepsilon_k^{(2)}} \cdot \mathbf{1}_M\left(\underline{\theta_k^{(2)}}\right)\right], \tag{2.103}$$

where $B(\boldsymbol{\Theta})$ is the set of all borel subsets of $\boldsymbol{\Theta} \subset \mathbf{R}^8$. ■

DEFINITION 2.10. The exact and probabilistic processes P_n and Q_n ($n \in \mathbf{N}$) are said to be power equivalent if and only if for each starting ray $\underline{r} = (\underline{\theta}, \underline{\varepsilon})$ and for each $n \in \mathbf{N}$ the sets P_n and $\{Q_n\}$ are power equivalent. ■

As the fibre space $\boldsymbol{\Theta}$ is defined (in Definition 2.5) in a simple and obvious way, all necessary measurable optical characteristics of a fibre, so its far and near field profiles (for the definitions see Part 2.3), may be defined via borel sets on $\boldsymbol{\Theta}$. What is left to be shown is that both processes P_n and Q_n actually *are* power equivalent.

THEOREM 2.11. The exact and probabilistic raytracing processes P_n and Q_n ($n\in\mathbf{N}$) defined in Definition 2.8 are power equivalent.

PROOF: The power equivalence of the processes P_n, Q_n ($n\in\mathbf{N}$) will be shown inductively with respect to n.

(a) P_0 and Q_0 are power equivalent: It is directly implied by the fact, that both processes have the same starting ray.

(b) P_1 and Q_1 are power equivalent. Let the starting random ray be $\underline{r} = (\underline{\theta},\underline{\varepsilon})$ and let its probability density function[4] (pdf) be $f(\theta,\varepsilon) = f(r)$. Then

$$P_1 = \{T(\underline{r}), R(\underline{r})\} = \left\{\left(X^T_{\underline{\theta}}, \underline{\varepsilon}\cdot p(\underline{\theta})A^T_{\underline{\theta}}\right), \left(X^R_{\underline{\theta}}, \underline{\varepsilon}\cdot q(\underline{\theta})A^R_{\underline{\theta}}\right)\right\},$$

$$Q_1 = S(\underline{r})$$

and the mean power of Q_1 per any borel subset $M\in B(\boldsymbol{\Theta})$ is (Eq. (2.103) with n=1):

$$\begin{aligned}
&E\left[\underline{\varepsilon}\cdot A_{\underline{\theta}}\cdot \mathbf{1}_M\left(X_{\underline{\theta}}\right)\right] = \\
&= E\left[\underline{\varepsilon}\cdot\left(Z_{\underline{\theta}}A^T_{\underline{\theta}} + \left(1-Z_{\underline{\theta}}\right)A^R_{\underline{\theta}}\right)\cdot \mathbf{1}_M\left(Z_{\underline{\theta}}X^T_{\underline{\theta}} + \left(1-Z_{\underline{\theta}}\right)X^R_{\underline{\theta}}\right)\right] = \\
&= E\left[\underline{\varepsilon}\cdot\left(Z_{\underline{\theta}}A^T_{\underline{\theta}} + \left(1-Z_{\underline{\theta}}\right)A^R_{\underline{\theta}}\right)\cdot\left(Z_{\underline{\theta}}\cdot \mathbf{1}_M\left(X^T_{\underline{\theta}}\right) + \left(1-Z_{\underline{\theta}}\right)\cdot \mathbf{1}_M\left(X^R_{\underline{\theta}}\right)\right)\right] = \\
&= E\left[\underline{\varepsilon}\cdot\left(Z^2_{\underline{\theta}}A^T_{\underline{\theta}}\cdot \mathbf{1}_M\left(X^T_{\underline{\theta}}\right) + \left(1-Z_{\underline{\theta}}\right)^2 A^R_{\underline{\theta}}\cdot \mathbf{1}_M\left(X^R_{\underline{\theta}}\right) + \right.\right. \\
&\qquad \left.\left. + Z_{\underline{\theta}}\left(1-Z_{\underline{\theta}}\right)A^T_{\underline{\theta}}\cdot \mathbf{1}_M\left(X^R_{\underline{\theta}}\right) + Z_{\underline{\theta}}\left(1-Z_{\underline{\theta}}\right)A^R_{\underline{\theta}}\cdot \mathbf{1}_M\left(X^T_{\underline{\theta}}\right)\right)\right] = \\
&= E\left[\underline{\varepsilon}\cdot\left(Z^2_{\underline{\theta}}A^T_{\underline{\theta}}\cdot \mathbf{1}_M\left(X^T_{\underline{\theta}}\right) + \left(1-Z_{\underline{\theta}}\right)^2 A^R_{\underline{\theta}}\cdot \mathbf{1}_M\left(X^R_{\underline{\theta}}\right)\right)\right] = \\
&= E\left[\underline{\varepsilon}\cdot\left(Z_{\underline{\theta}}A^T_{\underline{\theta}}\cdot \mathbf{1}_M\left(X^T_{\underline{\theta}}\right)\right)\right] + E\left[\underline{\varepsilon}\cdot\left(\left(1-Z_{\underline{\theta}}\right)A^R_{\underline{\theta}}\cdot \mathbf{1}_M\left(X^R_{\underline{\theta}}\right)\right)\right] = \\
&= \int_{\Theta\times[0,1]} E\left[\varepsilon\cdot Z_\theta A^T_\theta\cdot \mathbf{1}_M\left(X^T_\theta\right)\middle|\underline{r} = r = (\theta,\varepsilon)\right] f(r)dr + \\
&\qquad + \int_{\Theta\times[0,1]} E\left[\varepsilon\cdot\left(1-Z_\theta\right)A^R_\theta\cdot \mathbf{1}_M\left(X^R_\theta\right)\middle|\underline{r} = r = (\theta,\varepsilon)\right] f(r)dr =
\end{aligned}$$

[4] Instead of a continuous distribution and its pdf, any probabilistic distribution could be taken. The proof would stay the same; only the integrals would become notationally more complicated, as they would have to be taken with respect to the induced measure on $\boldsymbol{\Theta}\times[0,1]$.

Because the random variables Z_θ are independent of X_ϑ^R, X_ϑ^T, A_ϑ^R and A_ϑ^T:

$$= \int_{\Theta\times[0,1]} E\left[\varepsilon \cdot p(\theta) A_\theta^T \cdot \mathbf{1}_M\left(X_\theta^T\right) \middle| \underline{r} = r = (\theta,\varepsilon)\right] f(r)dr +$$

$$+ \int_{\Theta\times[0,1]} E\left[\varepsilon \cdot q(\theta) A_\theta^R \cdot \mathbf{1}_M\left(X_\theta^R\right) \middle| \underline{r} = r = (\theta,\varepsilon)\right] f(r)dr =$$

$$= E\left[\underline{\varepsilon} \cdot p(\underline{\theta}) \cdot A_{\underline{\theta}}^T \cdot \mathbf{1}_M\left(X_{\underline{\theta}}^T\right)\right] + E\left[\underline{\varepsilon} \cdot q(\underline{\theta}) \cdot A_{\underline{\theta}}^R \cdot \mathbf{1}_M\left(X_{\underline{\theta}}^R\right)\right],$$

which is the mean power of P_1 per any borel subset $M \in B(\mathbf{\Theta})$.

(c) Assumed that

$$P_n = \left\{\left(\underline{\theta_k}, \underline{\varepsilon_k}\right) \middle| k = 1,2,\ldots,N\right\} = \left\{\underline{r_k} \middle| k = 1,2,\ldots,N\right\},$$

$$Q_n = \left(\underline{\theta_0}, \underline{\varepsilon_0}\right) = \underline{r_0}$$

are power equivalent:

$$\bigwedge_{M\in B(\Theta)} E\left[\underline{\varepsilon_0} \cdot \mathbf{1}_M\left(\underline{\theta_0}\right)\right] = \sum_{k=1}^{N} E\left[\underline{\varepsilon_k} \cdot \mathbf{1}_M\left(\underline{\theta_k}\right)\right], \tag{2.104}$$

we will prove that so are also

$$P_{n+1} = \left\{R\left(\underline{r_k}\right), T\left(\underline{r_k}\right) \middle| k = 1,2,\ldots,N\right\},$$

$$Q_{n+1} = S\left(\underline{r_0}\right).$$

The following notational conventions will be used:

- Let $f_k(\theta,\varepsilon)$ be for each $k \in \{0, 1, 2, \ldots, N\}$ the pdf of $\underline{r_k} = \left(\underline{\theta_k}, \underline{\varepsilon_k}\right)$.
- Let $f_\theta(\theta,\varepsilon)$ be for each $\theta \in \mathbf{\Theta}$ the pdf of $S((\theta,1)) = (X_\theta, A_\theta)$.
- Let $K_M(\theta)$ be for each $\theta \in \mathbf{\Theta}$ the mean power in $M \in B(\mathbf{\Theta})$ of $S((\theta,1)) = (X_\theta, A_\theta)$:

$$K_M(\theta) := E\left[A_\theta \cdot \mathbf{1}_M\left(X_\theta\right)\right] = \int_M \int_0^1 \varepsilon \cdot f_\theta(\omega,\varepsilon)\, d\varepsilon\, d\omega\,.$$

- Let $T_k(\theta)$ be for each $k \in \{0, 1, 2, \ldots, N\}$ the mean power of $\underline{r_k} = \left(\underline{\theta_k}, \underline{\varepsilon_k}\right)$ in point $\theta \in \mathbf{\Theta}$:

$$T_k(\theta) := \int_0^1 \varepsilon \cdot f_k(\theta,\varepsilon)\, d\varepsilon\,.$$

Using the above notation Eq. (2.104) can be rewritten as follows:

$$\forall_{M\in B(\Theta)} \int_M T_0(\theta)d\theta = \sum_{k=1}^{N}\int_M T_k(\theta)d\theta = \int_M \sum_{k=1}^{N} T_k(\theta)\,d\theta\,.$$

M is here any borel subset of $\boldsymbol{\Theta}$, so the above implies:

$$T_0(\theta) = \sum_{k=1}^{N} T_k(\theta)$$

with probability 1.

We will need also the following fact, directly implied by the definition of the power equivalence of sets (Definition 2.9):

- The relation of the power equivalence of sets is *transitive*, i.e. if (i) sets *A* and *B* are power equivalent and (ii) sets *B* and *C* are power equivalent, then (iii) sets *A* and *C* are also power equivalent.

Step *(b)* of the inductional proof directly implies that the sets $\{R(\underline{r_k}), T(\underline{r_k})\}$ and $\{S(\underline{r_k})\}$ are power equivalent. Thus, instead of considering P_{n+1} and $Q_{n+1,}$ it is enough to prove that $\{S(\underline{r_k}) | k = 1,2,\ldots,N\}$ and $\{S(\underline{r_0})\}$ are power equivalent. For each $M\in B(\boldsymbol{\Theta})$:

$$E\left[\underline{\varepsilon_0}\cdot A_{\underline{\theta_0}}\cdot \mathbf{1}_M\left(X_{\underline{\theta_0}}\right)\right] =$$

Because the random variables $\underline{\varepsilon_0}$ and $A_{\underline{\theta_0}}, X_{\underline{\theta_0}}$ are independent:

$$= E\left[\underline{\varepsilon_0}\cdot E\left[A_{\underline{\theta_0}}\cdot \mathbf{1}_M\left(X_{\underline{\theta_0}}\right)\right]\right] = E\left[\underline{\varepsilon_0}\cdot K_M\left(\underline{\theta_0}\right)\right] =$$

$$= \int_{\Theta}\int_0^1 \varepsilon\cdot K_M(\theta)\cdot f_0(\theta,\varepsilon)d\varepsilon\,d\theta = \int_{\Theta} K_M(\theta)\cdot\left[\int_0^1 \varepsilon\cdot f_0(\theta,\varepsilon)d\varepsilon\right]d\theta =$$

$$= \int_{\Theta} K_M(\theta)\cdot T_0(\theta)\,d\theta = \int_{\Theta} K_M(\theta)\cdot\sum_{k=1}^{N} T_k(\theta)\,d\theta = \sum_{k=1}^{N}\int_{\Theta} K_M(\theta)\cdot T_k(\theta)d\theta =$$

$$= \sum_{k=1}^{N}\int_{\Theta} K_M(\theta)\cdot\left[\int_0^1 \varepsilon\cdot f_k(\theta,\varepsilon)d\varepsilon\right]d\theta = \sum_{k=1}^{N}\int_{\Theta}\int_0^1 \varepsilon\cdot K_M(\theta)\cdot f_k(\theta,\varepsilon)d\varepsilon\,d\theta =$$

$$= \sum_{k=1}^{N} E\left[\underline{\varepsilon_k}\cdot K_M\left(\underline{\theta_k}\right)\right] = \sum_{k=1}^{N} E\left[\underline{\varepsilon_k}\cdot E\left[A_{\underline{\theta_k}}\cdot \mathbf{1}_M\left(X_{\underline{\theta_k}}\right)\right]\right] =$$

$$= \sum_{k=1}^{N} E\left[\underline{\varepsilon_k}\cdot A_{\underline{\theta_k}}\cdot \mathbf{1}_M\left(X_{\underline{\theta_k}}\right)\right].$$

■

2.3 Basic measurable optical characteristics of a fibre

Both approaches to light propagation presented in the previous parts of this chapter describe the mechanism and allow modelling of light transmission through an optical fibre. Both depend on a number of imperfection-related parameters (perturbations of the refractive index, roughness of the core-clad interface, mean free path length, scale of the bulk scattering, etc.). As there is no known way to estimate the exact numerical values of these parameters *a priori*, they must be found *a posteriori*, i.e. by comparison between simulation results and measurements (see Part 3.2.3). The basis for comparison must be such optical characteristic of a fibre that on one hand is relatively easy to measure and to simulate but on the other hand diverse enough. As only static and not time-related characteristics[5] of an optical fibre are considered here, there are two potential fibre characteristics: far- and near-field profiles, discussed in the following parts. In the implemented raytracing software (Chapter 3) only the far-field profile is used.

2.3.1 Far-field profile (FFP)

Far-field profile (FFP) of an optical fibre is the angular distribution of its output power per solid angle. It is measured far away from the fibre endface, at a distance much larger than the fibre's diameter, so that the angular differences of rays leaving the fibre at different points of the endface can be neglected.

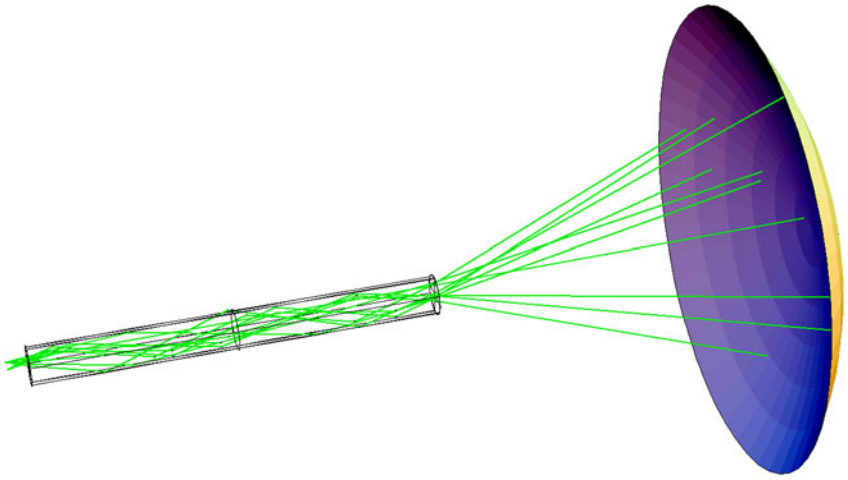

Fig. 2.10 *Illustration of the concept of the far-field profile (FFP) measurement.*

FFP is expressed in units of average power radiated into a solid radian. *Fig. 2.11* shows two sample FFP measurements. Further examples can be found in Part 6.3.

As it can be concluded from literature [10], FFP strongly depends on the

- illumination angle,
- POF type,
- sample length (see *Fig. 2.11*).

[5] As for example the bandwidth or the impulse-response characteristic of a fibre.

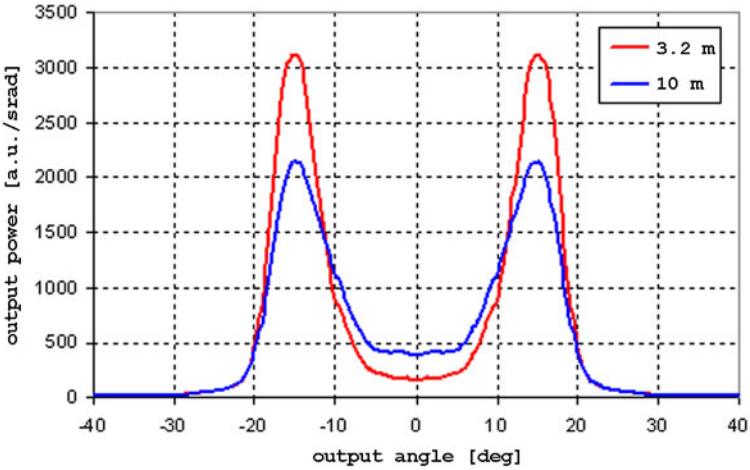

Fig. 2.11 *Influence of POF sample length on the FFP at the illumination angle 15°.*

Within the raytraced software discrete FFPs will be computed from rays leaving the endface of the simulated fibre as a mean output power per solid radian. Let the discretisation step equal $\Delta\alpha$ and let $S(\alpha,\alpha+\Delta\alpha)$ denote the total power of all rays leaving the fibre end face with inclination angle towards the axis within the interval $[\alpha,\alpha+\Delta\alpha)$. Then

$$FFP(\alpha,\alpha+\Delta\alpha)=\frac{S(\alpha,\alpha+\Delta\alpha)}{4\pi\sin\left(\frac{1}{2}\Delta\alpha\right)\sin\left(\alpha+\frac{1}{2}\Delta\alpha\right)}, \tag{2.105}$$

where the denominator equals the surface of a fragment of a sphere with radius 1 lying between α and $\alpha+\Delta\alpha$ angle.

2.3.2 Near-field profile (NFP)

Near-field profile (NFP) of an optical fibre is the local output power distribution of the light just after leaving the fibre endface (*Fig. 2.12*).

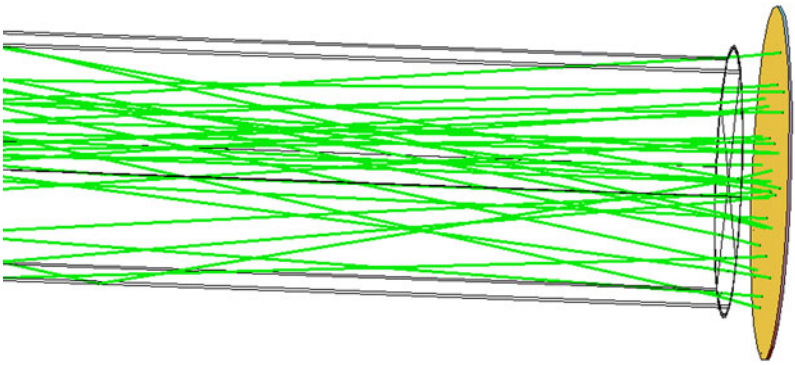

Fig. 2.12 *Few last steps of a raytracing procedure for several rays:The concept of the near-field profile (NFP) measurement.*

NFP is expressed in units of average density of output power on the endface surface. *Fig. 2.13* shows three sample simulated near-field profiles; the simulations were made with the software described in Chapter 3. The illumination angle was equal to 15° (the same as on *Fig. 2.11*), the input beam divergence was 0.35 mrad and the whole input face of a fibre (core and clad) was lighted. The imperfection-related parameters were assumed to be equal to those of the fitted non-aged Mitsubishi fibre (*Table 7.1*). The noise overlaid on the NFP curves should be attributed to the statistic dispersion of the results and gets smaller with the increasing number of traced rays. Note also that (if uniform ray distribution on fibre's endface assumed) the closer to the endface centre, the fewer rays are used for NFP computations and hence the more noise.

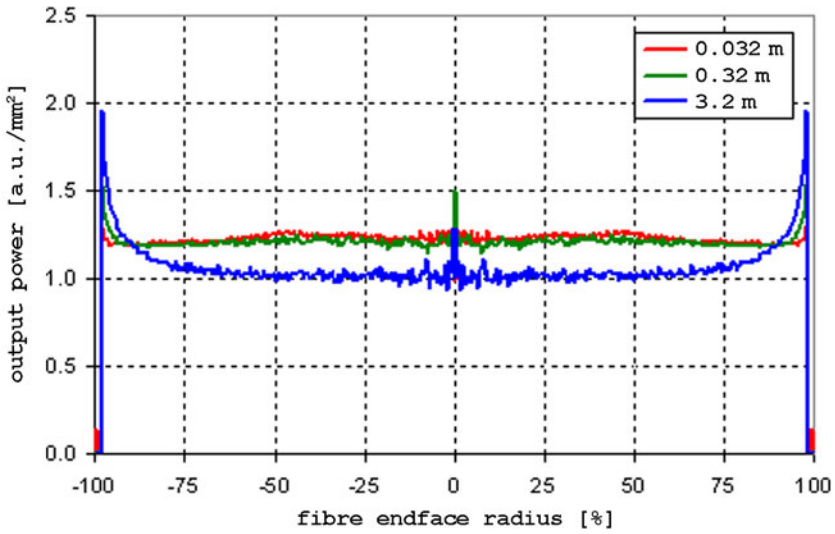

Fig. 2.13 *Three sample simulated near-field profiles of one POF type and different lengths. For each curve approx. 1 000 000 rays were traced.*

It has turned out that NFP is almost independent of fibre length and illumination angle. Thus, NFP seems to be unsuitable for fibre comparison purposes and will not be used for optimising and fitting the imperfection-related fibre parameters.

3 Simulation software

3.1 Commercially available software

Commercially available, scientific raytracing software can be in general divided into two groups: *sequential* and *non-sequential* raytracing software.

Sequential raytracing software is used for modelling and simulating the cases, in which the rays are traced through a predefined sequence of distinct optical objects, e.g. starting with a simulated light source generating several rays in approximately the same direction, refracted by a given lens no. 1, reflected then by a mirror and finally refracted by a lens no. 2. In this way traced rays may be collected on a projection screen and analysed in respect to their local distribution, optical path length, etc. A typical and widely used software form this group is the application package *Optica*, an extension tool to the well-known *Mathematica* from Wolfram Research [21].

Software packages belonging to the other group model the raytracing problems, in which the sequence of objects encountered by each traced ray is not or cannot be determined a priori, before the actual simulation of the ray path takes place. So, for example, some rays in the above-mentioned setup may miss the mirror but be nevertheless further traced towards other objects lying behind it, while a sequential raytracing software would just discard them as not matching the predefined sequence of encountered objects. This kind of general raytracing requires usually more sophisticated, versatile and costly software then simpler sequential systems. Similar raytracing procedures are also used by 3D lighting and scene-building graphical applications. The most known examples are the systems *CODE V* from Optical Research Associates [22] and *ASAP* from Breault Research Organization [23].

Implementing the raytracing procedure described in Part 2.2 would be potentially possible using both described kinds of commercial software, because the system consists of the light source and only one optical element, the modelled fibre. However, none of the available systems offers enough detailed control over the raytracing mechanism (angle-dependent intensity of the random scattering, reflection attenuation coefficients, etc.) to allow direct implementation of the developed model. Reprogramming would be possible in the case of *Optica*, but it would require deep intervention in the basic code of the package and the resulting software (as partly interpreted, not compiled) would be too slow to trace millions of rays in a reasonable amount of time. Thus, new specific software for fibre raytracing had to be developed.

3.2 Developed software

Developed software consists of three parts:

- Raytracing software library containing all the type definitions and the functions necessary for performing actual simulations.
- Graphical user interface, which allows entering values of the simulation parameters, passes them to the library and presents obtained simulation results (FFP, NFP, attenuation, etc.).

- Optimisation functions and their user interface, which allows entering the simulation parameters and measured FFPs, and communicates with the library for performing simulations to use the results in the optimisation process.

All three parts of the software were developed in Delphi environment from Borland Software Corporation [24], as it offers both code compilation (so high speed of its execution) and easy creation and management of the graphical user interface.

3.2.1 Raytracing software library

The raytracing library performs the simulation exactly as described in Part 2.2, according to the values of three groups of parameters: *setup*, *material* and *software*.

3.2.1.1 Setup parameters

Several *setup parameters* are required to define the physical properties of the simulation setup, i.e. of the simulated fibre and the light source. Their values, as describing the physical setup itself and not the optical properties of the fibre, are assumed to be given a priori, independent of the aging time, and are not optimised to get the best fit between simulated and measured FFPs (Part 3.2.3.1). Most important of the setup parameters are listed in *Table 3.1*.

Table 3.1 *Most important setup parameters.*

	parameter	type	remarks
fibre specific	*fibre length*	*real*	
	core diameter	*real*	
	fibre diameter	*real*	
	use clad tracing	*logical*	*Should rays be traced also in the clad?*
	model Fresnel reflection	*logical*	*Should Fresnel reflection modelling be used?*
	ray cut-off power level	*real*	*A ray is traced only until it leaves the fibre or its power falls below the cut-off level.*
illumination specific	*illumination angle*	*real*	
	light divergence	*real*	
	uniform illumination	*logical*	*Should uniform illumination (and not a Gaussian beam) be used?*
	beam horizontal diameter	*real*	
	beam vertical diameter	*real*	
	beam rotation	*real*	
	beam centre location	*(real, real)*	

3.2.1.2 Material parameters

The *material parameters* of the simulation describe the optical properties[6] of the simulated fibre and thus their values are optimised to get the best fit between simulated and measured FFPs (Part 3.2.3.2). Besides the parameters listed in *Table 2.2* (describing fibre attenuation) and *Table 2.3* (describing fibre scattering) they include also the *refractive indices* of fibre's core and clad, hence a total of 23. As an exact optimisation of all 23 independent parameters would be too time-consuming and thus practically impossible, the material parameters have been subjected to additional constraints, see Part 3.2.3.1.

3.2.1.3 Software parameters

The *software parameters* influence only the control of the simulation process and the display of its results, not the way the simulation is performed. The most important software parameters are:

- *Memory save*, a logical parameter. If true, the data of rays leaving fibre's endface (output point, power, direction) are stored only in an aggregate form. If false, all the output data of each ray (six 4-byte reals, i.e. 24 bytes for each ray) is stored. One million traced rays would produce then approx. 24 MB of output data for further processing.
- *Refresh step*, an integer. As refreshing the cumulative FFP/NFP graphs on the screen takes usually much more time than tracing a single ray through a typical fibre, it is reasonable to refresh the graphs only after several rays have been traced. This parameter defines the number of rays to trace before the simulation is temporary interrupted for displaying its updated results.
- *Rescale FFP*, a logical parameter. If true, the simulated FFP is rescaled to fit a given FFP and the fit quality is computed.

3.2.1.4 Simulation results

In each simulation step a total of *refresh step* (a software parameter, see Part 3.2.1.3) rays is traced. Then the library functions return the simulation results listed in *Table 3.2*.

Table 3.2 *Simulation results returned after each simulation step.*

parameter	type	remarks
FFP	*array of reals*	*simulated discrete FFP*
NFP	*array of reals*	*simulated discrete NFP*
transmitted rays	*array of array of reals*	*array of output rays' data (if save memory == false)*
no of traced rays	*integer*	*no of rays traced in this step*
no of transmitted rays	*integer*	*no of rays leaving fibre's endface*
backscattered power	*real*	
transmitted power	*real*	

[6] With the exception the *endface scattering* parameter of *Table 2.3*, which describes rather the quality of fibre endface polishing than the aging-affected material properties.

3.2.2 User interface for raytracing

Fig. 3.1 shows the user interface allowing for a direct use of the raytracing library. The upper part of the window contains controls used for manual parameter input; the lower part shows basic simulation results (transmitted and backscattered power, number of traced rays, average simulation speed in rays per second, etc.) and either simulated FFP/NFP or their simple smoothness measure based on the variation of the curves. The simulated FFP can be rescaled to match a reference FFP and the fit quality can be computed. During the execution the shown results are regularly refreshed, the FFP/NFP graph can be saved for future reference.

For the FFP simulation presented in *Fig. 3.1* as sample parameter values a fibre length of 3.2 m and an illumination angle of 15° were used; over a million of rays have been traced. *Fig. 3.2* shows the simulated NFP obtained during the same simulation.

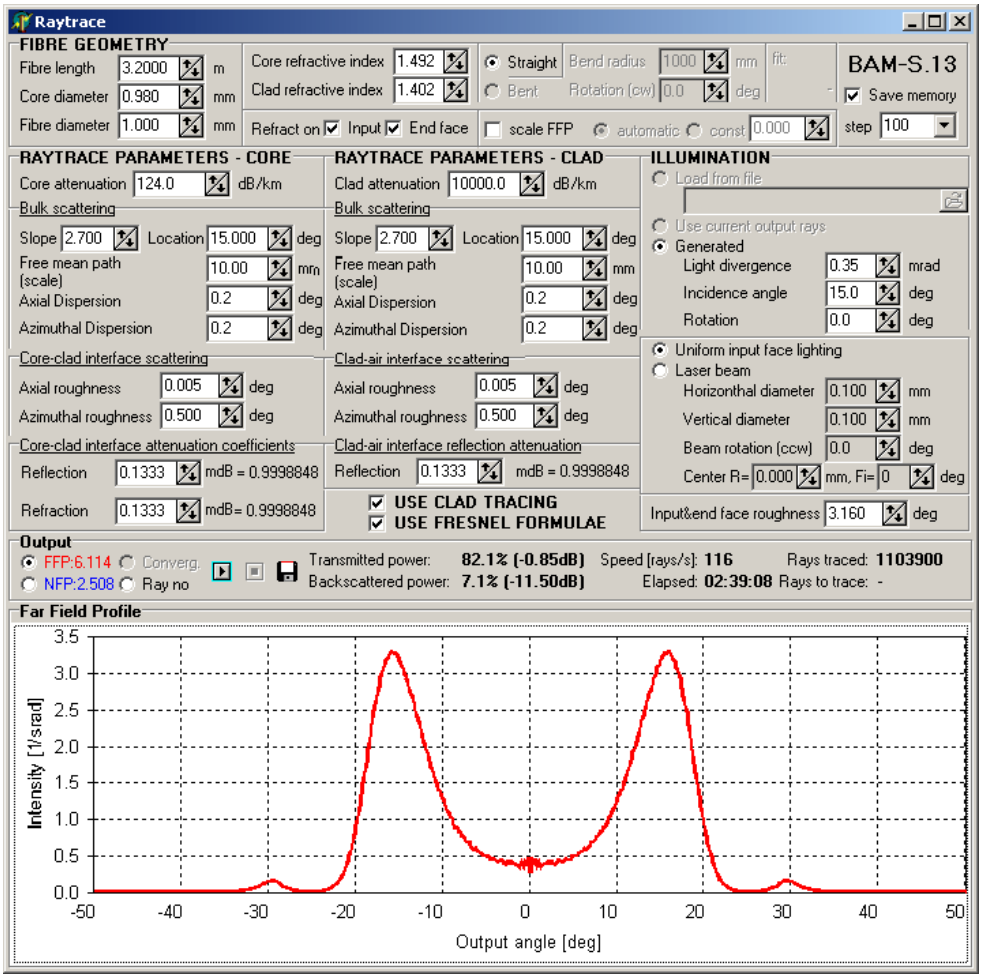

Fig. 3.1 *Graphical user interface of the raytracing library for the FFP simulation. Besides other parameters, 3.2 m fibre length, 15° illumination angle and over a million of traced rays have been used.*

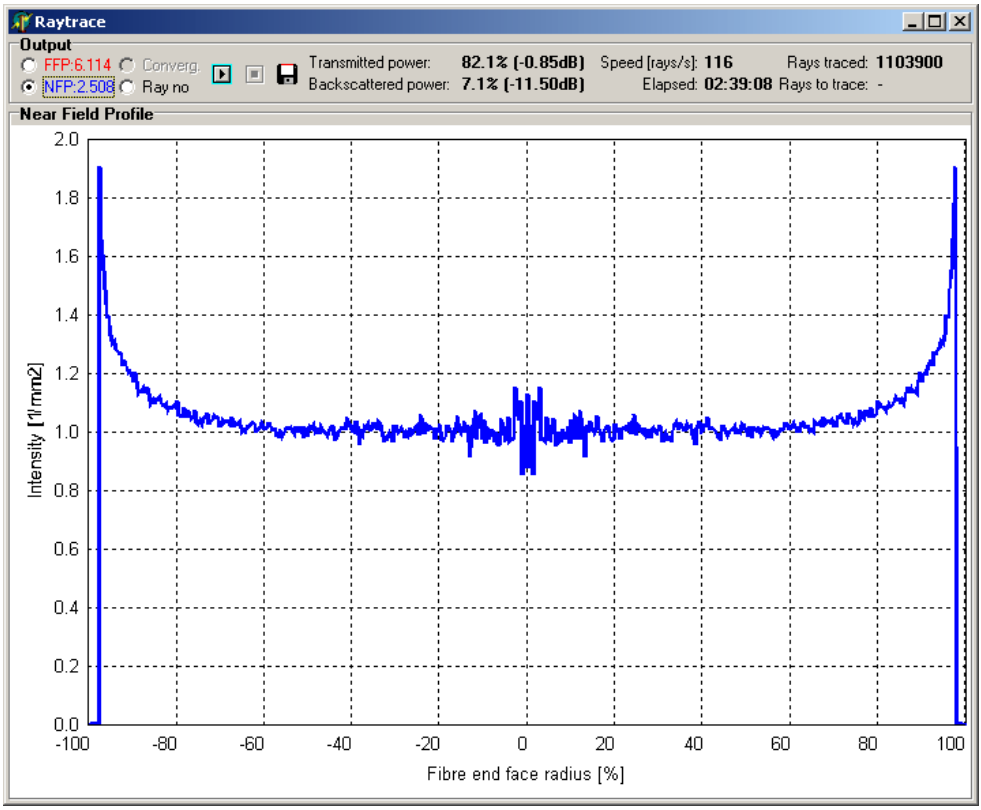

Fig. 3.2 *Simulated NFP corresponding to Fig. 3.1.*

3.2.3 Optimisation software

The graphical interface described in the previous part, although it allows to compute the (best-square-)fit quality of the simulated and reference FFPs, cannot be used for optimisation of the material parameters with the measured FFPs (Chapter 6) due to two following reasons:

- It allows for only manual and thus rough and non-systematic optimisation.
- It allows simulating and comparing with the reference of only one FFP at a time. For better optimisation results, several FFPs of each investigated fibre type, differing only in the length of the measured sample and its illumination angle (see Chapter 6), have been measured.

Thus, another software had to be developed for performing the semi-automatic optimisation of fibre's material parameters (Part 3.2.1.2), capable of using several measured FFPs simultaneously.

3.2.3.1 Setup parameters

The setup parameters mentioned in Part 3.2.1.1 and listed in *Table 3.1* have been divided into two groups: those common to all measured fibre samples and those specific to each

FFP measurement. Assumed to be common to all measured samples and thus constant are the following:

- Fibre core diameter: a value of 0.98 mm, as typical for POFs, has been used.
- Fibre diameter: a value of 1 mm, as typical for POFs, has been used.
- Use clad tracing: true. Rays in all simulations were traced also in fibre's clad.
- Model Fresnel reflection: true. The Fresnel reflection was modelled according to the mechanism described in Part 2.2.3.
- Ray cut-off power level: 10^{-4}. Each ray was traced until it left the fibre or its power fell below 0.01 % of the initial level.

The rest of the setup parameters describe the conditions of each measurement and thus have to be given separately for each FFP measurement, even if some of them happen to be the same for all samples:

- Fibre length: approx. 0.8 m, 3.2 m or 10 m, see Parts 6.1 and 6.2.
- Illumination angle: 6°, 15° or 24°, see Part 6.2.
- Light divergence: 0.35 mrad, see Part 5.2.
- Uniform illumination: true. As the diameter of the laser beam used was 3 mm to 4 mm (Part 5.2), it was assumed that the illumination intensity over 1 mm POF input face is sufficiently uniform. Thus, the setup parameters related to the illuminating beam do not apply.

Fig. 3.3 shows the part of the user interface of the optimisation software used for the input of setup parameters and corresponding measured FFPs.

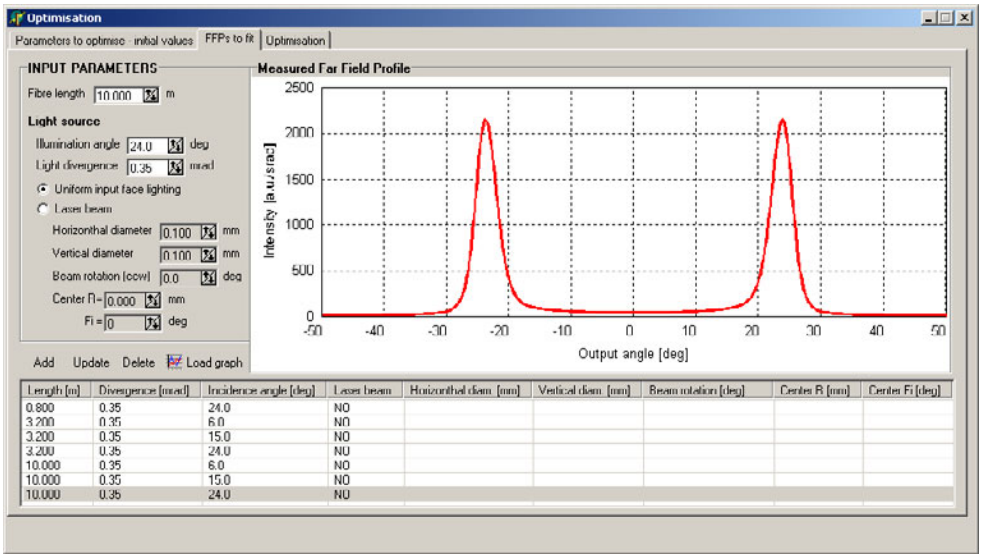

Fig. 3.3 *Optimising software. Input of setup parameters and corresponding measured FFPs.*

3.2.3.2 Constraints on optimised material parameters

Altogether there are 23 material parameters that describe optical properties of a fibre (Part 3.2.1.2). To get the best fit between the measured and simulated FFPs the values of all of them should be optimised. However, optimising the fit-quality function (see Part 3.2.3.3) in 23 independent variables would be too time-consuming to make the procedure practical. Thus, several constraints had to be enforced on the possible values of the parameters, leading to the total of six independent optimisation variables listed in *Table 3.3*.

Table 3.3 *Optimisation variables used and their relation to the material parameters.*

variable no.	variable name	relation to fibre's material parameters
var1	*endface scattering*	*= endface scattering*
var2	*core bulk attenuation*	*= core bulk attenuation*
var3	*interface attenuation*	*= core-clad reflection attenuation* *= core-clad transmission attenuation* *= clad-air reflection attenuation* *= clad-air transmission attenuation*
var4	*scattering scale*	*= core bulk scattering scale* *= clad bulk scattering scale* *('A' parameter in Eq. (2.87))*
var5	*scattering slope*	*= core bulk scattering slope* *= clad bulk scattering slope* *('κ' parameter in Eq. (2.87))*
var6	*scattering slope location*	*= core bulk scattering slope location* *= clad bulk scattering slope location* *('θ' parameter in Eq. (2.87))*

The six optimisation variables defined in this way describe 12 of 23 material parameters. The 11 parameters left were assumed to be constant and their values were not optimised for the following reasons:

- *clad bulk attenuation* = 10 000 dB/km

  The most of the transmitted rays cover almost all the way to the endface of the fibre within its core, guided through a chain of successive total internal reflection on the core-clad interface. Thus, the main medium for light transmission is the core, not the clad, and the exact value of clad bulk attenuation does not seem to be decisive. The value of 10 000 dB/km is mentioned in Daum et al. [10].

- *core-clad interface axial scattering = core-clad interface azimuthal scattering = clad-air interface axial scattering = core-air interface azimuthal scattering* = 0.

  As stated in Part 2.2.2, the intensities of both interface and bulk scattering processes are dependent on the propagation angle of a ray. The formula Eq. (2.86) for the

angle-dependent intensity of the bulk scattering allows for a relatively free choice of its shape. Therefore, it will be assumed that its shape accounts also for the influence of the interface scattering and thus the only parameters needed for modelling of the scattering remain the parameters A, κ and θ of Eq. (2.86) (*var4*, *var5* and *var6*).

- *core bulk scattering axial dispersion* =
  = *core bulk scattering azimuthal dispersion* =
  = *clad bulk scattering axial dispersion* =
  = *clad bulk scattering azimuthal dispersion* =
  = 0.2°

  In general, the (optimised) scale parameter of the bulk scattering (i.e. A in Eq. (2.87)) defines how many times a ray is scattered on its way through fibre, while the four angular dispersion parameters here define by which angle it is each time scattered. Thus, as in practice each ray is scattered numerous times, both groups of parameters define the angular dispersion of the scattered power, which depends linearly on angular dispersion parameters and is proportional to the square root of the mean number of ray redirections (the reciprocal of the mean free path, depending on the scale parameter). Hence, scale and angular dispersion parameters are substitutive and it is sufficient to optimise the value of only one of them, which was also experimentally confirmed in a simpler raytracing model [15]. The value of 0.2° was experimentally found to correspond to a reasonable optimised value of the parameter A.

- The refractive index of fibre's core was assumed to be 1.492, a typical value for PMMA.

- The refractive index of fibre's clad was each time computed using Eq. (2.82) and the value of fibre's numerical aperture NA (*Table 4.2*) given by the manufacturer. As a result, the following values were used: 1.402 for Mitsubishi's fibres, 1.411 for Asahi's fibres and 1.406 for Toray's fibres.

3.2.3.3 Optimisation procedure

A semiautomatic optimisation procedure based on the Powell's Direction Set Method [6] has been implemented and used to optimise the values of the six variables *var1* to *var6* (Part 3.2.3.2) to obtain the best fit between the computed and measured FFPs.

In each step of the optimisation procedure FFPs have been simulated for the actual values of *var1* to *var6* using the same setup parameters (Part 3.2.3.1) as that of the measured fibre samples. The target function $d(var1,\ldots,var6)$ to be minimised was the sum of the normalised square differences between the measured and simulated two-dimensional FFPs[7], rescaled to get the best fit between the two:

[7] Obtained from their one-dimensional representation, thus constant on the rings of $\Delta\alpha = 0.2°$ width.

$$d(var1,\ldots,var6) := \sum \frac{\int_{\Omega} \left(FFP_{measured} - \vartheta \cdot FFP_{simulated}\right)^2 ds}{\left[\int_{\Omega} FFP_{measured}\, ds\right]^2} =$$

(3.1)

$$= \sum \frac{\sum_{\alpha=0}^{\frac{\pi}{4}-\Delta\alpha} 4\pi \sin\left(\frac{1}{2}\Delta\alpha\right)\sin\left(\alpha+\frac{1}{2}\Delta\alpha\right)\left[FFP_{measured}\left(\alpha,\alpha+\frac{1}{2}\Delta\alpha\right) - \vartheta \cdot FFP_{simulatedd}\left(\alpha,\alpha+\frac{1}{2}\Delta\alpha\right)\right]^2}{\left[\sum_{\alpha=0}^{\frac{\pi}{4}-\Delta\alpha} 4\pi \sin\left(\frac{1}{2}\Delta\alpha\right)\sin\left(\alpha+\frac{1}{2}\Delta\alpha\right) FFP_{measured}\left(\alpha,\alpha+\frac{1}{2}\Delta\alpha\right)\right]^2},$$

where Ω is the fragment of a unit sphere with its origin in the middle of the fibre output face and extending up to 45° (i.e. the detectable angular range of the FFP optics) out of the fibre axis. For the meaning of the weighting coefficients in the second term see Eq. (2.105). The non-indexed sum in Eq. (3.1) denotes the sum over all different measured and simulated samples for the current fibre and the scaling factor ϑ has the value that minimises the target function, i.e.:

$$\vartheta := \underset{\vartheta \in \mathbf{R}_+}{\arg\min}\, d(var1,\ldots,var6). \tag{3.2}$$

Rescaling of the simulated FFPs with the factor ϑ was necessary because the measured FFPs are expressed in a.u. / srad and those arbitrary units cannot be related to the unknown total power incident on the fibre's input face, as it is the case with the simulated FFPs. Nonetheless the attenuation parameters can be optimised thanks to the use of different fibre lengths.

Note that the target function Eq. (3.1) compares two-dimensional FFPs and thus puts more weight on the tails of the corresponding one-dimensional curves, which can be generally observed on measured and fitted graphs in Appendix A3: the higher is the output angle, the better the fit of both curves.

Simulated FFPs are in fact obtained from a Monte Carlo procedure and thus each computed value of the target function d contains some amount of noise disturbing its minimisation process. The more rays traced, the less gets the noise and the more exact is the optimisation procedure but also the longer time it demands. Thus, the best-fitting values of the variables $var1$ to $var6$, describing the optical properties of an investigated fibre, are always loaded with some amount of uncertainty (*Table 7.4*), which represents the trade-off between the optimisation time and its accuracy.

4 Aging process and POF samples

In this chapter we give a short overview of the material loss mechanisms in POFs and of fibre aging (Part 4.1), discuss their influence on the raytracing model (Part 4.2), specify the fibres used (Part 4.3), describe the applied aging conditions and show sample online measurements of relative fibre transmission under long-term environmental stress (Part 4.4).

4.1 Loss mechanisms in POF and fibre aging

POF during its service time is often subjected to different types of environmental stresses, which result in changes of its chemical and physical properties. This is called aging. Most important in respect to the deterioration of optical properties are long-term influences of high temperature, high humidity, freezing, radiation, and mechanical or chemical stress.

See Daum et al. [10, Chapter 8] for a general discussion of the reliability of POFs, for measurement methods to trace the influence of environmental stresses, for reports on several reliability investigations made under various stress conditions, for a description of standardisation efforts and for numerous references.

Loss factors of optical transmission in a commercially available POF can be divided into those specific to the material itself (intrinsic) and those related to fibre imperfections or impurities (extrinsic). They are further categorised as shown in *Table 4.1*.

Table 4.1 *Loss factors in POFs [10, 17].*

Intrinsic loss factors	Absorption	• *high harmonics of the C-H bondings* • *electron transitions*
	Scattering	• *Rayleigh scattering*
Extrinsic loss factors	Absorption	• *organic contaminants* • *water absorption* • *transition metals*
	Scattering	• *microcracks* • *fluctuations of the core diameter* • *core-clad interface imperfections*

The influence of the aging process on the loss factors will not be discussed in detail in this research. It is treated parallel to this work, in another thesis at the Federal Institute for Materials Research and Testing (BAM) by A. Appajaiah. He investigates the material aspects of high temperature and high humidity aging [see 33-36]. Further literature is given in [17], too.

4.2 Aging influence on raytracing model

In a real fibre as well as in a modelled one that imitates it, passing light encounters two main imperfection-related processes: attenuation and scattering. Both processes can be described in two ways:

I. Using the terms belonging to the geometric or wave optics, as in Chapter 2 and Appendix A2, so that the overall influence of attenuation and scattering on fibre optical properties and light propagation could be computed or simulated, which is one of the goals of this work.

II. But they can also be described using rather chemical than optical terms, as in *Table 4.1* and in the above-mentioned thesis of A. Appajaiah [see 33-36]. This approach allows better understanding of the environmental influence on fibre material itself but it is harder to relate its terminology and findings to fibre's optical properties.

In this work we deal mainly with simulation of light propagation, so the terminology of the first approach will be used. Because it is reasonable to assume that the raytracing mechanism itself does not change under environmental influences, its parameters have to change. The raytracing parameters listed and explained in Part 2.2 will be (as it is described in the beginning of Part 2.3) found for each investigated fibre separately, by comparison of the measured and simulated FFPs (Chapter 7). Thus, by tracing changes of the values of the model parameters between initially the same fibres but subjected to different environmental conditions or different aging times, the following aging-related alteration can be found:

- Aging of the fibre bulk material, traced via its modelled
  - scattering (the left column of the *Table 2.3*) and
  - attenuation properties (the left column of the *Table 2.2*).
- Degradation of the core-clad interface, traced via the modelled
  - interface scattering (the middle column of the *Table 2.3*) and
  - interface attenuation coefficients (the right column of the *Table 2.2*).

For the results and discussion see Chapter 7.

4.3 POF samples

For the experimental part of the work commercially available PMMA-based POFs of 1 mm diameter from three leading manufacturers were bought and used:

- Mitsubishi Rayon Co., fibre ESKA CK-40,
- Asahi Chemicals Inc., fibre LUMINOUS TB-1000,
- Toray Industries Inc., fibre PGU-FB 1000.

All three fibres were bought bare (core and clad only, no jacket) to trace the pure influence of the environmental conditions during the aging tests, not disturbed by the presence of the protective layer of jacket. The nominal basic technical data of all three fibres are very similar and listed as given by the manufacturers in *Table 4.2*, together with the measured attenuation value at 650 nm for comparison. For its measurement a broad-spectrum light source was used and a Sentronic S2000 miniature spectrometer [37]. The light was

launched into measured samples using a 0.8 mm diameter, high NA silica fibre directly illuminating the POF input face.

Table 4.2 *Basic technical data of the fibres used in investigations.*

	ESKA CK-40	LUMINOUS TB-1000	PGU-FB 1000
∅	*1 mm*	*1 mm*	*1 mm*
core material	*PMMA*	*PMMA*	*PMMA*
clad material	*fluoropolymer*	*fluoropolymer*	*fluoropolymer*
numerical aperture NA	*0.51*	*0.485±0.05*	*0.50*
acceptance angle α_{max}	*30.7°*	*29.0°*	*30.0°*
nominal attenuation at 650 nm	*0.20 dB/m*	*0.16 dB/m*	*0.15 dB/m*
measured attenuation at 650 nm	*0.14 dB/m*	*0.14 dB/m*	*0.16 dB/m*

Mitsubishi's fibre's numerical aperture value of 0.51 corresponds to the typical combination of PMMA-core refractive index of 1.492 and clad refractive index of 1.402. Those typical values are used in all numerical investigations of Appendix A2, as stated in Eq. (A2.1). *Fig. 4.1* shows the spectral attenuations of all three non-aged fibres measured using 10 m polished-end samples with a Sentronic S2000 miniature spectrometer [37].

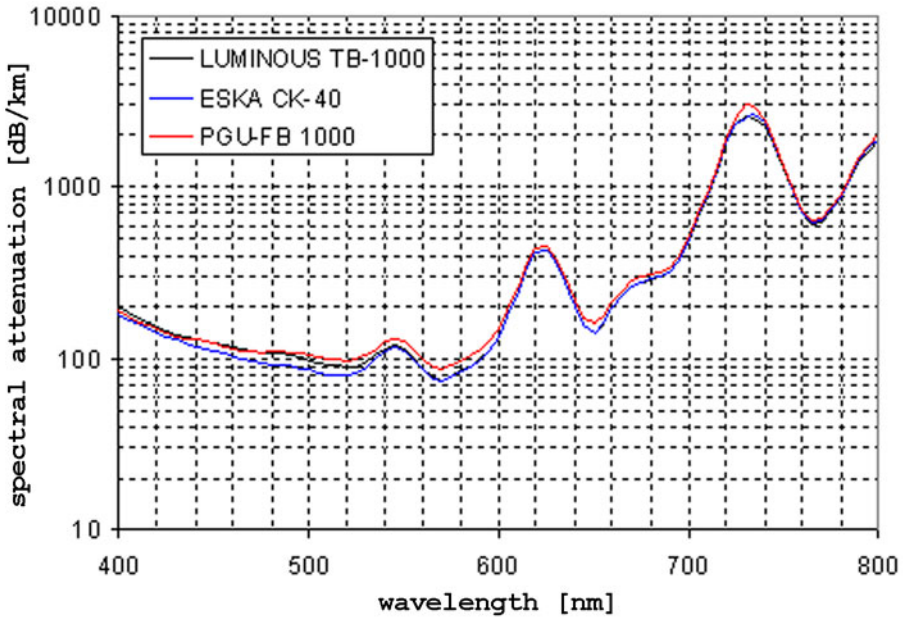

Fig. 4.1 *Measured spectral attenuations of 10 m non-aged fibres.*

4.4 Aging conditions

Five samples of all three fibre types were subjected to accelerated aging using specialised climatic chambers, ovens and the following conditions:

- total fibre length 13 m, aged fibre length 10 m;
- dry heat conditions (80 °C, 90 °C, 95 °C and 100 °C), i.e. high temperature without humidity control (<<50 % RH) or
- high temperature combined with high humidity (92 °C / 95 % RH, 92 °C / 50 % RH).

All tests went on for 3000 h to 4500 h. During the whole aging processes online transmission measurements of the hot fibres were automatically performed with the help of the multiplexer measurement system [19]:

- in 10 min steps,
- using three LEDs with spectra centred at: 525 nm (green), 590 nm (yellow) and 650 nm (red) wavelengths.

Fig. 4.2 to *Fig. 4.6* show sample results of obtained measurements. Note that the transmission measurements were done online, during exposure[8], and thus they differ from the values that are obtained from the fibres cooled down to the room conditions[9], for the comparison of both see *Fig. 4.20*.

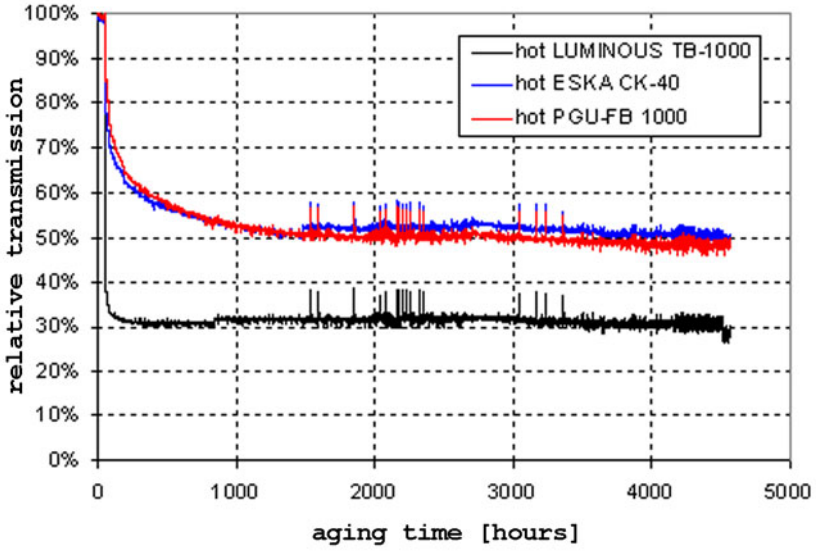

Fig. 4.2 *Relative online transmission of 10 m hot samples (i.e. during exposure) of investigated fibres at 650 nm wavelength and under 100 °C / <<50 % RH.*

The transmission of the fibres subjected to the 80 °C / <<50 % RH stress has stayed practically constant or dropped only very slightly during the whole test (*Fig. 4.3*). The temperature of 92 °C combined with 95 % relative humidity (*Fig. 4.5*) has caused the transmission of all fibres to drop completely within the first hours of the test, while keeping

[8] Fibres during exposure will be henceforth referred to as the 'hot' fibres.

[9] Henceforth referred to as the 'cold' fibres.

the temperature at 92 °C but decreasing the relative humidity to 50 % has allowed the transmission (at least in the commonly used 650 nm region) to stay relatively high through the whole test time, see *Fig. 4.5* and *Fig. 4.6*.

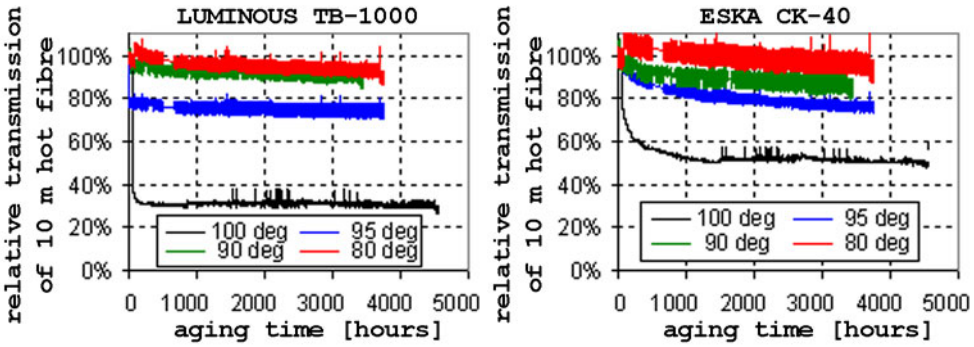

Fig. 4.3 *Relative online transmission of the 10 m Asahi's (left) and Mitsubishi's (right) fibres at 650 nm wavelength in dry heat conditions, i.e. 80 °C, 90 °C, 95 °C and 100 °C without humidity control (<<50 % RH).*

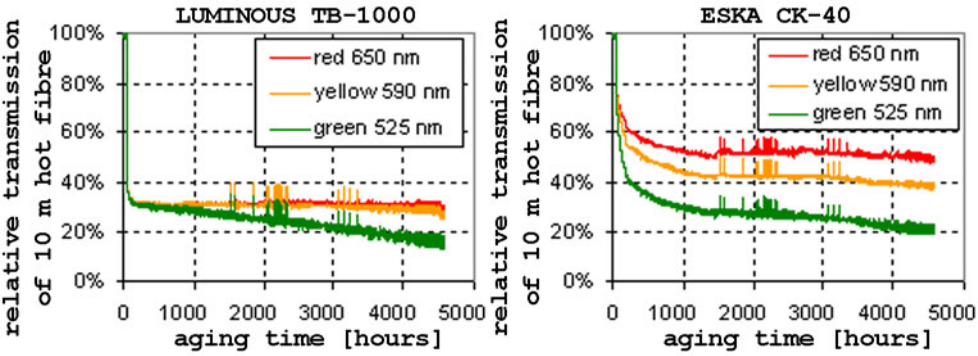

Fig. 4.4 *Relative online transmission of the 10 m Asahi's (left) and Mitsubishi's (right) fibres at three wavelengths under 100 °C / <<50 % RH.*

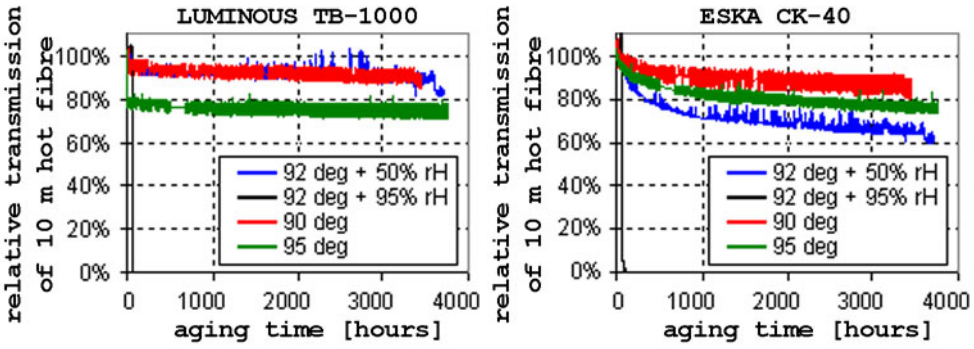

Fig. 4.5 *Relative online transmission of the 10 m Asahi's (left) and Mitsubishi's (right) fibres at 650 nm wavelength under 90 °C to 95 °C, without humidity control (dry heat, i.e. <<50 % RH) and with high relative humidity (50 % RH, 95 % RH).*

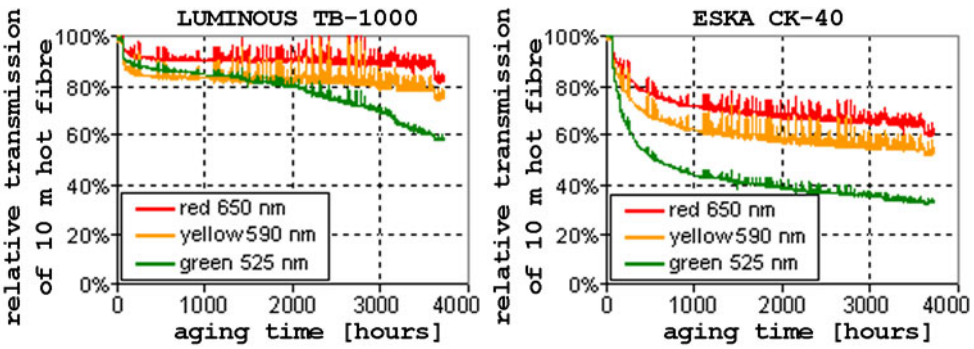

Fig. 4.6 *Relative online transmission of the 10 m Asahi's (left) and Mitsubishi's (right) fibres at three wavelengths under 92 °C and with 50 % relative humidity.*

4.4.1 Sample preparation

Because the main purpose of this research was to develop and to validate the model for light propagation in POFs, capable of describing the aging-related changes, as typical examples, besides the non-aged fibres, only the samples obtained during the 100 °C / <<50 % RH aging were used for further investigations (Chapters 6 and 7). *Table 4.3* lists the respective aging times. At each time given in the table, a set of three fibre samples, one for each manufacturer, has been taken out of the oven and kept for attenuation and FFP measurements, resulting in a total of 18 fibre samples.

Table 4.3 *Aging times of POF samples used for further optical investigations.*

Aging time (100 °C / <<50 % RH) of the sample sets used for investigations
sample set 0: 0 h (fresh, non-aged fibre)
sample set 1: 2 h
sample set 2: 258 h
sample set 3: 677 h
sample set 4: 1393 h
sample set 5: 4467 h

After cooling down to room temperature (about 25 °C) each of those 18 fibre samples had been cut into three pieces of the length of approx. 0.8 m, 3.2 m and 10 m. The endfaces of the pieces were polished using several abrasive papers with a grade down to 0.1 μm. As a result 54 fibre samples with fine-polished endfaces were prepared for FFP measurements (Chapter 6). The 10m-pieces were used for measuring the spectral attenuations with a Sentronic S2000 miniature spectrometer [27], too. The results of the latter are given in *Fig. 4.7* to *Fig. 4.9*.

Note that the attenuation of the cooled down fibres in the usable wavelength ranges seems to stay approximately constant or even *decrease* (Asahi's fibre, *Fig. 4.7* and *Fig. 4.9*) with the aging time (between *set2* and *set4*). This astonishing behaviour is confirmed with the total transmission measurements obtained in Chapter 6 (*Fig. 6.11* to *Fig. 6.16*).

Fig. 4.10 to *Fig. 4.12* compare the relative transmission of the hot fibre samples (*Fig. 4.2*) with the relative transmission of the cooled down samples.

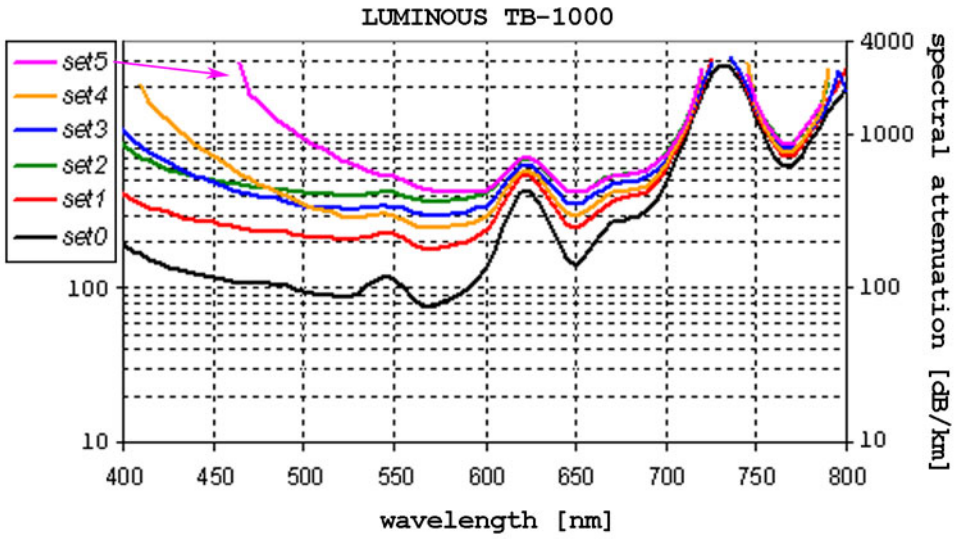

Fig. 4.7 *Attenuation of the 10 m sample of Asahi's fibre at different aging times (Table 4.3) in the 100 °C / <<50 % RH conditions.*

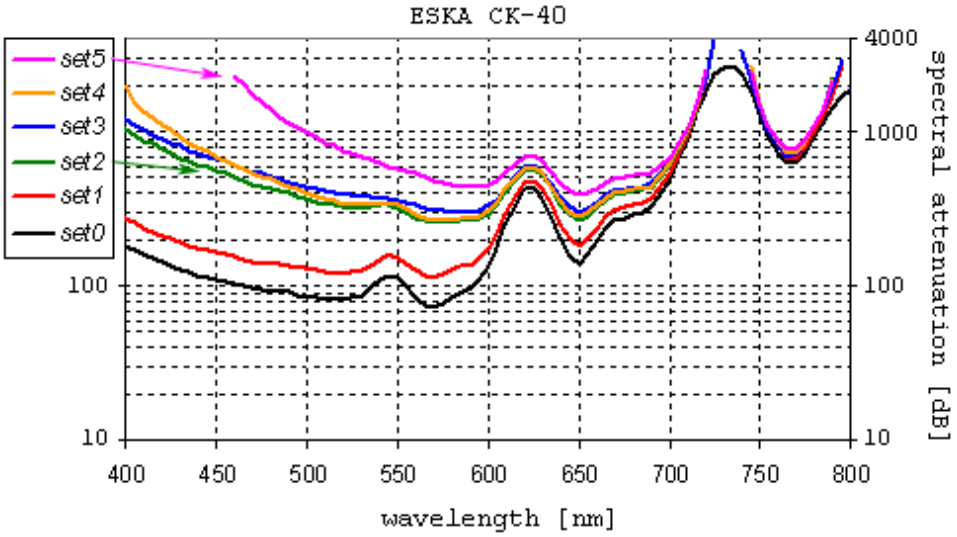

Fig. 4.8 *Attenuation of the 10 m sample of Mitsubishi's's fibre at different aging times (Table 4.3) in the 100 °C / <<50 % RH conditions.*

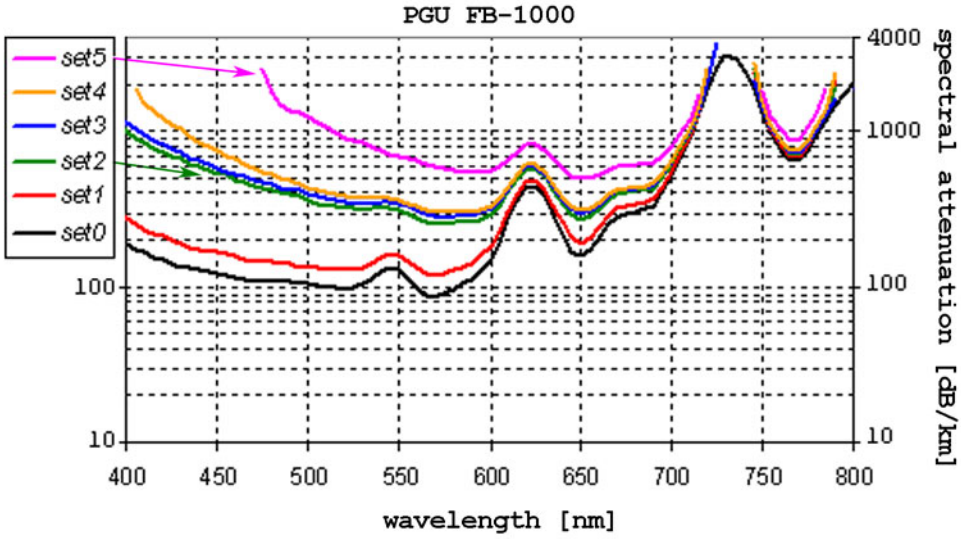

Fig. 4.9 *Attenuation of the 10 m sample of Toray's fibre at different aging times (Table 4.3) in the 100 °C / <<50 % RH conditions.*

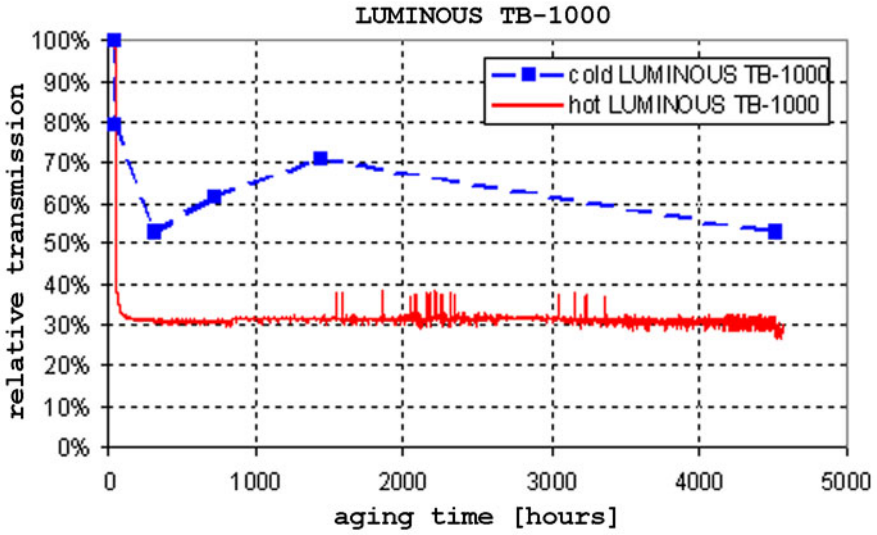

Fig. 4.10 *Relative transmission of the hot (online) and the cold (cooled down) 10 m sample of Asahi's fibre at 650 nm wavelength and under 100 °C / <<50 % RH.*

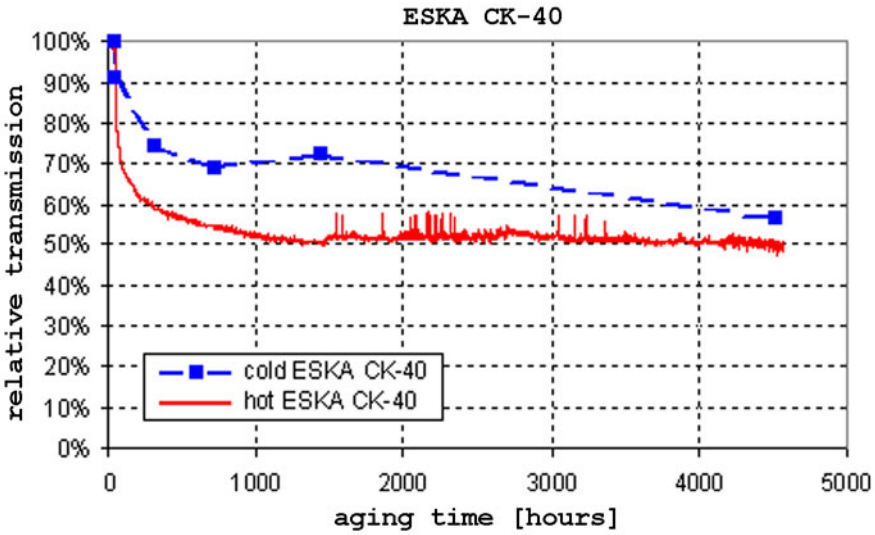

Fig. 4.11 *Relative transmission of the hot (online) and the cold (cooled down) 10 m sample of Mitsubishi's fibres at 650 nm wavelength and under 100 °C / <<50 % RH.*

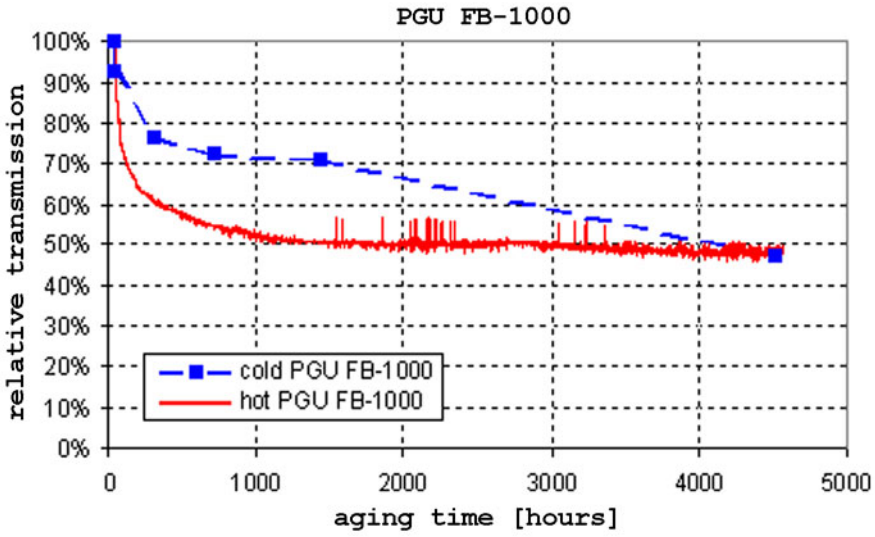

Fig. 4.12 *Relative transmission of the hot (online) and the cold (cooled down) 10 m sample of Toray's fibres at 650 nm wavelength and under 100 °C / <<50 % RH.*

5 Experimental instrumentation for FFP measurements

In Part 2.3 the near- and far-field profiles of an optical fibre were discussed and the far-field profile (FFP) was chosen as the enough general and diverse fibre characteristic to be used for the comparison of simulated and real POFs, as in [11, 15, 16]. The simulation software described in Chapter 3 uses the formula Eq. (2.105) for computing the FFP of a simulated fibre. The FFP of a real fibre must however be measured. In this chapter the measurement setup, the necessary instrumentation, its reliability and calibration is discussed.

5.1 General measurement setup

To get enough complete characteristics of a POF, either aged or non-aged, its far-field profile has to be measured in dependence on

- incidence angle of an illuminating beam,
- fibre length.

Fig. 5.1 schematically depicts the setup used for FFP measurements [see 38-40]. A red laser is used for POF illumination; a specialised far-field optics translates the angular characteristic of fibre output power to spatial coordinates, needed for illumination of the flat CCD sensor of the CCD camera. The CCD camera output is then processed to obtain the FFP using the procedure described in Part 6.3.

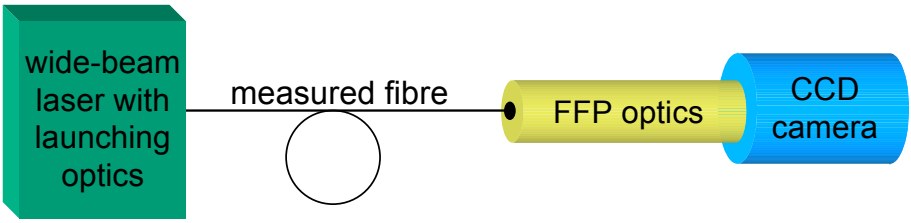

Fig. 5.1 *Principle of the measurement setup.*

The measurement setup outlined on *Fig. 5.1* has resolved basic contradiction between time efficiency and accuracy of other possible techniques for far-field measurement, but has also created new problems:

- *It is time-effective*. Due to the huge number of measurements (several combinations of illumination angle, fibre length, fibre type/manufacturer and aging time) the traditional scanning (goniophotometric) measurements turned out to be too time-consuming. Therefore, it was decided to use a CCD camera with 1024×1024 cells (meaning a simultaneous measurement of $>10^5$ points of FFP), as it allows taking measurement with a limited number of short single snaps.
- *It is accurate in respect to the illumination*. The CCD camera's reliability had to be investigated. As there is no obvious literature on calibration and reliability of CCD cameras, a procedure for their quality assessment and calibration had to be developed (Part 5.3). A common measurement problem of standard CCD cameras, i.e. too small dynamic range, may be overcome by combining several measurements taken with different exposure times, as described in Part 5.3.4.
- *It is accurate in respect to the angular resolution*. Using a bare CCD sensor with a direct illumination provides first at the distance to the fibre endface of approx. 12 mm

the sufficient angular part of the FFP ($\pm\alpha_{max} \approx 30°$) but already too small angular resolution (approx. 4.7° for the fibre of 1 mm diameter). A specialised FFP optics with much higher angular accuracy (at least 0.5°) became available recently. However, optics' reliability, i.e. its angular distortion and stability of resolution, had to be investigated, too (Part 5.4).

5.2 Laser

As a light source for POF illumination a laser diode DLS 15 from LINUS was used with the following optical properties:

- Wavelength: 653 nm at 20 °C.
- Beam divergence: 0.3 mrad to 0.4 mrad (0.017° to 0.023°).
- Beam diameter: 3 mm to 4 mm.

The beam diameter safely surpassing that of the measured POFs (1 mm) guarantees almost uniform illumination of fibre input face. The stability of the output power was tested together with the stability of the CCD camera's response after exposure time change, for the results see *Fig. 5.9*.

5.3 CCD camera calibration

On one hand scientific CCD cameras are fast and robust instruments for optical measurements. On the other hand, most of reasonably priced scientific CCD cameras are constructed to give rather qualitative than quantitative results. Nevertheless, they can be used for scientific purposes and POF measurements, although with a calibrating procedure. In this part we describe the measurement setup used to obtain calibration measurements (Part 5.3.1), discuss common inaccuracies of CCD cameras (Part 5.3.2), propose a calibration procedure for measurements (Part 5.3.3) and address the often-occurring problem of too small dynamic range (Part 5.3.4).

5.3.1 Setup for calibration measurements

The general idea of the setup is to get several snaps (raw responses of the camera's CCD sensor) under direct uniform illumination of the sensor with the wavelength approximately the same as that of the used laser. *Fig. 5.2* shows the setup.

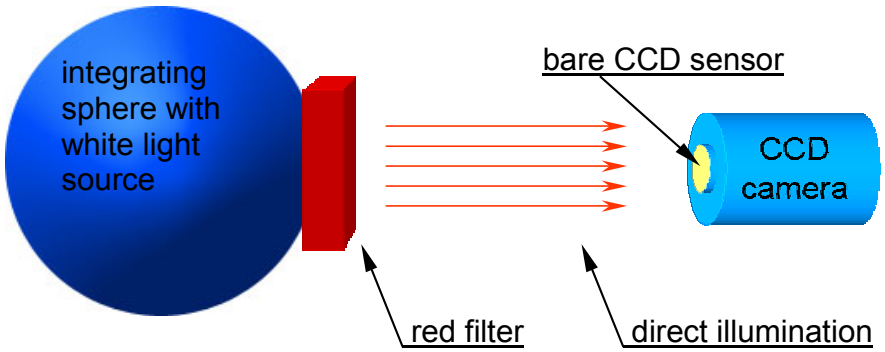

Fig. 5.2 *Principle of the calibration setup.*

The distance between the integrating sphere and the bare CCD sensor was approx. 0.5 m. The uniformity of the sensor relative illumination intensity was better than 0.5 %, measured with a linear photodiode. An example is shown in *Fig. 5.3*. The sensor of dimensions 14.34 mm × 14.34 mm was positioned for measurements with its centre at the '0 mm point' of the horizontal axis on *Fig. 5.3*. As the CCD camera a '*BFi OPTiLAS Eurocam CCD-1020*' with the following characteristics was used:

- 1024 × 1024 pixel resolution,
- Bit depth of 12 bpp (bit per pixel), i.e. 4096 distinct grey levels [GL],
- Adjustable exposure time ≥ 1 ms.

The same camera was used for all further FFP measurements (Chapter 6).

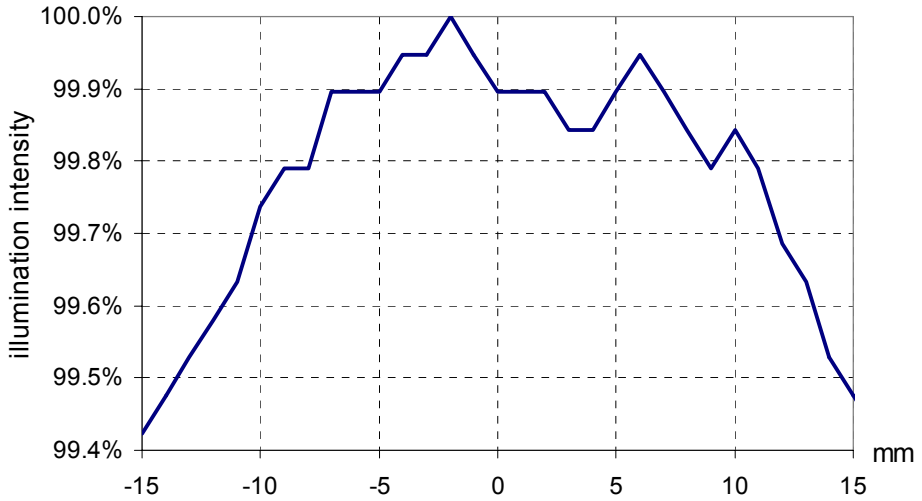

Fig. 5.3 *Typical measurement of the illumination uniformity of the CCD sensor (measured radial from the centre and plotted as normalised intensity).*

For each of the considered exposure times (1 ms, 2 ms, 4 ms, 8 ms, 16 ms and 32 ms) the following four measurement series were made, each one of 16 measurements, to obtain the calibration data:

- A series X_0 of 16 measurements taken with zero illumination, i.e. under completely dark conditions. The absolute illumination intensity $m_0 = 0$.
- Three series $X_i,\ i \in \{1, 2, 3\}$ of 16 measurements, each taken under uniform lighting conditions generated by the distant integrating sphere of *Fig. 5.2* and (by using different voltage) generating approx. 25 %, 50 % and 75 % of the maximal CCD sensor response (10^{12} GL = 4096 GL, grey levels). The absolute (actual) illumination intensity $m_i,\ i \in \{1, 2, 3\}$ was measured for each series separately with a linear photodiode.

5.3.2 Unreliability factors and calibration data

The reliability of a single uncalibrated CCD camera measurement may be strongly influenced by several factors; below the most important are mentioned.

5.3.2.1 Dark profile

The dark profile is the camera's output under zero illumination, thus it is the constant bias of all measurements taken with the camera. For each exposure time it is computed as the average of all 16 measurements of the X_0 series taken under completely dark conditions. As the dark profile is strongly temperature-dependent and the used camera is not cooled, all measurements should be taken after the temperature of the CCD sensor stabilises. *Fig. 5.4* shows the dark profile of the used camera at the typical 32 ms exposure time. Besides the slope, a finer wave-like pattern may be noticed, it is probably related to the row arrangement of the CCD cells within the sensor.

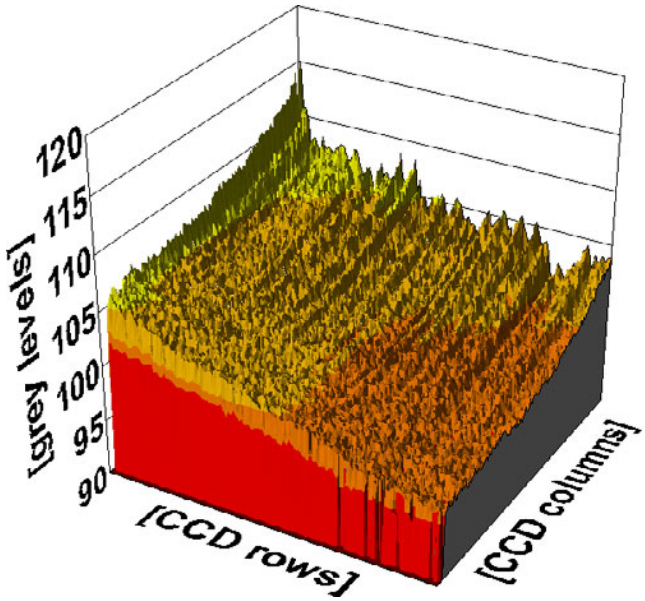

Fig. 5.4 *The camera's dark profile at 32 ms exposure time. For presentation clarity and to reduce the effect of unreliable cells and noise the figure shows averages over 8×8 squares.*

5.3.2.2 Random noise

Sensor random noise is the cause of inevitable differences between successive measurements taken under exactly the same conditions. Random noise of a single CCD cell may be modelled with a centred Gaussian random distribution. For each of six exposure times and for each CCD cell the sample standard deviation s_i, $i \in \{0, 1, 2, 3\}$ of each of four measurement series was computed.

The average sample standard deviation of the dark profile (under null illumination) at the most-used 32 ms exposure time was found to be approx. 1.5 GL (grey levels). For the non-zero illumination, it turned out that s_i increases with the illumination intensity. Thus, the random noise of each cell was characterised by taking the maximum value of three relative sample standard deviations[10]. The average value at 32 ms exposure time was found to be approx. 0.6 %, which corresponds to approx. 24 GL at the full illumination (4095 GL).

[10] Sample standard deviation divided by the respective average illumination level.

5.3.2.3 Non-linear response function

Response function of an ideal CCD cell should have a linear relationship between input and output. However, response function of a real CCD cell may not be ideally linear, as it was the case with the earlier investigated '*DALSA CA-D4*' camera [14] with the average relative non-linearity of 7 %. Nevertheless, the camera used here showed the average non-linearity of approx. 0.3 % only (at 32 ms exposure time).

For each exposure time the response function of each cell is modelled in the following way: The average response x_i of each cell in the measurement series X_i and the corresponding measured absolute lighting intensities m_i form a series of four points (m_i,x_i), $i \in \{0, 1, 2, 3\}$ lying on the actual response function of the cell. The points have to be fitted with a cell-specific function $x = f(m)$ (linear, quadratic, exponential, etc.). The inverse function $m = f^{-1}(x)$ will be further used to translate cell's response x to the real illumination intensity m and where appropriate to correct cell's nonlinear characteristics, too. The average non-linearity of the sensor can be computed by averaging relative deviations of the best linear fit from the measured points.

As the camera used here had almost linear characteristic, the response functions of its CCD cells were fitted with the linear function:

(5.1) $$x = f(m) := x_0 + am.$$

5.3.2.4 Non-uniform sensitivity

Differences between response functions of CCD cells make the sensitivity profile of a CCD sensor non-uniform. As the CCD camera used here had almost linear response, its sensitivity profile can be assumed to stay constant over all illumination levels and be directly defined by the inclinations *a* of individual cells' response functions Eq. (5.1). *Fig. 5.5* shows the relative sensitivity profiles of the used camera at 1 ms and 32 ms exposure time (the average value was rescaled to 100 %).

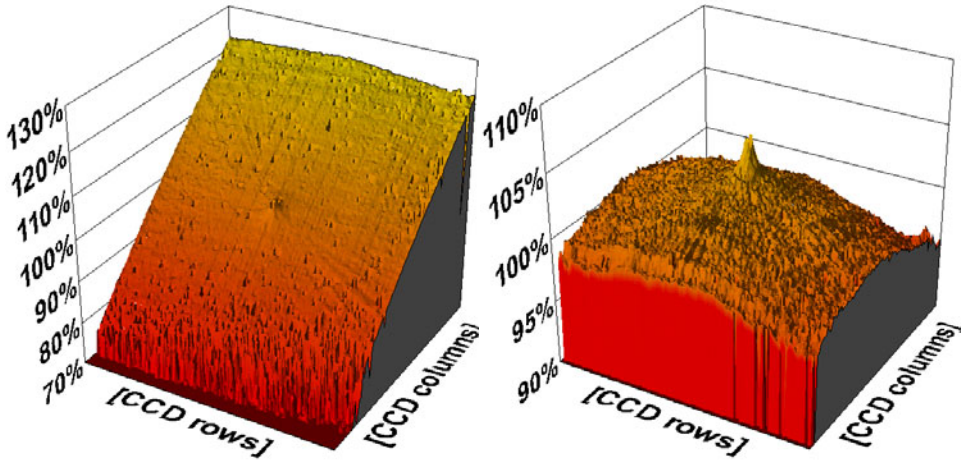

Fig. 5.5 *Relative sensitivity profiles of the camera at 1 ms (left) and 32 ms (right) exposure time. For presentation clarity and to reduce the influence of unreliable cells and noise the figures show averages over 8×8 squares.*

5.3.2.5 Damaged CCD cells

In a real CCD sensor some cells are usually damaged or dead as well as there may be dust and scratches present on the CCD sensor's surface generating a remarkable local sensitivity change. Such cells will be called irregular. Measurements of such cells are unreliable and should be approximated basing on measurements of neighbouring cells. *Fig. 5.6* presents sample defect of the sensor surface of the investigated CCD camera that has been identified via the sensitivity profile analysis.

As an irregularity criterion the following can be used: The cell is marked irregular if and only if it satisfies at least one of the following conditions:

- The random noise of the cell is too high (e.g. more than a given r-percentile of the noise values of all investigated cells).
- The fit quality (average square fit error) of cell's fitted response function f is too bad (e.g. the error exceeds a given r-percentile of the square fit errors of all investigated cells).
- The fitted response function f of the cell differs too much from the average fitted response function (e.g. the mean square difference exceeds a given r-percentile of the mean square differences of all investigated cells).

For further investigations the 3σ level (i.e. $r \approx 99.7$ %) was used. The total number of irregular cells of the camera was found to be about 2.4 % (approx. 25 000 of the total cell number ~1 050 000). *Fig. 5.7* shows the distribution of the irregular cells on the sensor surface at 32 ms exposure time. Note the horizontal blue strip in the upper part of the figure, consisting entirely of unusable irregular cells.

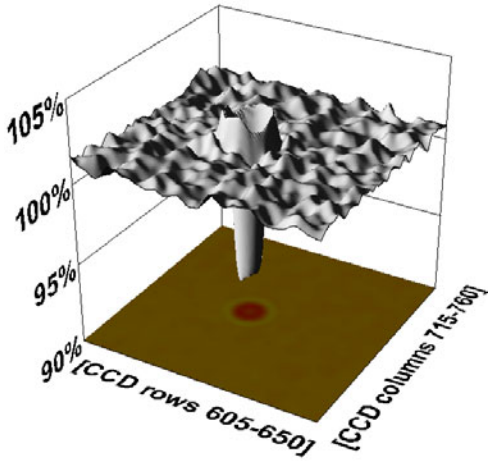

Fig. 5.6 *Fragment of the sensitivity profile of the camera at 32 ms exposure time. The magnification clearly shows a defect of the CCD sensor surface.*

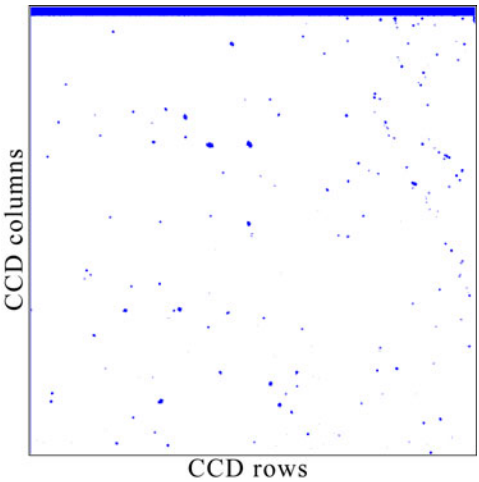

Fig. 5.7 *Irregular cells (blue dots) foundt 32 ms exposure time*

5.3.2.6 Temperature dependence

Many characteristics of a CCD camera are strongly temperature-dependent. As the CCD camera used here was not cooled, all measurements (calibration as well as FFP measurements) had to be taken after the CCD sensor temperature stabilises. *Fig. 5.8* shows the camera's response in dependence on the heat-up time (the camera was switched on at the time 0, after overnight cooling down to the room temperature). As a result, the heat-up time of at least 2 hours before all measurements was always used.

The temperature distribution on the sensor could be different for different exposure times, which (if true) would require some accommodation time after any change of the exposure time. *Fig. 5.9* shows the response of the already heated-up camera after the exposure time change at the time 0 from 32 ms to 1 ms. As the variations found are rather minute, it was assumed that there is no need for such accommodation time. Small variations of the camera's response prove also good output power stability of the laser used for the measurements.

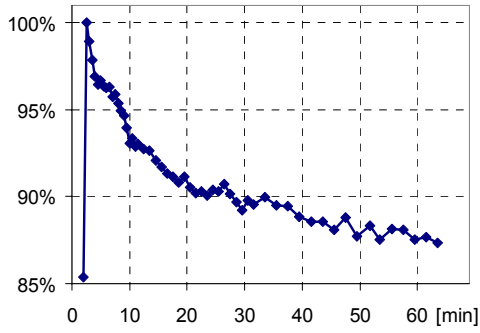

Fig. 5.8 *The camera's typical response (an average over 10×10 cells square) in dependence on the heat-up time at the exposure time of 32 ms.*

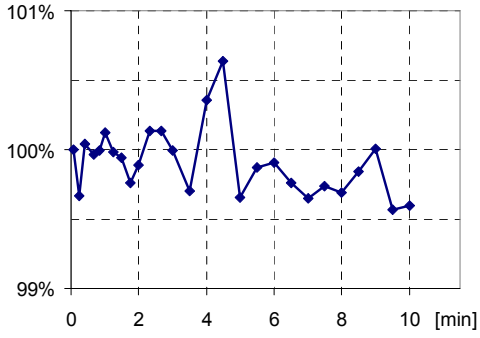

Fig. 5.9 *Response of the already heated-up camera after a change of the exposure time from 32 ms to 1 ms.*

5.3.3 Calibration procedure for measurements

The factors mentioned in the previous section strongly influence the reliability of measurements taken with a CCD camera. Nevertheless, using the calibration data collected and processed as described in Part 5.3.1 and Part 5.3.2, each raw measurement can be calibrated in the following way to exclude or minimise effects of the most of the mentioned unreliability factors:

1) Let the camera heat-up at least 2 hours after switching it on.

2) Take a series of N subsequent raw measurements and compute their average. The random noise should be reduced by the factor of $N^{½}$.

3) Correct the sensor's dark noise and non-uniform sensitivity by applying to the measurement of each CCD cell its inverse fitted response function $m = f^{-1}(x)$.

4) For each irregular cell approximate its measurement value using the calibrated measurement values of its neighbouring regular cells.

As the unreliability characteristics of the camera can be wavelength-dependent, the calibration measurements should be made with a light source of approximately the same spectrum as used for final measurements.

5.3.4 Expanding the dynamic range

Another practical problem concerning the most of the low-end scientific cameras is their restriction to the bit depth of 8 bpp or 12 bpp only and thus to the dynamic range of 1:256 or 1:4096 at the very best. This dynamic range, relatively small for many applications, can be further considerably reduced by the above-mentioned unreliability factors. It was found that this limitation might be overcome by combining several calibrated measurements taken with different exposure times, according to the following procedure:

1) Make several calibrated measurements using different exposure times.
2) Upscale those made at shorter exposure times to match the longest exposure time measurement. As the exposure time rate only roughly determine the scaling factor, find it beforehand by comparing the response functions fitted at different exposure times.
3) Merge the scaled measurements into the final measurement.

Note that for each of the calibrated measurements obtained in 1) a separate calibration procedure should be performed and a separate set of calibration data (Part 5.3.1) should be used. Note also that at long exposure times in highly excited areas overexposure (blooming effect) should be avoided.

5.4 Quality verification of the far-field optics

As the far-field optics in the setup outlined on *Fig. 5.1* a specialised FFP optics A3267-12 from HAMAMATSU with the following optical specifications was used:

- Detectable angular range: ±45°.
- Angular resolution: 0.2°.
- Wavelength range: 630 nm – 1650 nm.

Accuracy of measurements taken with the setup strongly depends on the optics' reliability. Thus, three crucial FFP optics' characteristics have been investigated:

- Linearity of the θ-f (*angle*→*space*) transformation.
- Distortion level of the θ-f transformation.
- Real angular resolution and its stability across the angular input range.

The results of the tests described below showed that the real angular resolution of 0.5° (with the used CCD camera) is worse than the nominal value of 0.2°. Nevertheless, the tests clearly confirm high quality of the optics and show that there is no need for any FFP optics calibration procedure.

5.4.1 Test setup and measurements

For test purposes the red laser diode described in Part 5.2 was used to directly illuminate (with adjustable illumination angle) the input lens of the FFP optics under various angles with the help of a goniometer. The full field of the FFP optics (approx. 90° in diameter) was tested in approx. 5° steps with the resolution of ±5′ (≈ ±0.083°), all input beams were contained in one plane which included also the optics' axis. The resulting spots were registered with the CCD camera and calibrated according to the procedure described in Part 5.3.3. *Fig. 5.10* shows a typical example of a calibrated spot.

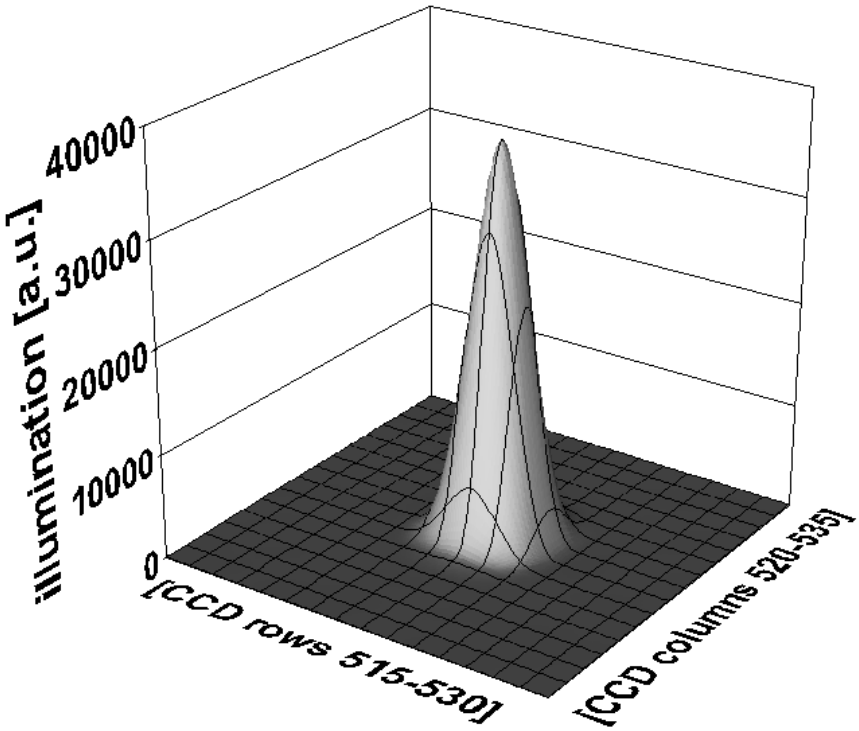

Fig. 5.10 *Sample calibrated spot measured by the CCD camera (clip from the complete CCD array). One CCD cell row/column corresponds to the angular distance of approx. 0.2°.*

5.4.2 Linearity of angle to space transformation

As the angular differences between all successive input beams were equal to 5°, the distance between respective peaks (the maxima) of successive measured spots on the CCD sensor should be identical, up to one pixel. Because the plane in which the illumination angle changes is parallel neither to the rows nor to the columns, both are influenced by the angular changes. *Table 5.1* lists the coordinates of all spot peaks, i.e. of the CCD cells with maximum illumination, and the distance between the current and the previous spot.

Table 5.1 *Coordinates of the spot peaks on the CCD sensor.*

illumination angle	x (rows)	y (columns)	d	illumination angle	x (rows)	y (columns)	d
-45°	*410*	*717*	-	5°	*536*	*507*	*24.7*
-40°	*423*	*696*	*24.7*	10°	*548*	*486*	*24.2*
-35°	*436*	*675*	*24.7*	15°	*561*	*465*	*24.7*
-30°	*448*	*654*	*24.2*	20°	*573*	*444*	*24.2*
-25°	*460*	*633*	*24.2*	25°	*585*	*423*	*24.2*
-20°	*473*	*612*	*24.7*	30°	*598*	*402*	*24.7*
-15°	*485*	*591*	*24.2*	35°	*610*	*381*	*24.2*
-10°	*498*	*570*	*24.7*	40°	*623*	*360*	*24.7*
-5°	*510*	*549*	*24.2*	45°	*635*	*339*	*24.2*
0°	*523*	*528*	*24.7*				

The linearity of the FFP optics has turned out to be constant across the full detectable angular range of 90° (up to one pixel). One row or column of CCD cells corresponds to the illumination angular difference of approx. 0.2°. The results confirm that there is no need for any linearity corrections.

5.4.3 Distortion of angle to space transformation

As all input beams were contained in one plane, the peaks (i.e. the maxima) of all measured spots should be also placed in one line across the CCD sensor, up to one-pixel resolution. Using the coordinates of the spots maxima from *Table 5.1* the linear best fit can be computed to be $y = -1.68066x + 1406.81074$. The average non-linearity of the spots, i.e. the square average distance between the spots and the linear best fit was found to equal approx. 0.06°, i.e. much less then 0.2° corresponding to one cell distance. Thus, there is no need for any distortion corrections.

5.4.4 Angular resolution

Fig. 5.8 shows how much an illuminating beam of approx. 0.02° divergence (see Part 5.2) is broadened by the FFP optics. Although the maximum of its energy distribution can be located within the distance of one cell (as in Part 5.4.2), the nearest distance in which two similar distributions can be distinguished from each other depends on the dispersion of the distribution. It is common sense to use the width at half height as a measure, i.e. the diameter in degrees of each spot at 50 % of its height, see *Fig. 5.11*. Additionally the corresponding 25 % values are given to be on the save side. The resolution measured at half height (50 % level) was not worse than 0.5°, which will be assumed to be the real angular resolution of the setup.

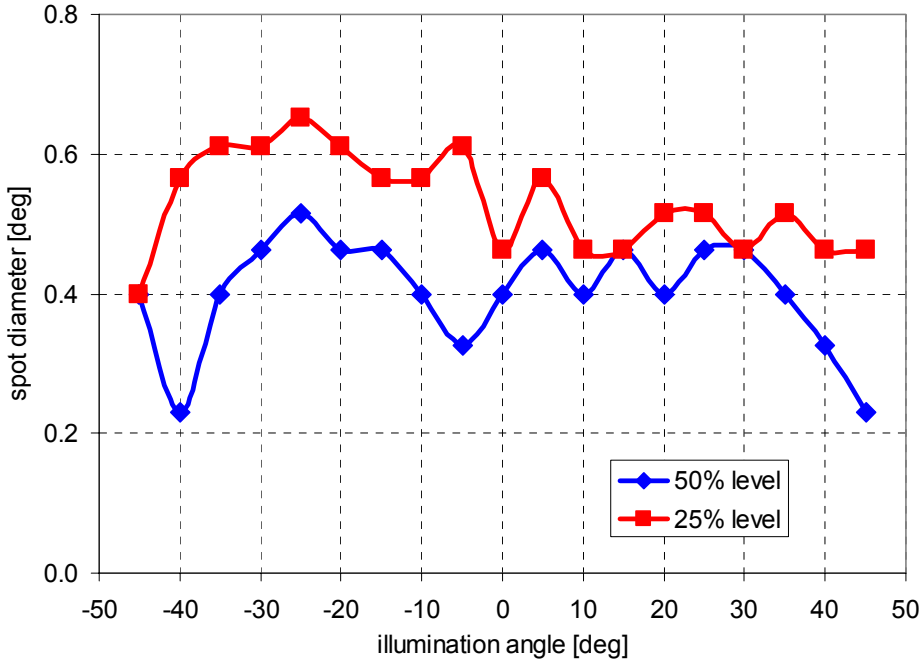

Fig. 5.11 *FFP optics resolution test: spot diameter at 25 % and 50 % spot height.*

6 Far-field profile measurements

6.1 Samples preparation

As stated in Part 4.4.1, the non-aged and aged up to 4467 hours (approx. half a year) samples (at 100 °C / <<50 % RH) have been used for further investigations. *Table 4.3* lists the aging times of the six sets of the fibre samples used, each consisting of three fibres from three manufacturers and finally cut into three pieces of approx. 0.8 m, 3.2 m and 10 m length. Then, after fine polishing of the endfaces, 54 fibre samples were prepared for FFP measurements.

6.2 Measurement procedure

The measuring setup is outlined in *Fig. 5.1* and used with three illumination angles (6°, 15° and 24°) to investigate the angle-dependent optical properties of the fibre. The fibre bend radius during all the measurements was kept not less than 20 cm to avoid the influence of bending [20, 68, 69].

Thus, each measured fibre sample is identified by three parameters:

- manufacturer (*M*: Mitsubishi Rayon, *A*: Asahi Chemicals, *T*: Toray Industries),
- aging by set no. (*set0*, …, *set5*: see *Table 4.3*)
- sample length (*1*: ~0.8 m, *2*: ~3.2 m, *3*: ~10 m),

while each FFP measurement can be uniquely identified by the additional fourth parameter:

- illumination angle (6°, 15° and 24°).

Thus, for clarity from now on each fibre sample will be uniquely identified by the first three parameters (e.g. *M-set3-2* will mean: Mitsubishi's fibre, aged 667 h, 3.2 m sample length), while each measured FFP will be identified by all four parameters (e.g. *M-set3-2-15* will mean the FFP of the *M-set3-2* fibre sample measured at 15° illumination angle).

For each calibrated FFP measurement six raw snaps with up to six applicable exposure times were used, meaning a maximum of 36 snaps for each of 3 illumination angles and 54 fibre samples. These raw snaps were calibrated, related to the corresponding exposure times and merged together according to the procedure described in Parts 5.3.3 and Part 5.3.4. In total more than 1000 raw snaps had to be processed.

Taking into account the three illumination angles, 54 fibre pieces need a total number of 162 measured FFPs. However, for the shortest fibres (0.8 m) many measurements had to be discarded, as they were apparently strongly dependent on the momentary run of the fibre, as observed on the monitor of the online measurement system. Due to an accidental damage to the sample, one measurement of the 3.2 m fibre piece (*M-set1-2-24*) had to be discarded, too. *Table 6.1* lists the illumination angles used for the measurements of the 18 shortest fibre pieces.

Table 6.1 *Illumination angles used for the FFP measurements with the shortest (0.8 m) fibre pieces. All three illumination angles have been used with all 36 longer fibre pieces (except M-set1-2-24).*

	ESKA CK-40	LUMINOUS TB-1000	PGU-FB 1000
set0	*24°*	-	*24°*
set1	*24°*	*15°, 24°*	-
set2	*24°*	*15°, 24°*	*24°*
set3	*15°, 24°*	*24°*	*15°, 24°*
set4	*24°*	-	*15°, 24°*
set5	*24°*	*15°, 24°*	*15°*

6.3 FFP extraction

The calibrated measurements, obtained as described in the previous part, have the form of two-dimensional functions (or 1024×1024 matrices) characterising the two-dimensional angular power distribution of the light leaving the fibre endface. The distance from the matrix centre depends linearly (Part 5.4.2) on the axial angle α of an outgoing ray, while its azimuthal angle φ equals the azimuth of the corresponding point on the matrix[11]. A clip of the *M-set3-2-24* two-dimensional FFP has been linearly downscaled to the 256-level grey scale (the brightest point has grey level 255) and inverted shown on *Fig. 6.1*.

The discrete one-dimensional $FFP(\alpha,\alpha+\Delta\alpha)$ will be computed out of the two-dimensional measurement matrix M using the formula Eq. (2.105) with the discretisation step $\Delta\alpha \approx 0.2°$. The total power $S(\alpha,\alpha+\Delta\alpha)$ radiated into the axial angle interval $[\alpha,\alpha+\Delta\alpha)$ can be computed by taking:

$$S(\alpha,\alpha+\Delta\alpha)=\int_0^{2\pi}\int_{\alpha}^{\alpha+\Delta\alpha}\varphi\cdot M\left(x_0+d_\alpha^{-1}\theta\cos\varphi,\, y_0+d_\alpha^{-1}\theta\sin\varphi\right)d\theta\, d\varphi\,, \tag{6.1}$$

where (x_0, y_0) are the coordinates of the FFP ring centre, $d_\alpha \approx 0.2°$ is the angular difference corresponding to one-pixel distance on the matrix (see Part 5.4.2). The value of the measurement matrix $M(x,y)$ for real x and y is computed by linear interpolation of the neighbouring integer points:

$$\begin{aligned} M(x,y) = {} & (\lceil x\rceil - x)((\lceil y\rceil - y)M(\lfloor x\rfloor,\lfloor y\rfloor)+(y-\lfloor y\rfloor)M(\lfloor x\rfloor,\lceil y\rceil)) \\ & +(x-\lfloor x\rfloor)((\lceil y\rceil - y)M(\lceil x\rceil,\lfloor y\rfloor)+(y-\lfloor y\rfloor)M(\lceil x\rceil,\lceil y\rceil))\,. \end{aligned} \tag{6.2}$$

The resulting discrete one-dimensional FFP has to be rescaled by dividing it by the cosine of the respective illumination angle (6°, 15° or 24°) to account for the decrease in the power entering the fibre.

[11] For angle notational conventions see *Fig. 2.1* and *Fig. 2.3*.

Note that the total transmitted power can be computed using Eq. (6.1) as $S\left(0^{o},45^{o}\right)$, due to the fact that the FFP optics' detectable angular range of ±45° (Part 5.4) exceeds the acceptance angle α_{max} of all measured fibres (approx. 30°, *Table 4.2*).

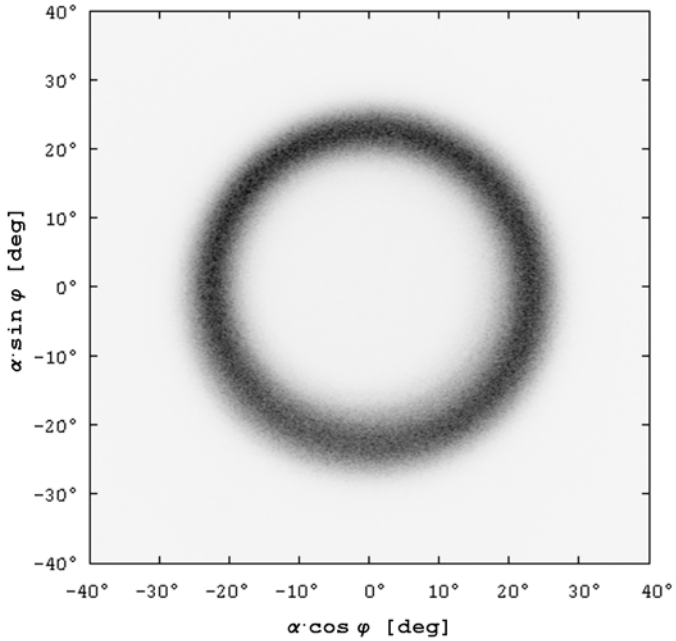

Fig. 6.1 *Sample calibrated two-dimensional FFP measurement* M-set3-2-24 *(i.e. ESKA CK-40 fibre, aged 677 hours at 100 °C / <<50 % RH, 3.2 m length, illumination angle 24°).*

6.4 Sample results

6.4.1 Non-aged 10 m fibre

Fig. 6.2 to *Fig. 6.4* show the influence of the illumination angle on the FFPs of 10 m non-aged samples of fibre from all three manufacturers.

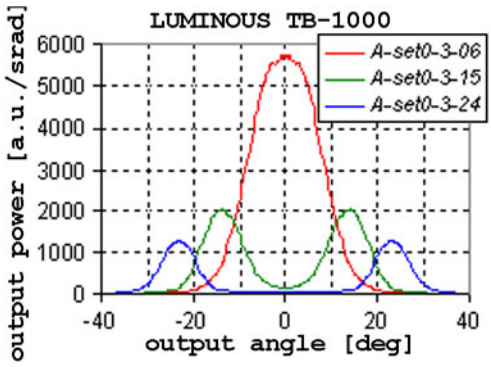

Fig. 6.2 *Influence of the illumination angle (6°, 15°, 24°) on the FFP of 10 m non-aged Asahi's fibre.*

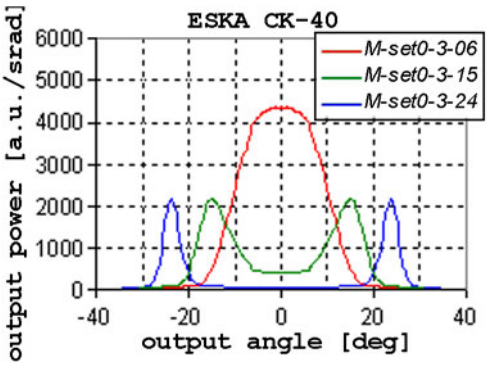

Fig. 6.3 *Influence of the illumination angle (6°, 15°, 24°) on the FFP of 10 m non-aged Mitsubishi's fibre.*

Fig. 6.5 shows the transmission loss due to the change of the illumination angle. Besides the generally higher attenuation of the Mitsubishi's fibre, a decreasing relation between the total transmission and the illumination angle can be observed. It is in perfect agreement with the raytracing model, as the rays travelling through fibre with higher propagating angle: 1) cover longer path and 2) undergo more reflections on the core-clad interface than the rays parallel to the fibre's axis. The pronounced transmission drop of the Toray's fibre at the 24° illumination angle, in relation to other fibres, suggests higher ray reflection losses on the core-clad interface, see *Table 7.1* to *Table 7.3*.

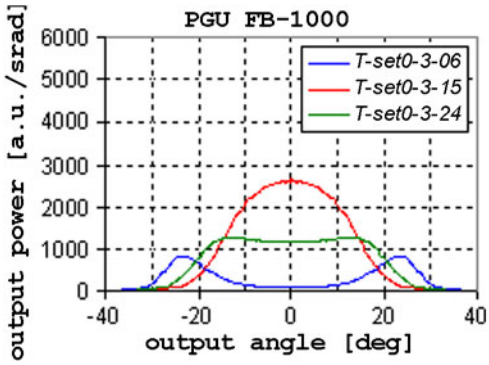

Fig. 6.4 *Influence of the illumination angle (6°, 15°, 24°) on the FFP of 10 m non-aged Toray's fibre.*

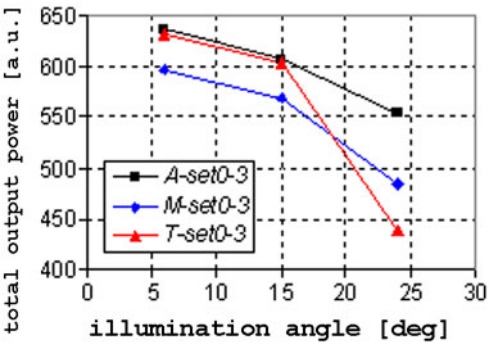

Fig. 6.5 *Influence of the illumination angle (6°, 15°, 24°) on the total output power of 10 m non-aged fibres.*

Fig. 6.6 to *Fig. 6.8* compare the FFPs of 10 m samples of the fibre from different manufacturers. The shapes of the curves clearly suggest that the most scattering occurs in the Toray's fibre (red curve is on all figures wider than the other two). The relative scattering intensity in both other fibre types turns out to be dependent on the illumination angle:

- for lower order modes (6° illumination angle, *Fig. 6.6*) higher in the Mitsubishi's fibre (blue curve),
- for 15° illumination angle (*Fig. 6.7*) approximately the same in both fibres (blue and black curves overlap)
- for higher order modes (24° illumination angle, *Fig. 6.8*) higher in the Asahi's fibre (black curve).

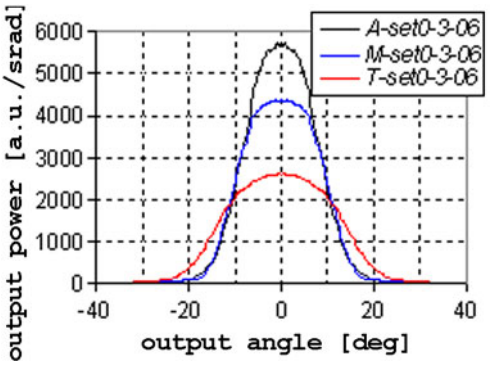

Fig. 6.6 *The FFPs of 10 m non-aged fibres from three manufacturers illuminated under 6° angle.*

The above observations are confirmed by the fitted values of angle-dependent scattering intensity, see Part 7.5, *Fig. 7.10*.

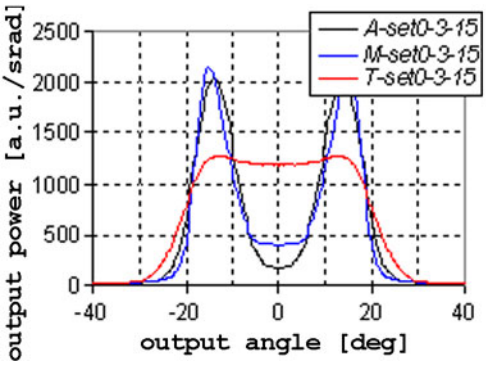

Fig. 6.7 *The FFPs of 10 m non-aged fibres from three manufacturers illuminated under 15° angle.*

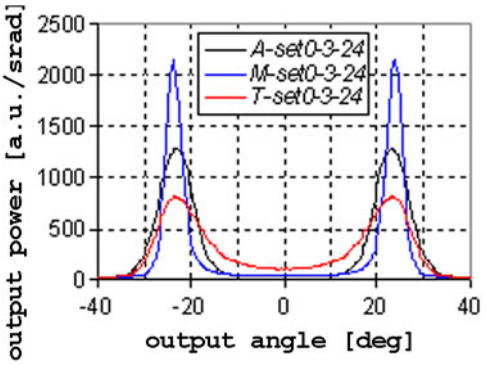

Fig. 6.8 *The FFPs of 10 m non-aged fibres from three manufacturers illuminated under 24° angle.*

6.4.2 Influence of sample length

Fig. 6.9 and *Fig. 6.10* illustrate the influence of the POF sample length on its FFP for the illumination angles 15° and 24°:

- The attenuation is in general proportional to fibre length, thus the FFPs of the longer samples (green and blue curves) runs mainly below the FFPs of the shorter samples (red curve).
- The scattering is also proportional to fibre length, thus the FFPs of the longer samples are more diffused.

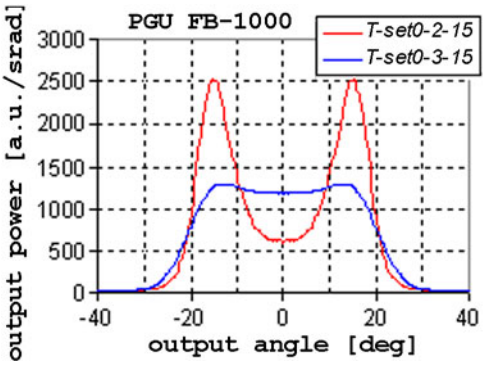

Fig. 6.9 *Influence of POF sample length (3.2 m and 10 m) on the FFP of non-aged Toray's fibre at 15° illumination angle.*

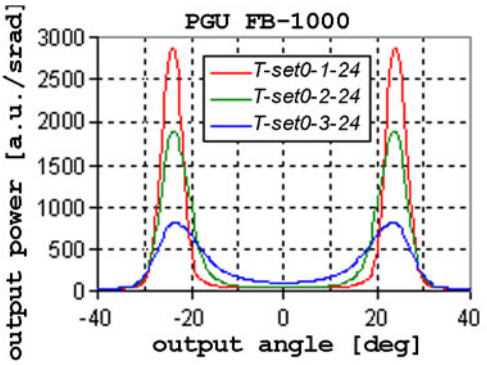

Fig. 6.10 *Influence of POF sample length (0.8 m, 3.2 m and 10 m) on the FFP of non-aged Toray's fibre at 24° illumination angle.*

6.4.3 Influence of aging time

6.4.3.1 Attenuation

Fig. 6.11 to *Fig. 6.13* show the total transmitted power (i.e. $S\left(0^{o},45^{o}\right)$ of Eq. (6.1)) through a 3.2 m sample in dependence on the aging time. The logarithmic scale for the (horizontal) time axis has been used to clearly show the transmission change between *set0* (0 h), *set1*

(2 h) and *set2* (258 h). Note that the logarithmic scale could be used only after adding 1 h to all aging times listed in *Table 4.3* (to move the beginning of the aging from time 0 h to 1 h).

The total transmitted power of *Fig. 6.11* to *Fig. 6.13*, measured in arbitrary but absolute units, can be easily recalculated to obtain the relative transmission loss of the sample in dependence on the aging time (i.e. relative to the transmission of the non-aged sample at the respective illumination angle). *Fig. 6.14* to *Fig. 6.16* compare it with the relative transmission loss calculated from the attenuation measured with a spectrometer (black lines, calculated from the attenuation data *Fig. 4.7* to *Fig. 4.8*). The curves corresponding to the spectrometer measurements combine mainly the behaviour of the curves corresponding to the 15° and 24° illumination angle. This is caused by the high NA of the large-diameter silica fibre directly illuminating the fibre input face in the spectrometer setup, thus strongly exciting higher-order modes.

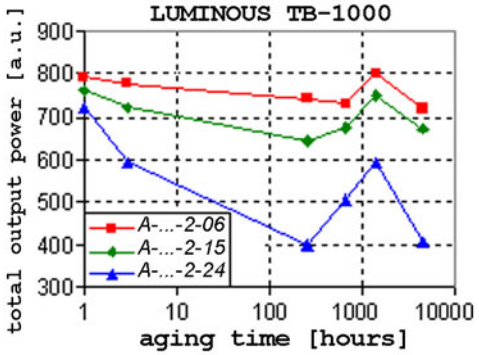

Fig. 6.11 *Aging time influence on the total output power of 3.2 m cold Asahi's fibre at three illumination angles (6°, 15° and 24°).*

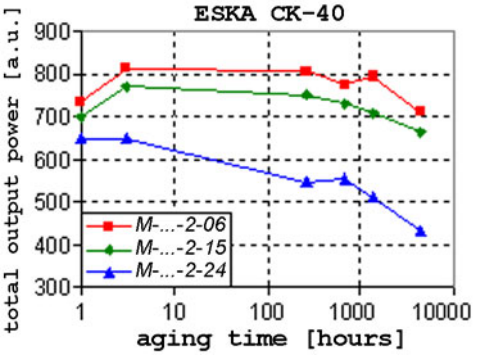

Fig. 6.12 *Aging time influence on the total output power of 3.2 m cold Mitsubishi's fibre at three illumination angles (6°, 15° and 24°).*

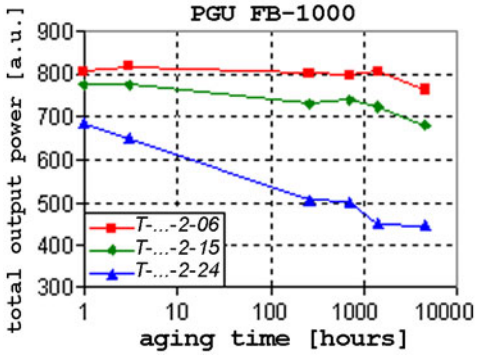

Fig. 6.13 *Aging time influence on the total output power of 3.2 m cold Toray's fibre at three illumination angles (6°, 15°, 24°).*

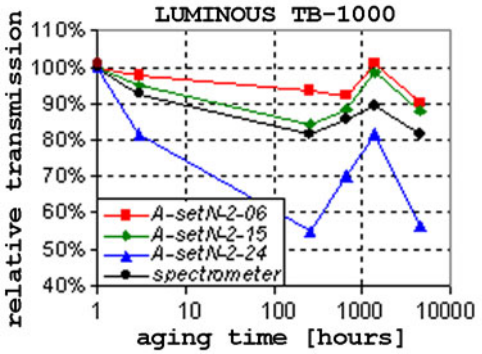

Fig. 6.14 *Relative transmission of 3.2 m cold Asahi's fibre computed from the FFPs and measured with a spectrometer.*

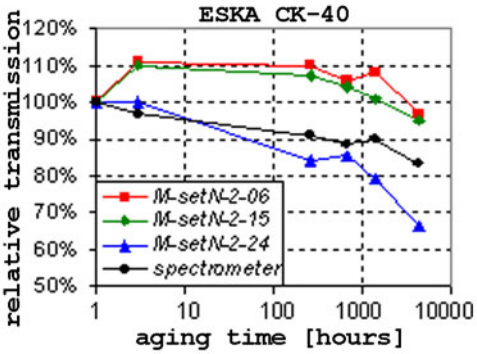

Fig. 6.15 *Relative transmission of 3.2 m cold Mitsubishi's fibre computed from the FFPs and measured with a spectrometer.*

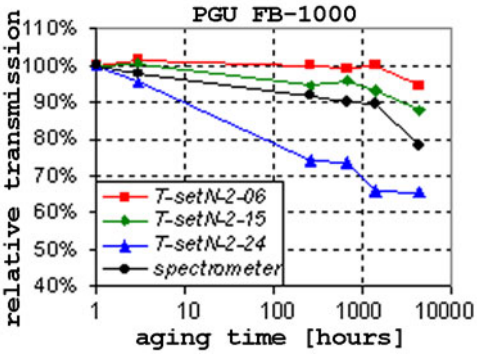

Fig. 6.16 *Relative transmission of 3.2 m cold Toray's fibre computed from the FFPs and measured with a spectrometer.*

6.4.3.2 Far-field profile

Fig. 6.17 - *6.22* show the FFPs of the 3.2 m samples in dependence on the aging time..

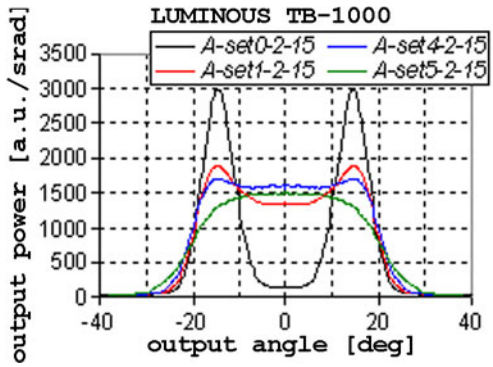

Fig. 6.17 *Influence of POF aging time on the FFP of 3.2 m Asahi's fibre at 15° illumination angle.*

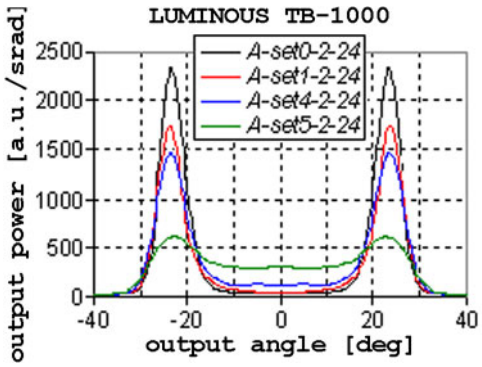

Fig. 6.18 *Influence of POF aging time on the FFP of 3.2 m Asahi's fibre at 24° illumination angle*

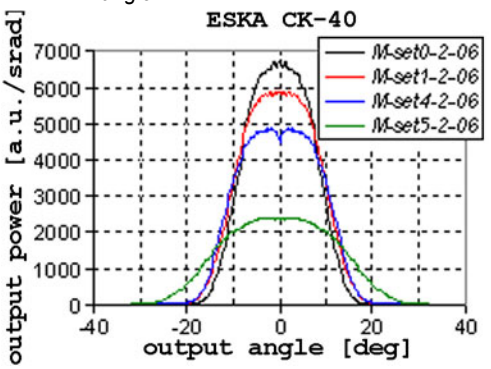

Fig. 6.19 *Influence of POF aging time on the FFP of 3.2 m Mitsubishi's fibre at 6° illumination angle.*

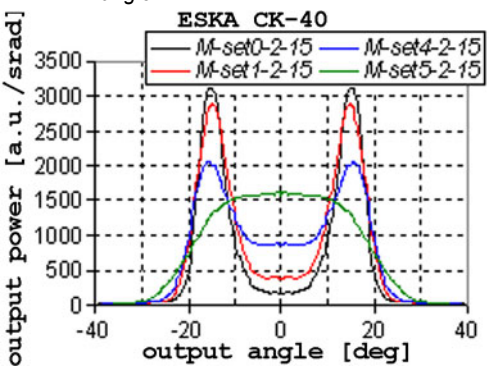

Fig. 6.20 *Influence of POF aging time on the FFP of 3.2 m Mitsubishi's fibre at 15° illumination angle*

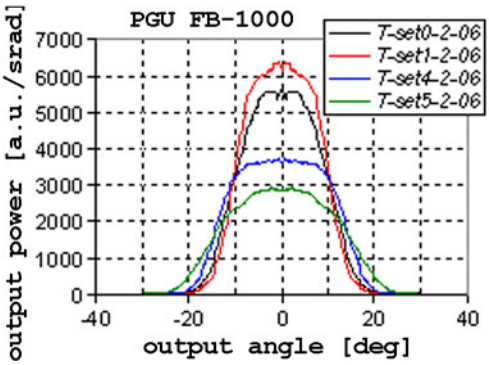

Fig. 6.21 *Influence of POF aging time on the FFP of 3.2 m Toray's fibre at 6° illumination angle.*

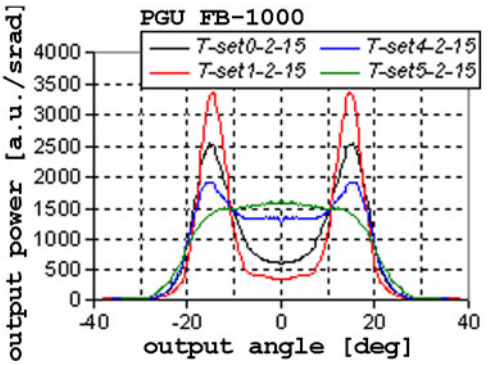

Fig. 6.22 *Influence of POF aging time on the FFP of 3.2 m Toray's fibre at 15° illumination angle.*

A general increase in attenuation (each successive curve runs generally below the preceding one) and in scattering intensity (successive curves are more diffused) with aging time can be observed. The inverse run of the first two curves of the Toray's fibre (*Fig. 6.21* and *Fig. 6.22*) can be attributed to the measured slight increase in the transmission of lower-order modes after the first 2 hours of aging, see *Fig. 6.13* and *Fig. 6.16*. It suggests a slight decrease in scattering intensity, too

7 Aging influence on model parameters

The first part of this chapter (Part 7.1) discuss the optimised values of the raytracing parameters, sample lengths of their uncertainty intervals, and shows graphs of the dependence of the optimised target function[12] on two sample parameters. Part 7.2 compares the overall attenuation of the simulated fibres with the measured attenuation of the real fibres. Part 7.3, Part 7.4 and Part 7.5 discuss the influence of the aging process on the optimised model parameters except for the endface scattering (the quality of the core-clad interface, attenuation of the bulk core material, angle-dependent scattering). It was found that the measured profound transmission drop during the first hours and days of aging is caused mainly by physical deterioration of the core-clad interface while the slower drop at the end of the aging process (first after few thousands of hours) can be attributed to the beginning then chemical deterioration of the fibre material.

7.1 Raytracing parameters

The optimum values of six raytracing parameters were found separately for all of the 18 investigated POF types (3 fibre manufacturers, 6 aging times each), using the optimisation procedure described in Part 3.2.3. As stated in Part 6.2, a total of as many as 128 simulated and measured FFPs had to be matched. An average of 1500 rays were used to compute each FFP; finding the best fit along a given direction required approx. 12 computations of the target function Eq. (3.1). To find the global minimum the optimisation along all the directions had to be repeated at least 4 times. As a result approx. 10 million rays had to be traced.

Table 7.1 to *Table 7.3* list for all three manufacturers the optimum values of the respective fibres' raytracing parameters found during the optimisation process. The numeration of the parameters was introduced and explained in Part 3.2.3.2, *Table 3.3*. Fibre 'sets' represent aging times (*set0* = non-aged; *set5* = strongly aged), for the explanation see *Table 4.3* in Part 4.4.1 and Part 6.2. Appendix A3 compares sample graphs of FFPs measured and simulated using the corresponding optimum parameter values from *Table 7.1* to *Table 7.3*.

Table 7.1 *Optimum values of the raytracing parameters of the non-aged and aged Mitsubishi's fibre (ESKA CK-40). See Table 4.2 for the aging times and Table 3.3 for the parameter description.*

	M-set0	*M-set1*	*M-set2*	*M-set3*	*M-set4*	*M-set5*
var1 [deg]	*3.4*	*3.0*	*3.2*	*3.2*	*3.5*	*3.8*
var2 [dB/km]	*113*	*113*	*120*	*120*	*125*	*145*
var3 [mdB]	*0.10*	*0.25*	*1.20*	*1.15*	*1.20*	*1.55*
var4 [mm]	*34.0*	*13.5*	*8.0*	*9.75*	*10.0*	*5.80*
var5 [a.u.]	*2*	*0.75*	*1*	*1*	*1*	*8*
var6 [deg]	*14*	*14*	*15*	*15*	*25*	*45*

[12] Target function Eq. (3.1) represents the fit quality between measured and simulated FFPs.

Table 7.2 *Optimum values of the raytracing parameters of the non-aged and aged Asahi's fibre (LUMINOUS TB-1000). See Table 4.2 for the aging times and Table 3.3 for the parameter description.*

	A-set0	A-set1	A-set2	A-set3	A-set4	A-set5
var1 [deg]	4.5	3.9	3.9	2.9	2.5	5.5
var2 [dB/km]	115	125	120	120	120	160
var3 [mdB]	0.20	0.30	1.20	1.15	1.45	2.40
var4 [mm]	107	11.5	6.8	2	2.75	1.175
var5 [a.u.]	8.0	1.1	1.1	0	0.45	0
var6 [deg]	45	30	90	-	20	-

Table 7.3 *Optimum values of the raytracing parameters of the non-aged and aged Toray's fibre (PGU FB-1000). See Table 4.2 for the aging times and Table 3.3 for the parameter description.*

	T-set0	T-set1	T-set2	T-set3	T-set4	T-set5
var1 [deg]	3.75	4.0	4.0	4.4	4.15	5.4
var2 [dB/km]	117	125	120	135	130	155
var3 [mdB]	0.4	0.6	1.20	1.30	1.30	1.75
var4 [mm]	17.7	22.0	10.7	7.75	8.50	3.30
var5 [a.u.]	2.0	1.2	0.8	0.7	0.66	0.3
var6 [deg]	25	21	40	60	40	90

Note that, as stated in Part 3.2.3.3, due to the random nature of the raytracing process and FFP simulation, the optimum values given in *Table 7.1* to *Table 7.3* cannot be understood as exact values, but rather as the middles of respective uncertainty intervals. *Table 7.4* lists sample uncertainties of the exact values on the example of the non-aged and strongly aged Mitsubishi's fibre (*M-set0* and *M-set5*).

Table 7.4 *Uncertainties of the optimum values of the raytracing parameters of the non-aged and strongly aged Mitsubishi's fibre (*M-set0 *and* M-set5*).*

	M-set0	M-set5
var1	± 0.3 deg	± 1.5 deg
var2	± 25 dB/km	± 50 dB/km
var3	± 0.04 mdB	± 0.06 mdB
var4	± 12.5 %	± 25 %
var5	± 0.6	[-4.0, +∞)
var6	± 3.5 deg	[-10, +45) deg

The uncertainties of optimum values of the raytracing parameters were found to be generally much lower for the non-aged than for the aged fibres and to increase with the aging time. This increasing parameters' uncertainties together with the worsening fit quality

(illustrated in Appendix A3, which compares the measured and simulated FFPs) suggest that the developed model allows faithful modelling of non-aged or short-term aged fibres, but in course of a long-term high temperature aging additional attenuation and/or scattering mechanisms occur that are not enough well implemented in the model or not enough well covered by the scattering angle-dependence of the form Eq. (2.86).

Note that the particularly high uncertainty of the optimised value of *var2* (bulk core attenuation) can be attributed to the small length difference (approx. 10 m) between the shortest and the longest investigated sample. The attenuation uncertainty of ± 25 dB/km corresponds to ± 0.25 dB (± 6 % transmission) uncertainty on the measured 10 m distance. Measuring and simulating much longer fibres would increase the quality of the fit, but would require much longer simulation and optimisation time. On the other hand high uncertainties of *var5* and *var6* for long-aged fibre are related rather to their specific optimum values (making the scattering intensity almost constant for all illumination angles within the acceptance angle, i.e. up to 30°, see Part 7.5) than to the optimisation inaccuracies.

As examples in *Fig. 7.1* the target function dependence on two sample parameters is shown (*var3* and *var4*, i.e. interface attenuation and bulk scattering scale). The fibre *M-set2* and the optimum parameter values from *Table 7.1* were used. Each of the seven FFPs (*M-set2-1-24* to *M-set2-3-06*) used for computing the target function (see Eq. (3.1)) was simulated with 4000 rays. The minima correspond to the optimum values of both parameters.

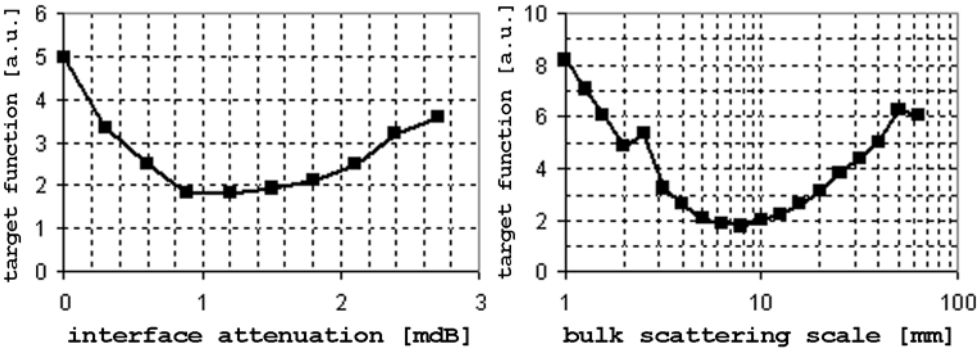

Fig. 7.1 *Target function dependence on interface attenuation (var3, left) and bulk scattering scale (var4, right). The fibre M-set2 and the optimum parameter values from Table 7.1 were used. Each FFP used for computing the target function was simulated with 4000 rays.*

7.2 Overall attenuation

Table 7.1 to *Table 7.3* show, between others, the dependence of the attenuation parameters *var2* and *var3* on the aging time. However, the actual overall attenuation of the simulated fibre depends not only on the two attenuation parameters but also on the scattering parameters and on the illumination conditions; it can be obtained only by performing a simulation. *Fig. 7.2* to *Fig. 7.4* compare two measured relative transmissions of aged to a different degree 10 m fibre samples (i.e. the online transmission measured on the hot fibre and the transmission of the same-time aged cold fibre, see *Fig. 4.10* to *Fig. 4.11*) with the relative transmission of 10 m simulated fibre. The curves illustrate the

aging process at 100 °C / <<50 % RH (as *Fig. 7.2* to *Fig. 7.4* and data in *Table 7.1* to *Table 7.3* do). The illumination angle of 0° has been used; the high numerical apertures of the LED used in the online measurement system (Part 4.4) and of the illuminating silica fibre in the spectrometer setup (Part 4.3) were simulated by a high divergence of the illuminating beam (15° ≈ 0.26 rad).

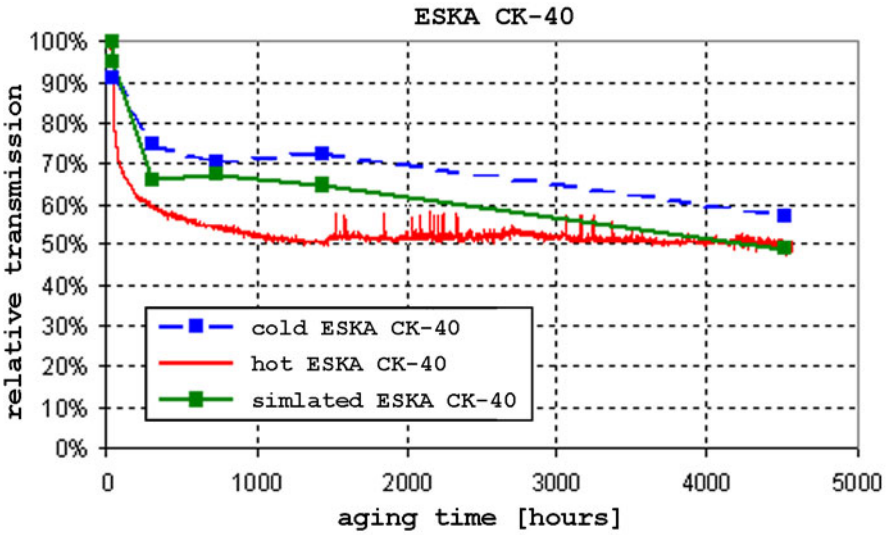

Fig. 7.2 *Relative transmission of the hot (online), the cold (cooled down) and the simulated 10 m samples of Mitsubishi's fibre in dependence on the aging time (650 nm wavelength, 100 °C / <<50 % RH).*

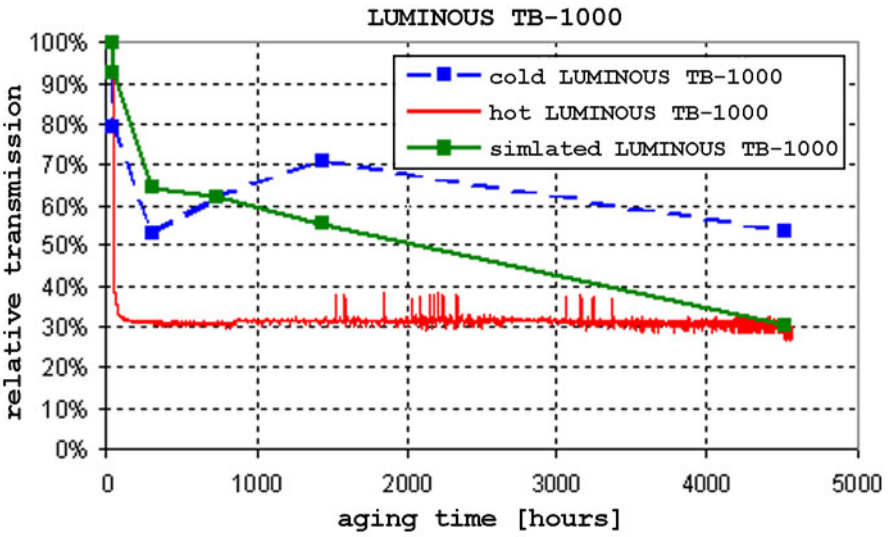

Fig. 7.3 *Relative transmission of the hot (online), the cold (cooled down) and the simulated 10 m samples of Asahi's fibre in dependence on the aging time (650 nm wavelength, 100 °C / <<50 % RH).*

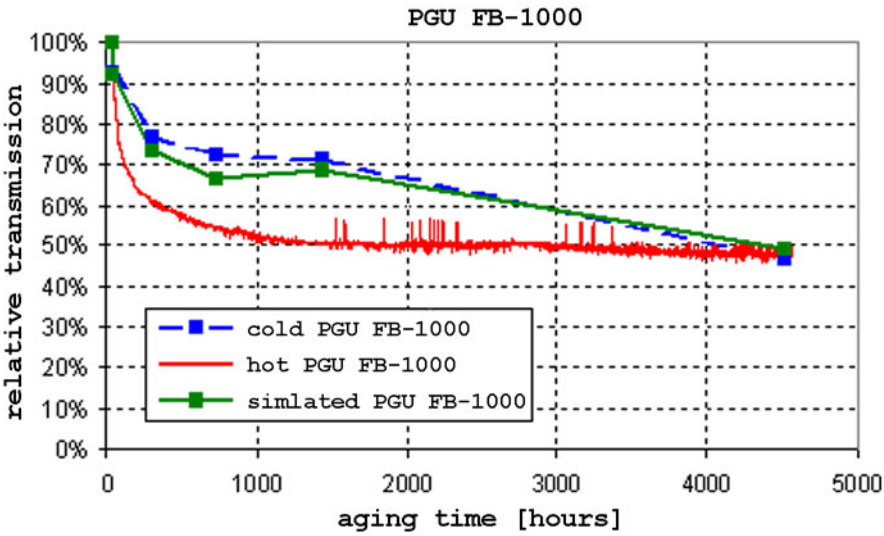

Fig. 7.4 *Relative transmission of the hot (online), the cold (cooled down) and the simulated 10 m samples of Toray's fibre in dependence on the aging time (650 nm wavelength, 100 °C / <<50 % RH).*

Comparison between the simulation (green) and the measurement is to be made for the cold fibre (blue), because only the FFPs of the cold samples were measured (Chapter 6) and used for the parameter fitting. Note the good match in the case of the Toray's fibres (*Fig. 7.4*). The simulated Asahi's fibres (*Fig. 7.3*) have provided the worst match, nevertheless the overall transmission of the simulated and measured fibre *A-set3* (both fourth points in *Fig. 7.3*) match exactly.

As mentioned above, several parameters influence the overall attenuation. In the next parts of this chapter changes of separate parameters with the aging time are discussed.

7.3 Core-clad interface attenuation

Fig. 7.5 shows the interface attenuation coefficient (*var3*) in dependence on the aging time for the fibres from all three manufacturers. Note that the aging time axis is shown in logarithmic scale.

The clear sharp increase in the fitted interface attenuation during the first hours and days of aging can be attributed to a rapid physical deterioration of the core-clad interface, presumably caused by the temperature shock.

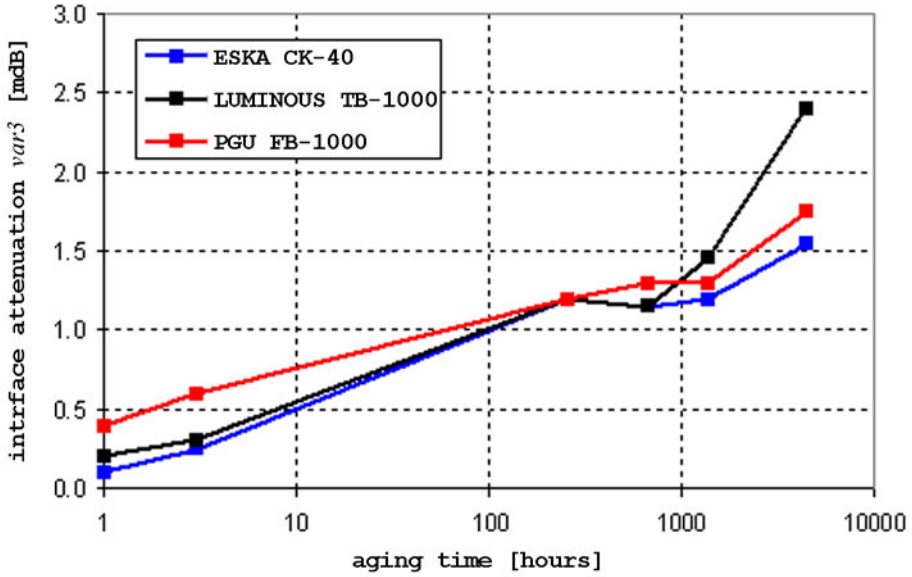

Fig. 7.5 *Fitted interface attenuation coefficient (var3) in dependence on the aging time.*

7.4 Bulk core attenuation

Fig. 7.6 shows the core bulk attenuation (*var2*) in dependence on the aging time for the fibres from all three manufacturers. As on *Fig. 7.5*, the aging time axis is shown in logarithmic scale.

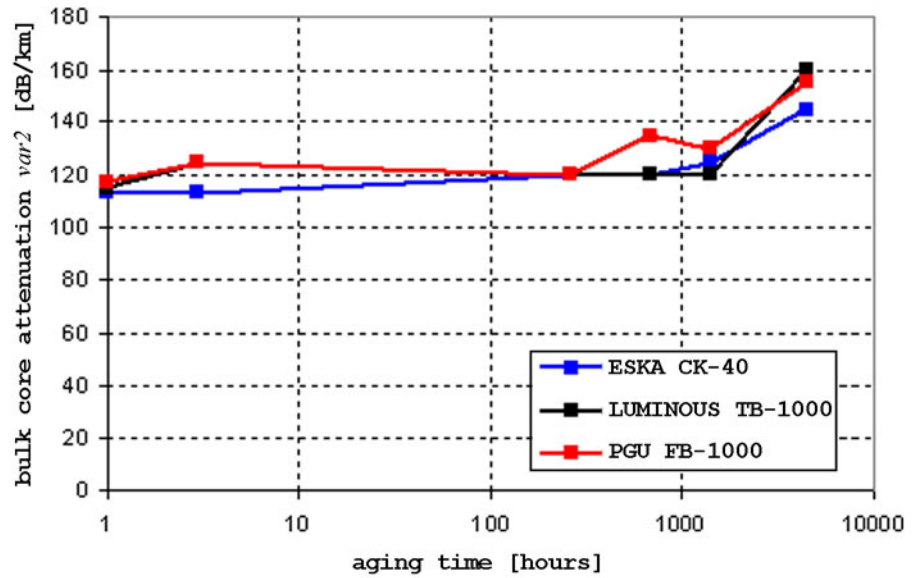

Fig. 7.6 *Fitted bulk core material attenuation (var2) in dependence on the aging time.*

The fitted bulk core material attenuation remains almost constant during most of the aging process (in contrast to *var3* of the previous part). A noticeable increase happens at the end of the exposure, first after 4000 h, compared to the immediate increase of the interface attenuation in *Fig. 7.5*. It suggests that the chemical deterioration of the fibre material (represented by *var2*) progresses much slower than the deterioration of the fibre's physical structure (*var3*). The bulk core attenuations of all three fibres show similar dependence on the aging time, as expected from the fact that the core material in all three cases is the same (PMMA, *Table 4.2*).

7.5 Scattering

Fig. 7.7 to *Fig. 7.9* show the fitted angle-dependent simulated scattering intensity in dependence on the aging time (computed with Eq. (2.86) and divided by *var4* to get rid of the normalisation present there). On all three figures it is given in the same arbitrary units per millimetre. As almost all rays propagate within fibre's acceptance angle and thus almost only those rays were used in optimisation of the parameters, the scattering intensity is plotted only for the illumination angles between 0° and 30°. Note the difference in the scaling of the vertical axes between the figures. The label order in the legend box corresponds to the curve order at 0° illumination angle.

As expected from the theoretical investigations of the Chapter 2 and Appendix A2, the scattering intensity decreases with the increasing illumination angle and tends to increase with the increasing aging time. Higher attenuation of the aged Asahi's fibres compared to the fibres from the other two manufacturers (*Fig. 4.2*) seems to be caused primarily by the much quicker increase of the scattering intensity with the aging time.

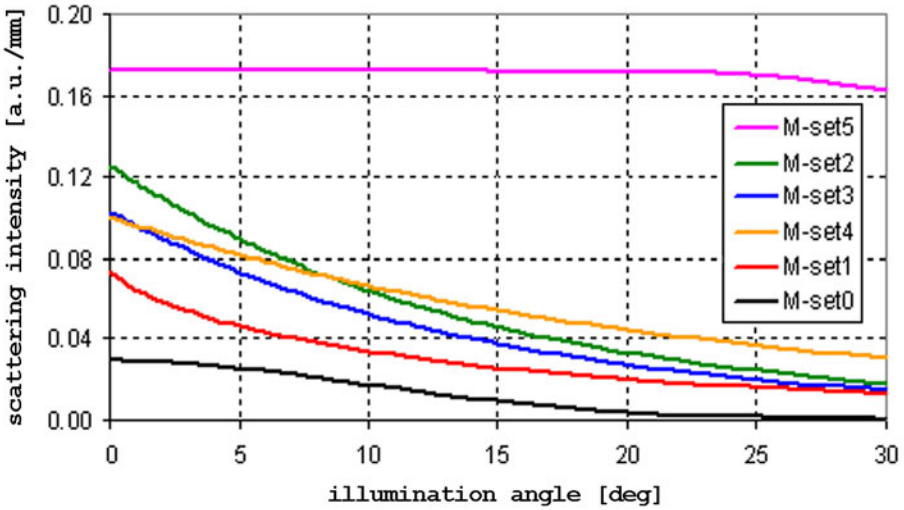

Fig. 7.7 *Fitted angle-dependent scattering intensity of Mitsubishi's fibre for all six aging times.*

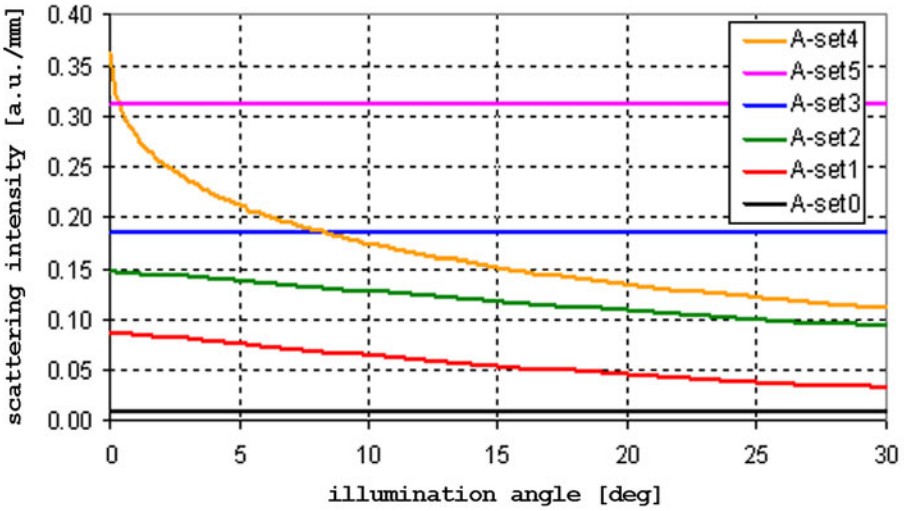

Fig. 7.8 *Fitted angle-dependent scattering intensity of Asahi's fibre for all six aging times.*

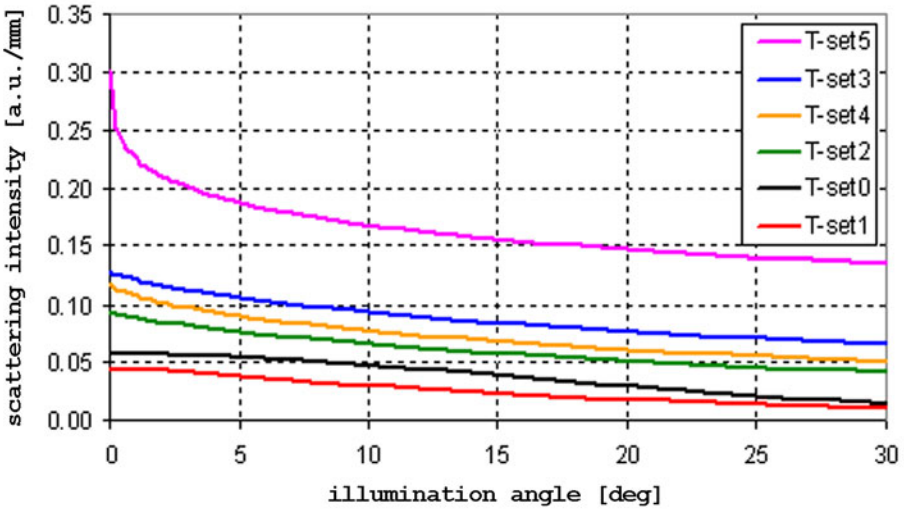

Fig. 7.9 *Fitted angle-dependent scattering intensity of Toray's fibre for all six aging times.*

Fig. 7.10 compares the fitted scattering intensities of all three investigated non-aged fibres (*M/A/T-set0* from *Fig. 7.7* to *Fig. 7.9*). It confirms the assumptions stated already in Part 6.4.1 and based on the measured FFPs' shapes (*Fig. 6.6* to *Fig. 6.8*): the non-aged Toray's fibre (red) shows the highest scattering; for small illumination angles the scattering of the non-aged Mitsubishi's fibre (blue) is higher than that of the non-aged Asahi's fibre (black), for greater illumination angles the relation is opposite.

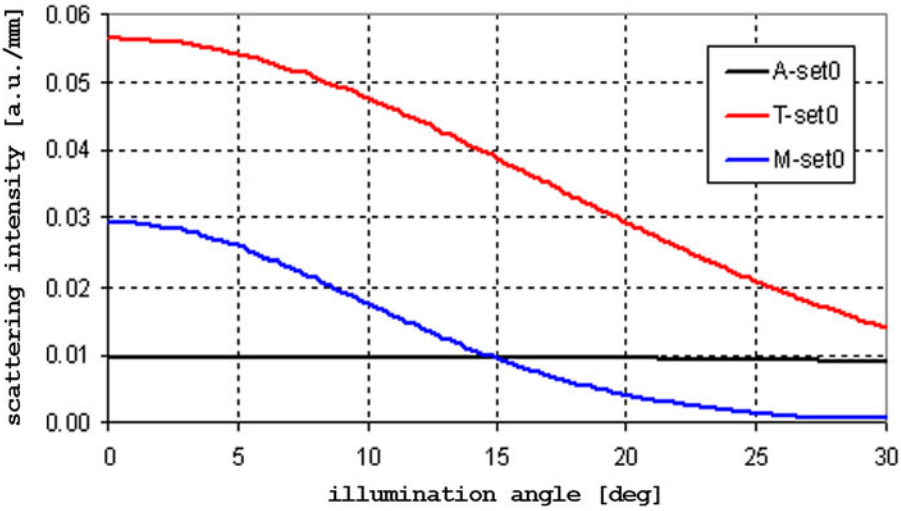

Fig. 7.10 *Fitted angle-dependent scattering intensity of non-aged fibres from all three manufacturers.*

8 Conclusions

The present Ph.D. work has combined an application-oriented as well as a theoretical approach to POF modelling. The precedence has been given to the practical issues and model verification, while at the same time much effort has been also spent on the mathematical analysis of the basic mechanisms governing light propagation in cylindrical waveguides, a prerequisite for reliable POF models and simulation.

In course of this work a practically usable general POF model has been developed; it implements the theoretically investigated mechanisms of scattering and Fresnel reflection. The first known systematic numerical optimisation of model parameters has been performed to get the best fit between simulated and measured optical characteristics of fibre samples. In extension to previous researches samples of different length and several illumination angles have been used. The results have been compared for fibres from three different manufacturers and subjected to six different aging times. The model was verified by providing a good agreement between simulated and measured FFPs, especially for non-aged fibres.

The important aspects of the work can be more detailed summarised as follows:

- Theoretical investigations of this work contain the first known attempt to use the wave-optics approach in the analysis of angular properties of scattering in cylindrical waveguides. Computed numerical examples have confirmed the experimentally observed decreasing scattering intensity with increasing illumination angle, an important practical result, as the geometric optics analysis suggests the opposite relation.
- To investigate the aging influence on fibre optical properties was one of the main tasks of this work. The optimised values of the attenuation coefficients for aged fibres suggest that most of the profound transmission loss in the first days, weeks and even months of investigated high temperature aging (100 °C / <<50 % RH) is caused by a significant physical deterioration of the core-clad interface. Chemical aging-related effects in bulk fibre material affecting its attenuation occur first after several months of aging. This observation seems to be also confirmed by the results of chemical experiments of a parallel running Ph.D. work of A. Appajaiah.
- The investigations showed also a general strong increase in the scattering intensity during the course of the aging. At present, the implemented scattering mechanism cannot differentiate between the scattering effects related to core-clad interface and bulk material. Thus, it cannot be told, if the observed scattering increase originates from physical deterioration of the core-clad interface or chemical changes of fibre bulk material.
- The agreement between measurement and simulation for the non-aged fibres is substantially better than reported in previous researches [16]. On the other hand, the general decrease of the fit quality with fibre aging time suggests that in course of the high temperature aging additional attenuation and/or scattering mechanisms occur, which are not implemented in the proposed model or not enough well covered by the

used form of the scattering-angle dependence. Thus, the model itself can be in future research refined and improved.

- The fit quality between the simulated and measured far-fields (especially at low illumination angles and for the above-mentioned long, strongly aged fibres), can be further improved even with the current model by refining the optimisation process to obtain better numerical values of the parameters, mainly at the expense of the simulation time. Using longer fibre samples and more illumination angles, tracing more rays or dropping some of the constraints forced on the parameters could be useful for this purpose.
- In course of the work fibres subjected to only one aging condition were investigated (100 °C / <<50 % RH). The influence of other aging conditions on the optical parameters of the model (i.e. of other temperatures possibly combined with high humidity) could also be investigated and compared. The results of detailed analysis could lead to development of more efficient methods for prediction of optical transmission through POFs under long-term environmental stress.
- As a side effect of this work, a calibration and quality assessment procedure for CCD cameras has been developed. It was necessary to guarantee the reliability of far-field profile measurements, because camera manufacturers, in general, deliver neither such procedures nor reliability data.

Therefore, progress has been made concerning the modelling and simulation of light propagation in non-aged and aged POFs. Nevertheless, additional further improvements by future research are possible.

The theoretical part of the work leaves its mathematical problems open, too. Primarily, there is no rigorous analysis of radiation conditions that would guarantee the uniqueness of the discussed solution to the scalar wave equation on a cylindrical waveguide. The presumed conditions, formulated analogically to those holding for the open-space problem [25] and necessary to solve the corresponding Helmholtz equation [2], were stated here as a hypothesis only. Furthermore, the (decreasing) relation between the illumination angle and the scattering intensity was found on numerical examples only for two waveguide radii and two specific forms of the refractive index perturbation. A more universal estimation, based on general formulae, would be welcome, as well as a general estimation of the angle-dependence of the relative guided power, presumably stepwise for large-diameter fibres (as numerical computations have shown). Last but not least, the proof of the convergence of the von Neumann series representing the scattered field should be brought to the end.

Appendices

A1 Basic identities

Wronskians of Bessel functions [1, 3, 12]:

$$\begin{aligned} &Y_m(z)J_{m+1}(z)-J_m(z)Y_{m+1}(z)=\frac{2}{\pi z}, \\ &J_m(z)Y_{m-1}(z)-Y_m(z)J_{m-1}(z)=\frac{2}{\pi z}. \end{aligned} \tag{A1.1}$$

Asymptotic expansions of Bessel functions for large argument ($z \to \infty$) [1, 3]:

$$\begin{aligned} &J_m(z)\cong\left(\frac{2}{\pi z}\right)^{\frac{1}{2}}\cos\left(z-\frac{1}{2}m\pi-\frac{1}{4}\pi\right), \\ &Y_m(z)\cong\left(\frac{2}{\pi z}\right)^{\frac{1}{2}}\sin\left(z-\frac{1}{2}m\pi-\frac{1}{4}\pi\right). \end{aligned} \tag{A1.2}$$

Series of Bessel functions [1, 3]:

$$\exp(iz\cos\varphi)=\sum_{m\in\mathbf{Z}} i^m J_m(z)\cos(m\varphi)=\sum_{m\in\mathbf{Z}} i^m J_m(z)\exp(m\varphi), \tag{A1.3}$$

where the second equality follows from [1, 3, 12]:

$$\begin{aligned} &J_{-m}(z)=(-1)^m J_m(z), \text{ for } m\in\mathbf{Z}, \\ &Y_{-m}(z)=(-1)^m Y_m(z), \text{ for } m\in\mathbf{Z}. \end{aligned} \tag{A1.4}$$

Integral of Bessel functions [1, 3]:

$$\int zJ_m(az)J_m(bz)dz=\frac{z}{a^2-b^2}\left[bJ_m(az)J_{m-1}(bz)-aJ_m(bz)J_{m-1}(az)\right] \tag{A1.5}$$

Upper bounds of Bessel functions [3, 12]:

$$\begin{aligned} &|J_m(z)|\le 1, \text{ for } m\in\mathbf{Z}, \\ &\text{If } |J_m(z)|=1 \text{ and } m\in\mathbf{Z}, \text{ then } m=z=0 \text{ and } J_0(0)=1, \\ &|J_m(z)|\le 1/\sqrt{2}, \text{ for } m\in\mathbf{Z}, |m|>0 \end{aligned} \tag{A1.6}$$

Recurrence relations for Bessel functions [1, 3, 12]

$$\begin{aligned} &J_{m+2}(z)=\frac{2(m+1)}{z}J_{m+1}(z)-J_m(z), \\ &J_m(z)=\frac{z}{2m}\left[J_{m-1}(z)+J_{m+1}(z)\right], \text{ for } m\neq 0. \end{aligned} \tag{A1.7}$$

Infinite summations of Bessel functions [3, 12]

$$\sum_{m\in\mathbf{Z}} J_m^2(z) = 1\,. \tag{A1.8}$$

Power series expansion of $Y_m(z)$ at z=0 [3, 12]:

$$Y_m(z) = \frac{2}{\pi} J_m(z) \ln\frac{z}{2} - \frac{1}{\pi}\sum_{k=0}^{m-1} \frac{(m-k-1)!}{k!}\left(\frac{z}{2}\right)^{2k-m} + \\ -\frac{1}{\pi}\sum_{k=0}^{\infty} \frac{(-1)^k\left[\psi(k+1)+\psi(k+m+1)\right]}{k!(m+k)!}\left(\frac{z}{2}\right)^{2k+m}, \text{ for } m\in\mathbf{N}, \tag{A1.9}$$

where $\psi(z)$ is the digamma function $\psi(z)=\Gamma'(z)/\Gamma(z)$.

Eq. (A1.9) implicates the following limiting forms of $Y_m(z)$ for small argument $z\to 0$:

$$Y_0(z) \cong \frac{2}{\pi}\ln\frac{z}{2}\,, \\ Y_m(z) \cong -\frac{(m-1)!}{\pi}\left(\frac{2}{z}\right)^n, \text{ for } m\in\mathbf{N}_+. \tag{A1.10}$$

Power series expansion of $J_m(z)$ at z=0 and its limiting forms for small argument $z\to 0$ [1, 3]:

$$J_m(z) = \left(\frac{z}{2}\right)^m \sum_{k=0}^{\infty} \frac{(-1)^k}{k!(m+k)!}\left(\frac{z}{2}\right)^{2k}, \text{ for } m\in\mathbf{N}; \\ J_0(z) = 1 - \left(\frac{z}{2}\right)^2 + O\left(z^4\right) = 1 + O\left(z^2\right) \cong 1, \text{ as } z\to 0; \tag{A1.11} \\ J_m(z) = \frac{1}{m!}\left(\frac{z}{2}\right)^m + O\left(z^{m+2}\right) = O\left(z^m\right), \text{ as } z\to 0 \text{ for } m\in\mathbf{N}_+.$$

Derivatives of Bessel functions with respect to the argument [1, 3, 12]:

$$\frac{d}{dz}J_m(z) = \frac{m}{z}J_m(z) - J_{m+1}(z), \\ \frac{d}{dz}Y_m(z) = \frac{m}{z}Y_m(z) - Y_{m+1}(z)\,. \tag{A1.12}$$

Summations of Bessel function [3, 12]:

$$Y_k(z_1 - z_2) = \sum_{m\in Z} Y_{m+k}(z_1) J_m(z_2), \text{ for } |z_1| < |z_2|\,. \tag{A1.13}$$

Debye asymptotic formulae for large order ($|z| << m - m^{1/3}$, $m >> 0$) [1, 3]:

$$J_m(z) \cong \frac{1}{\sqrt{2\pi}} \left(m^2 - z^2\right)^{-\frac{1}{4}} \exp\left(-m \cosh\frac{m}{z} + \left(m^2 - z^2\right)^{\frac{1}{2}} \right),$$

$$Y_m(z) \cong -\sqrt{\frac{2}{\pi}} \left(m^2 - z^2\right)^{-\frac{1}{4}} \exp\left(m \cosh\frac{m}{z} - \left(m^2 - z^2\right)^{\frac{1}{2}} \right). \quad \text{(A1.14)}$$

Eq. (A1.13) implicates that for enough large order m and constant argument z:

$J_m(z)$ monotonically decreases to zero as $m \to \infty$,
$Y_m(z)$ monotonically decreases to $-\infty$ as $m \to \infty$. (A1.15)

A2 Sample modal analysis

In this appendix modal characteristics of sample waveguides (mainly of two waveguides with normalised frequency parameters $V = 8$ and $V = 20$) are numerically computed and investigated. The results illustrate the theoretical discussion of Chapter 2, Part 2.1.

Some numerically computed properties of waveguides investigated in this part were used, due to the lack of exact formulas, as the basis for two general assumptions needed for modelling the scattering within the raytracing approach in Part 2.2:

- Numerically computed results concerning the mode mixing (aroused due to four tested random forms of the refractive index perturbations, Part A2.3) form the basis for the general formula approximating the angle-dependent scattering intensity (Part 2.2.3, Eq. (2.87)).
- Based on the results concerning excitation of guided modes for both investigated waveguides (Part A2.2, *Fig. A2.10*) it is assumed that for the illumination angles lying within the acceptance angle the overwhelming part of the input power enters guided modes. Therefore, taking also into account the quick attenuation of radiating modes in a real fibre, mode mixing analysis can be limited to the power flow between the guided modes only (Part A2.3).

All fibres investigated in this part differ only in their normalised frequency (and so in their diameters), all other parameters are assumed to be equal those of a typical POF, the wavelength equals 653 nm, so that of the laser used in the experiments (Part 5.2).

$n_0 = 1.492$,
$n_1 = 1.402$,
$\lambda = 653$ nm (red laser used in experiments),
$k = 2\pi/\lambda \approx 9.622 \times 10^6$. (A2.1)

According to Eq. (2.19), normalised frequency V of 8 and 20 corresponds to the fibre diameters of 3.26 μm and 8.14 μm, respectively.

A2.1 Modes

All guided modes of waveguides with $V = 8$ and $V = 20$ were computed by numerically solving equation Eq. (2.22). Equation Eq. (2.24) in both cases has no guided-mode solutions (i.e. for $|m|>1$). The waveguide with $V = 8$ supports 17 guided modes (for $m \in \{-5, -4, \ldots, 4, 5\}$), while the other waveguide ($V = 20$) supports a total of 105 guided modes ($m \in \{-16, -15, \ldots, 15, 16\}$). All the guided modes of both waveguides together with the corresponding relative wavenumber β are listed in *Table A2.1* and *Table A2.2*. Note that Eq. (2.22) has the same solutions for $+m$ and $-m$ modes, i.e. the corresponding modes in both cases have the same relative wavenumber β, the same radial component $j_m(r,\tau)$ and differ only in the oscillating term $exp(\pm im\varphi)$ (see Eq. (2.12)). *Table A2.1* and *Table A2.2* present (numerically obtained) all solutions to Eq. (2.22) for different values of the integer parameter m. They correspond to the zeros of Eq. (A2.2) and each of them represents one guided mode of form Eq. (2.21).

Table A2.1 *Numerical characteristics of guided modes for the $V = 20$ waveguide.*

m	relative mode wavenumber β						
0	*1.404*	*1.427*	*1.448*	*1.464*	*1.477*	*1.486*	*1.491*
±1	*1.416*	*1.438*	*1.457*	*1.471*	*1.482*	*1.489*	
±2	*1.405*	*1.428*	*1.448*	*1.465*	*1.478*	*1.487*	
±3	*1.417*	*1.440*	*1.458*	*1.473*	*1.484*		
±4	*1.406*	*1.430*	*1.451*	*1.468*	*1.481*		
±5	*1.420*	*1.443*	*1.462*	*1.477*			
±6	*1.410*	*1.434*	*1.455*	*1.472*			
±7	*1.425*	*1.448*	*1.468*				
±8	*1.416*	*1.441*	*1.462*				
±9	*1.406*	*1.433*	*1.456*				
±10	*1.424*	*1.450*					
±11	*1.415*	*1.443*					
±12	*1.405*	*1.436*					
±13	*1.428*						
±14	*1.420*						
±15	*1.411*						
±16	*1.402*						

Table A2.2 *Numerical characteristics of guided modes for the $V = 8$ waveguide.*

m	0	±1	±2	±3	±4	±5
relative mode wavenumber β	*1.414*	*1.440*	*1.418*	*1.448*	*1.430*	*1.410*
	1.459	*1.476*	*1.464*			
	1.486					

Fig. A2.1 shows for the $V = 20$ waveguide sample graphs of the function

(A2.2) $$f(\beta) := w_0 R \frac{J_{m+1}(w_0 R)}{J_m(w_0 R)} - w_1 R \frac{K_{m+1}(w_1 R)}{K_m(w_1 R)},$$

for m=0 and m=16, whose (numerically found) zeros correspond to the respective guided modes, see Eq. (2.22). Values of w_0R and w_1R are bound to β by Eq. (2.19) and to each other by the identity $400 = V^2 = (w_0 R)^2 + (w_1 R)^2$.

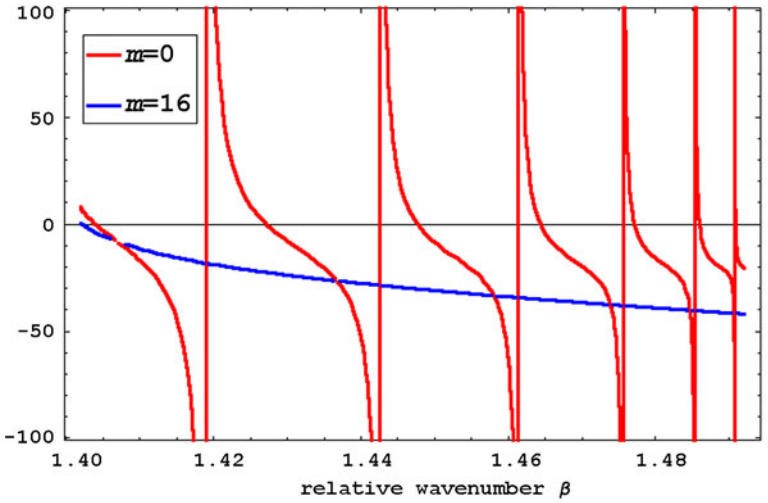

Fig. A2.1 *Function $f(\beta)$ of Eq. (A2.2) with V=20 for m=0 (red) and m=16 (blue). The zeros (to be found numerically) correspond to the respective guided modes.*

Guided modes are usually described with LP_{mk} symbol, where m corresponds to the rows in *Table A2.1* (columns in *Table A2.2*) and $k \in \mathbf{Z}$ is assigned (starting with 0) upwards columns of *Table A2.1* (right to left in *Table A2.2*), i.e. corresponding to the increasing values of parameter w_0R or decreasing values of β. *Fig. A2.2* shows descriptions of all the guided modes of the $V = 8$ waveguide in the $(w_0R, |m|)$ coordinate system.

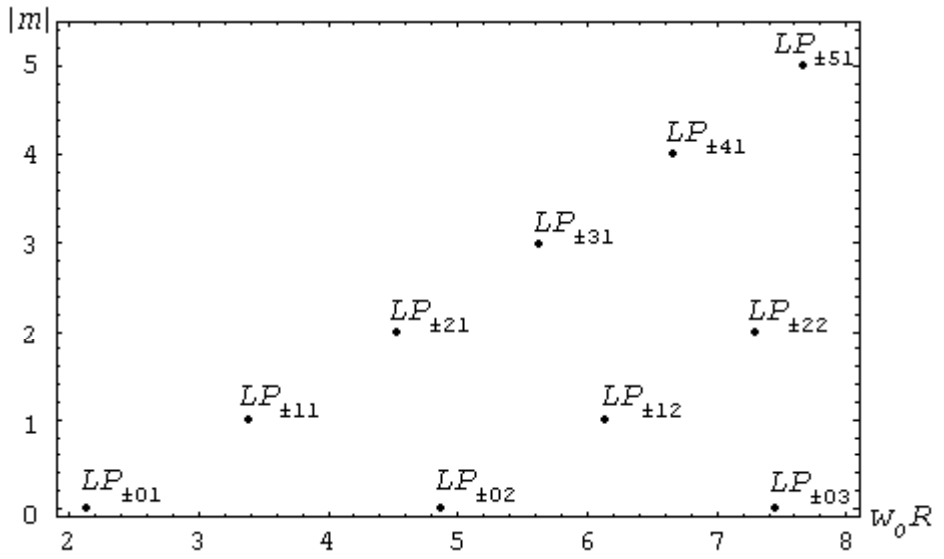

Fig. A2.2 *Descriptions of all guided modes of the $V = 8$ waveguide in the $(w_0R, |m|)$ coordinate system.*

Fig. A2.3 compares guided modes of both waveguides in the same coordinate system.

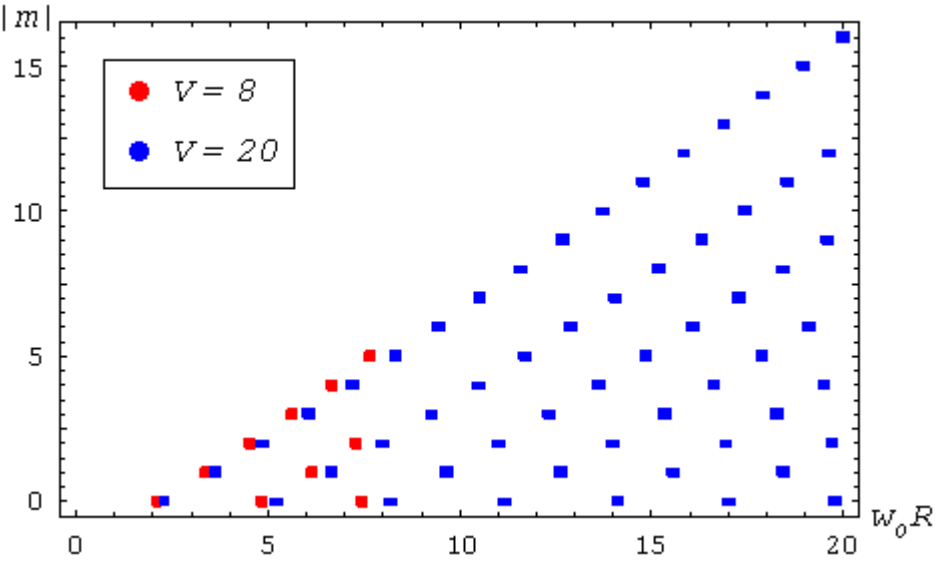

Fig. A2.3 *Guided modes of the $V = 8$ (red) and the $V = 20$ (blue) waveguide in the $(w_0R, |m|)$ coordinate system.*

The real parts of four sample guided modes Eq. (2.21) over the $V = 8$ waveguide's cross-section are shown in *Fig. A2.4*, while *Fig. A2.5* shows real parts of two sample guided modes Eq. (2.21) of the $V = 20$ waveguide. Their squared value is proportional to the local energy distribution of the respective mode.

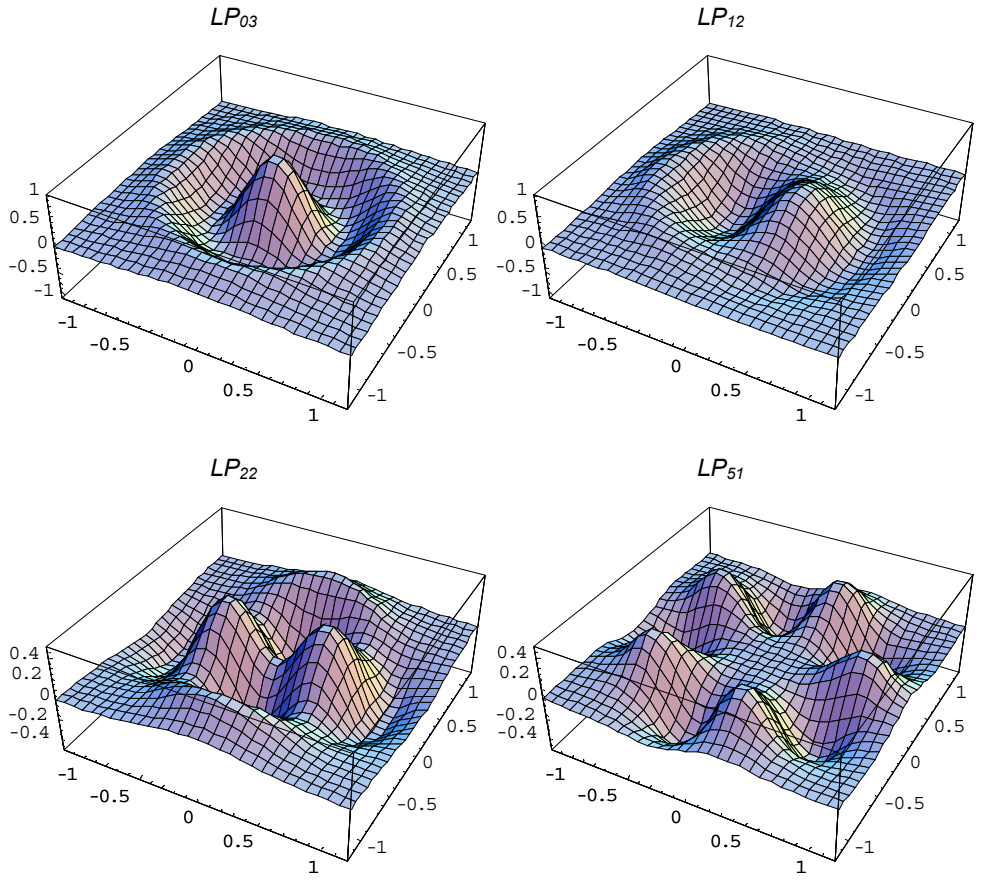

Fig. A2.4 *Real parts of four guided modes on the cross-section of the $V = 8$ waveguide. The waveguides' radii were scaled to unity (horizontal axes).*

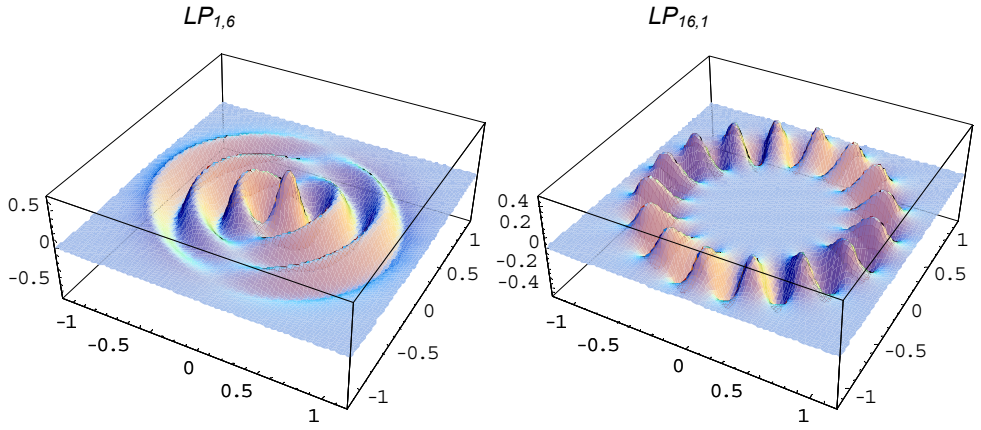

Fig. A2.5 *Real parts of two guided modes on the cross-section of the $V = 20$ waveguide. The waveguides' radii were scaled to unity (horizontal axes).*

As showed in Chapter 2, Part 2.1.2, for each $\tau < n_1^2$ and each $m \in \mathbf{Z}$ exists a corresponding radiating mode. *Fig. A2.6* shows real parts of two sample radiating modes Eq. (2.27) of both waveguides.

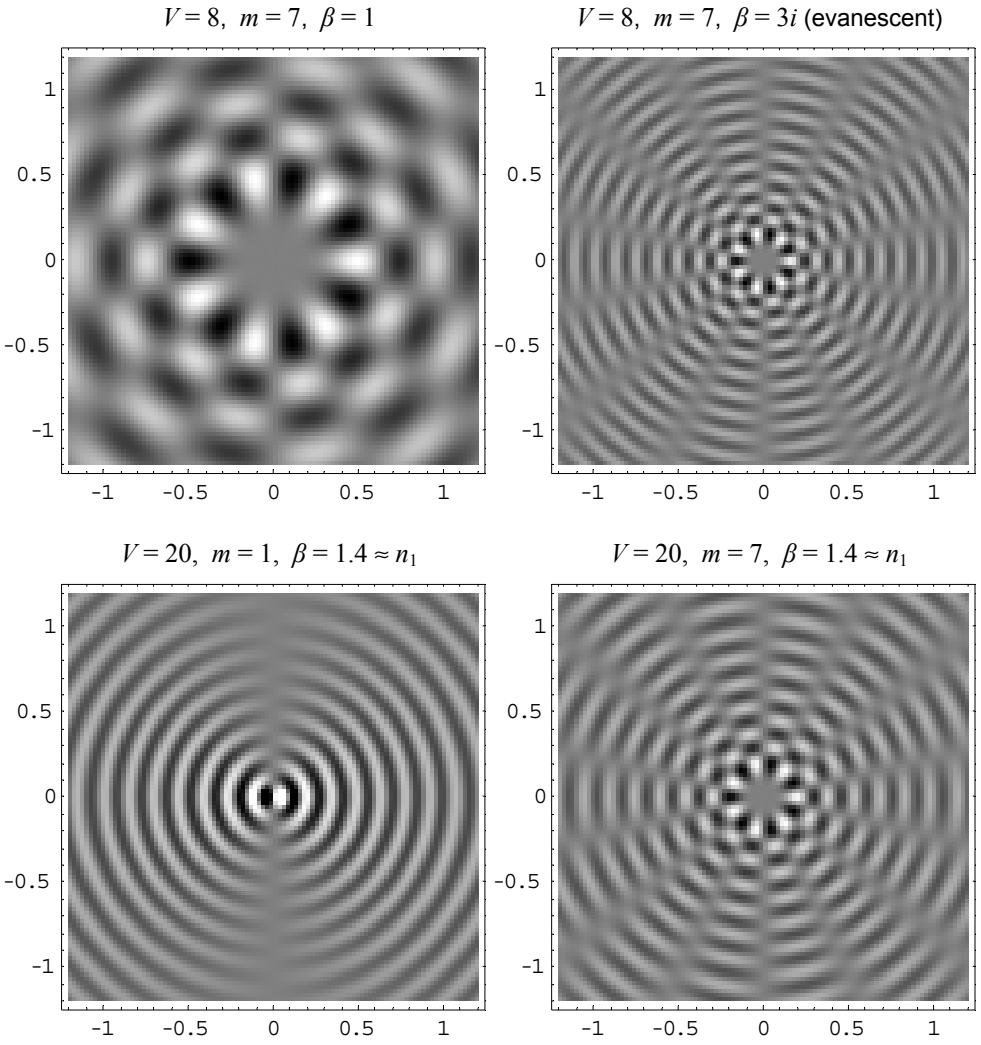

Fig. A2.6 *Top view on the real parts of four sample radiating modes on the cross-sections of two waveguides. The waveguides' radii were scaled to unity. The white (black) colour corresponds to the maximum (minimum) value.*

The basic guided mode (LP_{01}) was also found for two other waveguides with the normalised frequency parameter V equal to 100 and 500. *Fig. A2.7* compares in logarithmic scale its radial components $j_0\left(r, \tau_1^0\right)$ for all four waveguides. *It* shows that the field of LP_{01} mode extending into the clad decays exponentially with waveguide's radius and that the decay rate increases with waveguide's radius (or its normalised frequency).

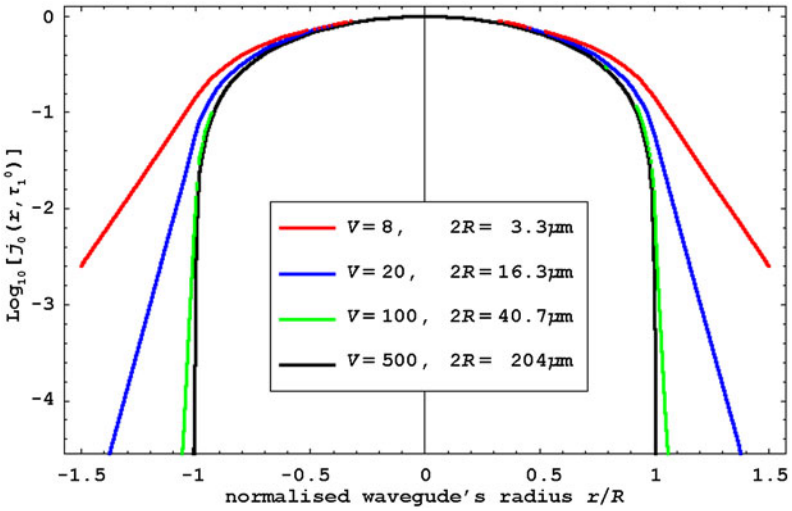

Fig. A2.7 *Radial component of LP_{01} mode for four different waveguides' radii (logarithmic scale).*

A2.2 Illumination and mode-angle relation

Using formula Eq. (2.46) we can compute the excitation of each guided mode of a waveguide with a uniformly illuminated input face. Summing Eq. (2.47) over all guided modes gives the total guided power. In this part we will use $p(\alpha) \equiv 1$ in Eq. (2.46), thus we will neglect the effects of slightly increasing with angle Fresnel reflection coefficient and assume that all power incident on the waveguide's input face actually enters it and excites its modes.

Fig. A2.8 shows relative excitations (the ratio of the power entering the mode to the total incident power) of all guided modes of the $V = 8$ waveguide in dependence on the illumination angle. Power in both $LP_{\pm mp}$ modes were added, whenever $|m|>0$

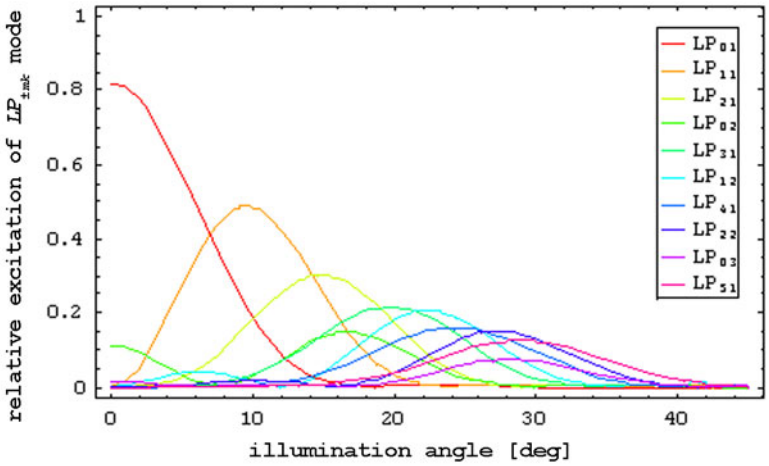

Fig. A2.8 *Relative excitation (the ratio of the power entering the mode to the total incident power) of all guided $LP_{\pm mp}$ modes of the $V = 8$ waveguide in dependence on the illumination angle α.*

Fig. A2.9 shows for both $V = 8$ and $V = 20$ waveguides the dependence on the illumination angle of the excitation of LP_{01} mode and of two other modes with the excitation maxima around 0°, 15° and 30°, respectively. The maxima of all graphs were normalised to 100 % to ease comparison of their shapes.

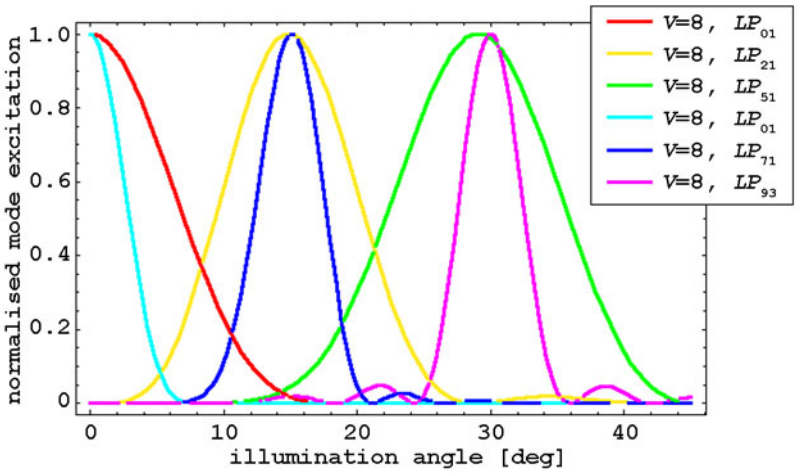

Fig. A2.9 *Dependence on the illumination angle of the normalised excitation of three sample modes with the optimum inclination about 0°, 15° and 30° for both $V = 8$ and $V = 20$ waveguides.*

Fig. A2.10 shows the angle-dependence of the relative total guided power for both waveguides (ratio of the power contained in all guided modes to the total incident power).

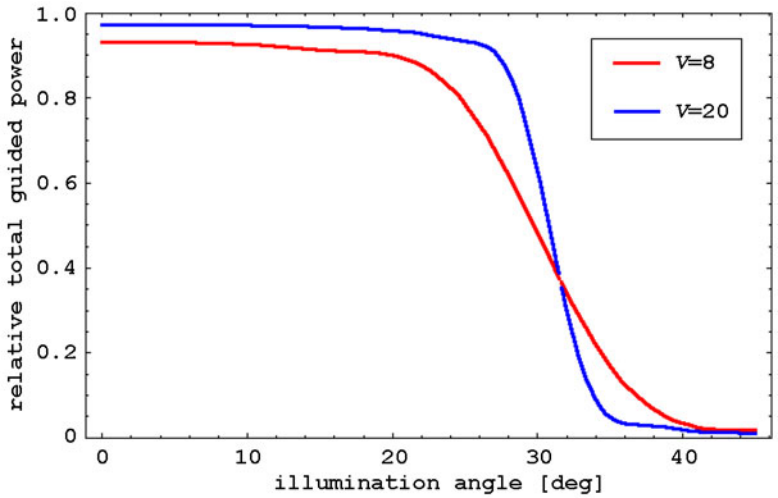

Fig. A2.10 *Relative total guided power in dependence on illumination angle for both $V = 8$ and $V = 20$ waveguides.*

Fig. A2.10 clearly suggests that with increasing waveguide's radius R (or its normalised frequency V) almost all power incident within the acceptance angle enters guided modes and so the limiting graph is step-like, see [1, Chapter 20]. For each investigated mode there

is the optimum input illumination angle, which maximises the power entering the mode (the maximum of the plots on *Fig. A2.8* and *Fig. A2.9*). Based on the *Fig. A2.9*, it may be assumed that for each guided mode of any waveguide (i.e. waveguide of any parameter V) there exists a similar peak of the excitation graph and that its dispersion tends to decrease with the increasing waveguide parameter V (and the waveguide's radius R), as on *Fig. 2.10*, so that for a highly multimode waveguide each guided mode may be practically uniquely related to its optimum illumination angle, called its *external propagation angle* (as related to the outside environment, so α and not γ on *Fig. 2.3*). *Fig. A2.11* shows the relation between the modal parameter w_0R of the mode and its optimum illumination angle, see [1, Chapter 20] for discussion and references.

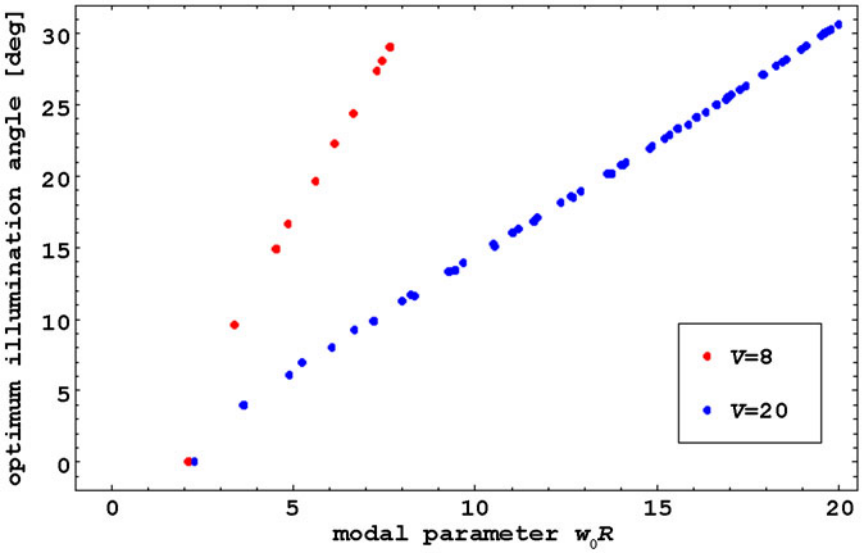

Fig. A2.11 *Optimum input illumination angle in dependence on the modal parameter w_0R for the $V = 8$ (left) and $V = 20$ (right) waveguide.*

According to the formulae Eq. (2.33), Eq. (2.34) and Eq. (2.46) propagating power is distributed continuously with respect to τ among radiating modes. The distribution function $p(\tau)$ is given by:

(A2.3) $$p(\tau) = k^2\pi \sum_{m\in\mathbf{Z}} \frac{|G_m(\tau,0)|^2}{a_m^2(\tau)+b_m^2(\tau)}\,.$$

To get the total power contained in all radiating modes the formula Eq. (A2.3) for $p(\tau)$ has to be integrated with respect to τ within the limits $(-\infty,\ n_1^2)$, as Eq. (2.48) states. *Fig. A2.12* shows the relative power distribution $p(\tau)/\pi R^2$, see Eq. (2.49), of the $V = 8$ waveguide for four different illumination angles, while *Fig. A2.13* compares $p(\tau)/\pi R^2$ of both $V = 8$ and $V = 20$ waveguides for 15° illumination angle. Summing over $m\in\mathbf{Z}$ in both cases was made only over $m\in\{-20, \ldots, 20\}$ or $m\in\{-80, \ldots, 80\}$ for the $V = 8$ or $V = 20$ waveguide, respectively. Both figures are shown in logarithmic scale.

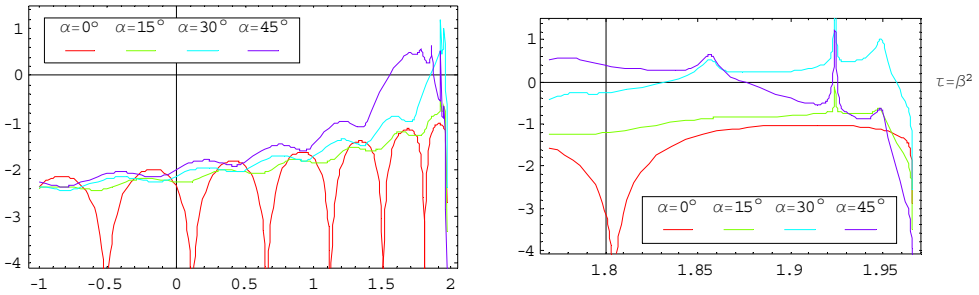

Fig. A2.12 *Relative power distribution among radiating modes of the $V = 8$ waveguide for four illumination angles.*

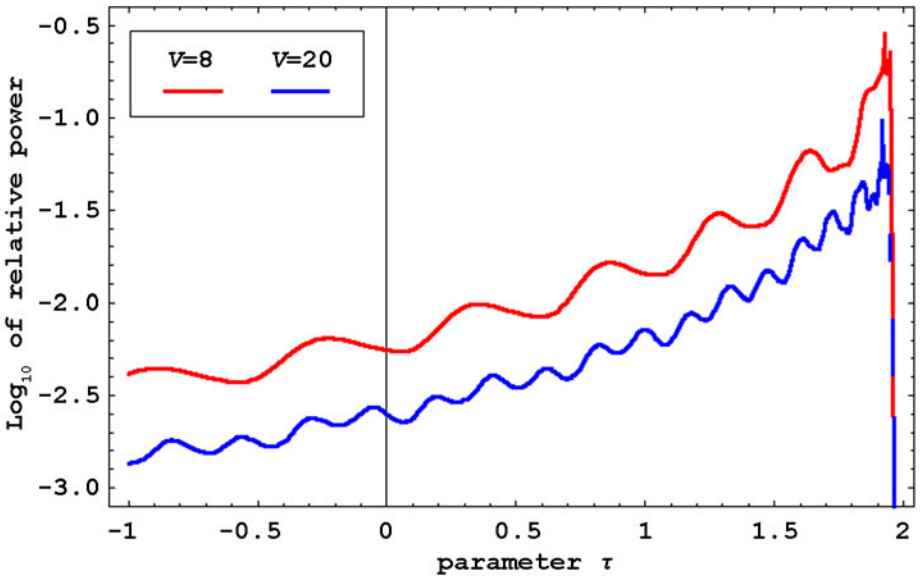

Fig. A2.13 *Relative power distribution among radiating modes of both $V = 8$ and $V = 20$ waveguides at 15° illumination angle.*

Fig. A2.13 clearly shows that the excitation of radiating modes in the $V = 20$ waveguide is considerably lower that in the $V = 8$ waveguide and in the former more power is transported via guided modes, as *Fig. A2.10* shows. From both figures it may be seen and assumed that the more multimode is the waveguide, the less power enters its radiating modes (for illumination angles within the acceptance angle).

A2.3 Scattering and mode mixing

A2.3.1 On input and end faces

Formula Eq. (2.53) allows calculating distribution of the output power per solid angle, depending on the illumination angle and under assumption of no power transfer between modes. *Fig. A2.14* shows sample graphs of angular distribution of the total output power for both investigated waveguides and several different illumination angles α.

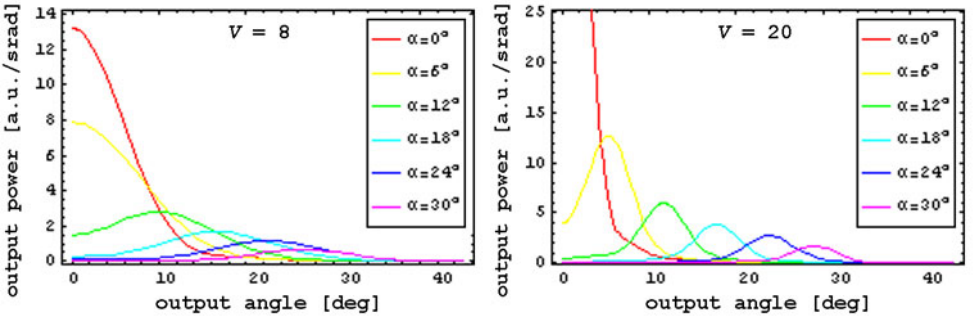

Fig. A2.14 *Angular distributions of the total output power for both waveguides; plots for different illumination angles α. No power transfer between modes assumed.*

Both figures confirm that the conversions between the illuminating/output fields and the modal fields on endfaces diffuse the angular input characteristics. To compute the scale of the diffusion, i.e. the angle-dependent dispersion of the output power, the graphs of *Fig. A2.14* were numerically square-best-fitted with respect to the dispersion parameter s with the (reflected at 0) Gaussian dispersion characteristics:

(A2.4) $$\psi(\alpha_{out};\alpha,s) := \psi_0(\alpha_{out};\alpha,s) + \psi_0(-\alpha_{out};\alpha,s),$$

where α is the illumination angle, α_{out} the output angle and

(A2.5) $$\psi_0(\alpha_{out};\alpha,s) = \frac{A}{s\sqrt{2\pi}} \exp\left[-\frac{(\alpha_{out}-\alpha)^2}{s^2}\right].$$

Amplitudes A for each illumination angle α were kept constant and equal to the integral of the respective curve. The fitted values of dispersions s are shown in *Fig. A2.15*.

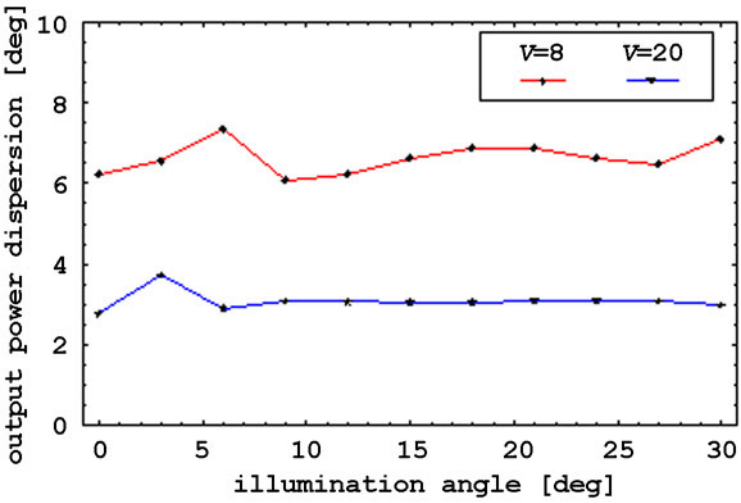

Fig. A2.15 *The dispersions* s *of the curves Eq. (A2.4), which best fit the angular distribution of the total output power (Fig. A2.14).*

The parameter s characterising the angle-dependent dispersion of the scattered power turned out to be almost constant across all illumination angles and for both investigated waveguides. Therefore, it will be henceforth assumed (and used in the raytracing software) that the scattering on fibre's endfaces is constant and does not depend on the illumination angle.

A2.3.2 Refractive index perturbations

Given the refractive index perturbation function d (defined in Eq. (2.54)), the formulae Eq. (2.71) to Eq. (2.73) can be used to investigate the angular dependence of the total power and the dispersion of the scattered field. In the numerical computations for the perturbation function a finite sum of simple single perturbations will be used:

$$d(\rho,\eta,\xi)=\sum_{l=1}^{L} A_l \exp\left[-\frac{\delta^2(\rho,\eta,\xi;\rho_l,\eta_l,\xi_l)}{S_l^2}\right], \tag{A2.6}$$

where the point (ρ_l, η_l, ξ_l) is the centre of a single perturbation, A_l is its amplitude and S_l defines its e^{-1} radius. The best candidate for the distance function δ would be the Euclidean metric

$$\begin{aligned}&\delta^2(\rho_0,\eta_0,\xi_0;\rho_1,\eta_1,\xi_1)=\\ &=(\xi_0-\xi_1)^2+(\rho_0\cos\eta_0-\rho_1\cos\eta_1)^2+(\rho_0\sin\eta_0-\rho_1\sin\eta_1)^2=\\ &=(\xi_0-\xi_1)^2+\rho_0^2+\rho_1^2-2\rho_0\rho_1\cos(\eta_0-\eta_1),\end{aligned} \tag{A2.7}$$

but this form would make integral Eq. (2.71) symbolically not integrable and considerably increase its computation time. So the following function was used instead, a modified version of Eq. (A2.7):

$$\begin{aligned}&\delta^2(\rho_0,\eta_0,\xi_0;\rho_1,\eta_1,\xi_1)=\\ &=(\xi_0-\xi_1)^2+\rho_0^2+\rho_1^2-2\rho_0\rho_1\left[1-\frac{2}{\pi}|\eta_0-\eta_1|\right]=\\ &=(\xi_0-\xi_1)^2+(\rho_0-\rho_1)^2+\frac{4}{\pi}\rho_0\rho_1|\eta_0-\eta_1|,\end{aligned} \tag{A2.8}$$

where for $(\eta_0-\eta_1)\in(-\pi,\pi]$ the $\cos(\eta_0-\eta_1)$ was approximated with the saw function $1-2|\eta_0-\eta_1|/\pi$, which equals the effect of keeping the Euclidean metric Eq. (A2.7) but modifying slightly the perturbation function Eq. (A2.6).

Substituting Eq. (A2.6) and Eq. (A2.8) into Eq. (2.71) and changing the order of integration over Ω yield:

$$(G_{scat})_m(z,\tau)=\frac{ik}{4\beta\pi}\exp(i\beta kz)\sum_{l=1}^{L} A_l\int_0^{z_0}\exp\left[\,i(\beta_0-\beta)k\xi-\left(\frac{\xi-\xi_l}{S_l}\right)^2\right]d\xi\,. \tag{A2.9}$$

$$\cdot \int_0^{R_0} \exp\left[-\left(\frac{\rho-\rho_l}{S_l}\right)^2\right] \cdot \rho \cdot j_m(\rho,\tau) j_{m_0}(\rho,\tau_0) \cdot \int_{\eta_l-\pi}^{\eta_l+\pi} \exp\left[i(m_0-m)\eta - \frac{4}{\pi S_l^2}\rho\rho_l|\eta-\eta_l|\right] d\eta\, d\rho \cdot$$

The first and third integrals can be computed analytically:

$$\left(G_{scat}\right)_m(z,\tau) = \frac{k\sqrt{\pi}}{i\beta}\exp(i\beta kz)\cdot\sum_{l=1}^{L}\rho_l A_l S_l \exp\left[-\frac{1}{4}k^2 S_l^2(\beta_0-\beta)^2 + i(\beta_0-\beta)k\xi_l\right]\cdot$$

$$\cdot\Phi\left[\frac{\xi_l - z_0}{S_l} + \frac{1}{2}ikS_l(\beta_0-\beta), \frac{\xi_l}{S_l} + \frac{1}{2}ikS_l(\beta_0-\beta)\right]\cdot\exp\left[i(m_0-m)\eta_l\right]\cdot$$

(A2.10)

$$\cdot\int_0^{R_0}\rho^2\cdot j_m(\rho,\tau)j_{m_0}(\rho,\tau_0)\cdot\exp\left[-\left(\frac{\rho-\rho_l}{S_l}\right)^2\right]\cdot\frac{1-\exp\left[-\frac{4\rho\rho_l}{S_l^2}-i\pi(m+m_0)\right]}{\left[\pi S_l(m_0-m)\right]^2+\left[\frac{4\rho\rho_l}{S_l}\right]^2}d\rho\,,$$

where $\Phi(a,b)$ is the error function:

(A2.11) $$\Phi(a,b) = \frac{2}{\sqrt{\pi}}\int_a^b e^{-t^2}\,dt\,.$$

The remaining one-dimensional integral over $[0,\, R_0)$ has to be computed numerically.

Using Eq. (A2.10) it is easy to compute numerically the scattered field Eq. (2.73) for a given illumination angle α. As it turned out to be highly dependent on the location and size of the waveguide's perturbations, the results had to be averaged for several randomly drawn perturbations. For the numerical computations the following perturbation properties were assumed:

- Only the waveguide's core is perturbed, so $R_0 = R$ in Eq. (A2.10).
- The perturbation centre (ρ_l, η_l, ξ_l) is uniformly distributed within the core.
- The perturbation amplitude $A_l \sim N(0, A)$ (was modelled with a Gaussian random variable with mean 0 and standard deviation A). As Eq. (A2.10) depends linearly on the perturbation amplitude, its exact value does not matter, and all numerical computations were made with the constant value $A = 0.01$.
- The perturbation size (i.e. its e^{-1} radius) $S_l \sim S\chi_1$ (was modelled with a random variable of chi-square distribution with one degree of freedom and mean S).

The perturbed fragment of the waveguide was assumed to have the length $z_0 = 10\,R$. The computations were made for the following combinations of parameters:

- The $V = 8$ waveguide:
  - L=1, S=0.05R,
  - L=1, S=0.25R,
- The $V = 20$ waveguide:
  - L=1, S=0.05R,
  - L=1, S=0.25R.

In each case 800 (for the $V = 8$ waveguide) or 400 (for the $V = 20$ waveguide) computations were made and averaged to obtain the average scattering matrix $[rsp(m_0, k_0; m, k)]$ (see Eq. (2.72) and Eq. (2.73)). *Fig. A2.16* shows in the logarithmical scale the angular distributions of the scattered power per solid angle for both waveguides, the scattering matrices obtained for the parameters L=1, S=0.25R and the same input angles as on *Fig. A2.14*.

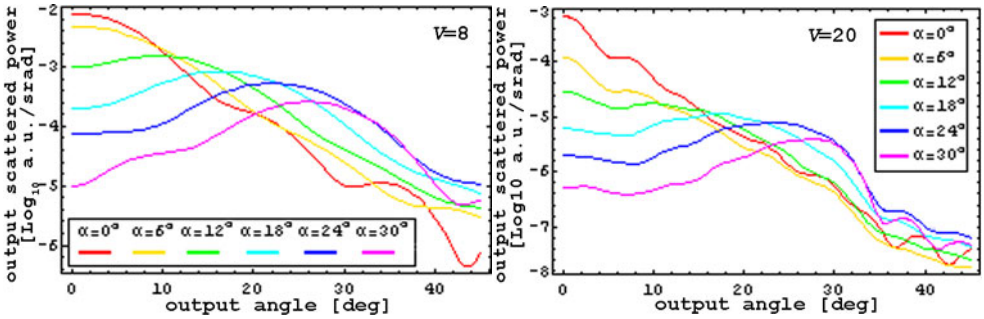

Fig. A2.16 *Angular distribution of the output power of the scattered field in both waveguides, (number of perturbations L=1, mean size of the perturbation S=0.25R).*

Using the obtained scattering matrices and Eq. (2.46), Eq. (2.47) the *t*otal *s*cattered *p*ower in dependence on the illumination angle α for both waveguides and all investigated perturbation types can be easily computed:

(A2.12) $$tsp(\alpha) := \sum_{m_0 \in Z} \sum_{k_0=0}^{P_m} p_{m_0}^{(0)}\left(\alpha; m_0, \tau_{k_0}^{m_0}\right) \sum_{m \in Z} \sum_{k=0}^{P_m} rsp(m_0, k_0; m, k)$$

and after normalisation to 1 at the illumination angle 0° plotted as *Fig. A2.17*:

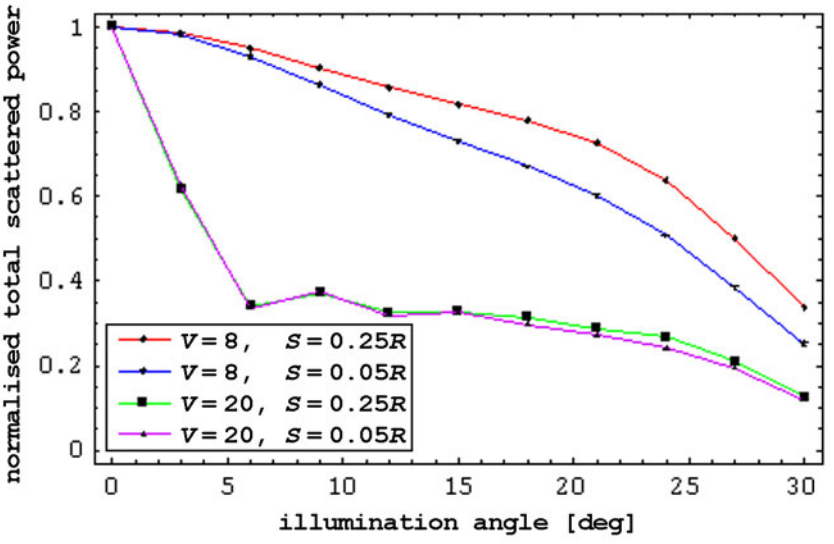

Fig. A2.17 *Normalised total scattered power in dependence on the illumination angle.*

Fig. A2.17 shows an evident negative correlation between the illumination angle and the total scattered power and is used in Part 2.2.2 to construct the formulae for the angle-dependent scattering model within the raytracing approach.

A3 Sample measured and simulated FFP graphs

In this appendix the sample graphs of the measured and simulated (optimised) FFPs of *set0* (non-aged fibres) and *set5* (the most aged fibres: 4467 h at 100 °C / <<50 % RH) are shown for comparison. Note the difference of the fit quality between the non-aged (*set0*) and highly aged (*set5*) samples. According to the target function Eq. (3.1), the optimisation procedure described in Part 3.2.3.3 matches two-dimensional FFPs and thus it weights the one-dimensional FFPs with the sine of the illumination angle α. Therefore, in the following graphs, the higher α, the better the fit quality. The FFP notation is explained in Part 6.2.

A3.1 ESKA CK-40 fibre

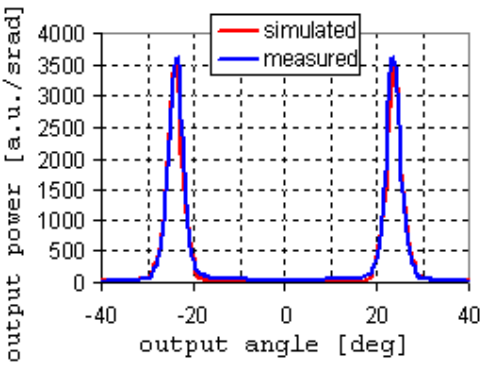

Fig. A3.1 *Measured and simulated* M-set0-1-24.

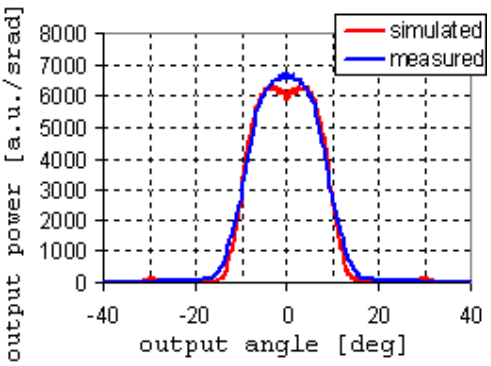

Fig. A3.2 *Measured and simulated* M-set0-2-06.

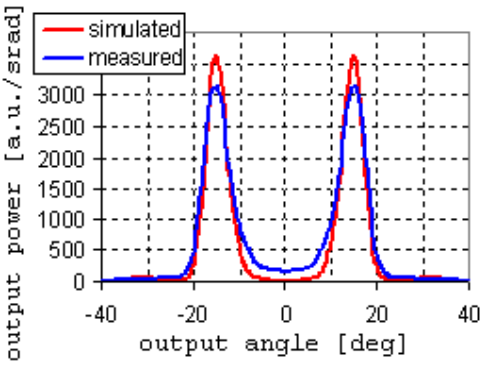

Fig. A3.3 *Measured and simulated* M-set0-2-15.

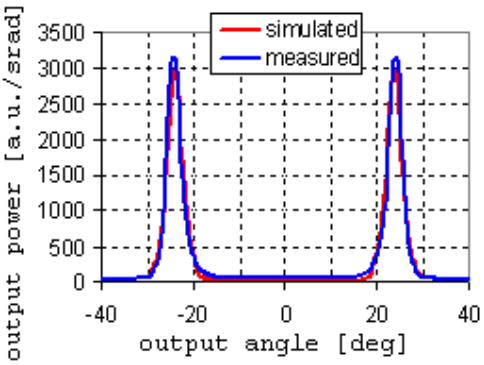

Fig. A3.4 *Measured and simulated* M-set0-2-24.

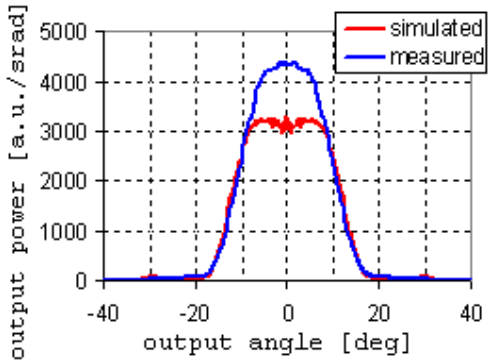

Fig. A3.5 *Measured and simulated* M-set0-3-06.

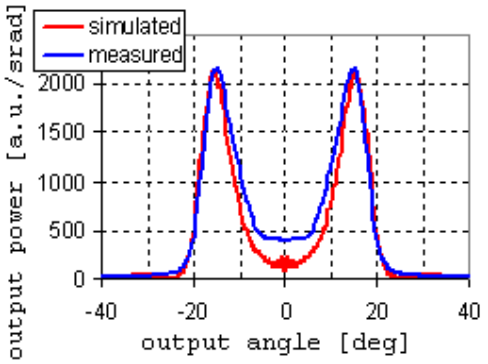

Fig. A3.6 *Measured and simulated* M-set0-3-15.

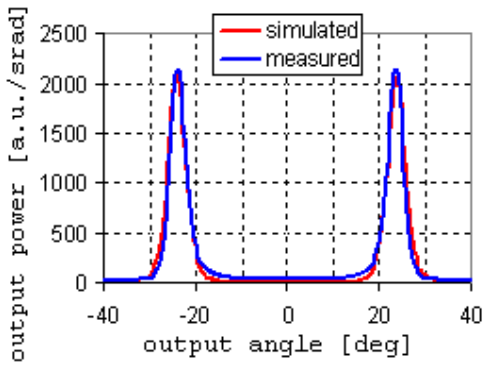

Fig. A3.7 *Measured and simulated* M-set0-3-24.

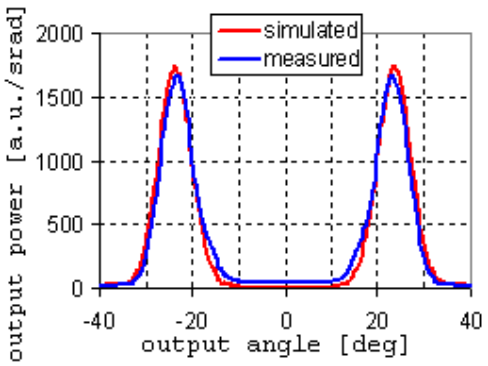

Fig. A3.8 *Measured and simulated* M-set5-1-24.

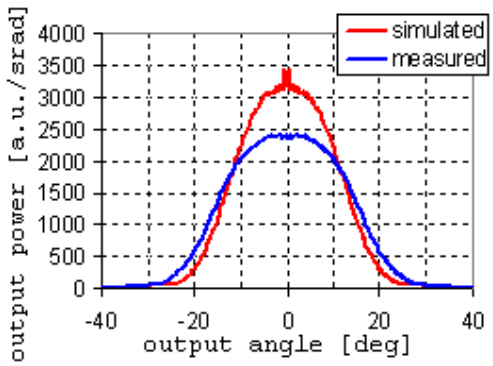

Fig. A3.9 *Measured and simulated* M-set5-2-06.

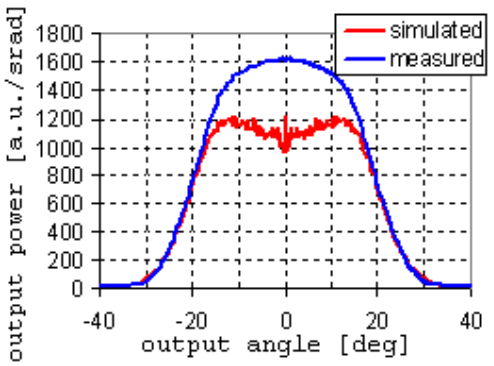

Fig. A3.10 *Measured and simulated* M-set5-2-15.

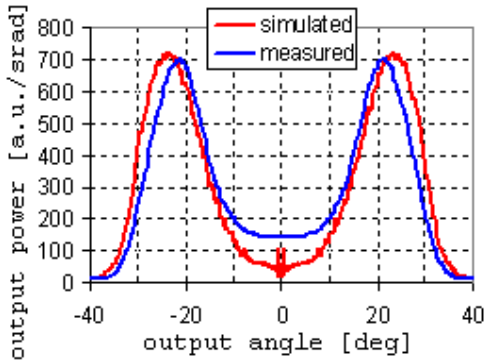

Fig. A3.11 *Measured and simulated* M-set5-2-24.

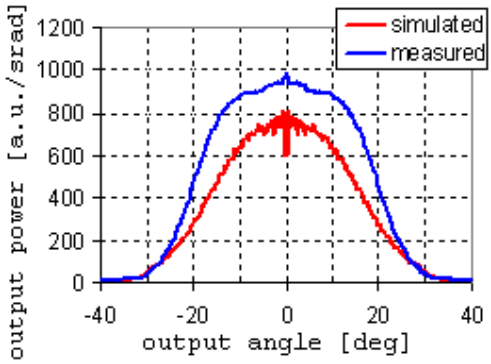

Fig. A3.12 *Measured and simulated* M-set5-3-06.

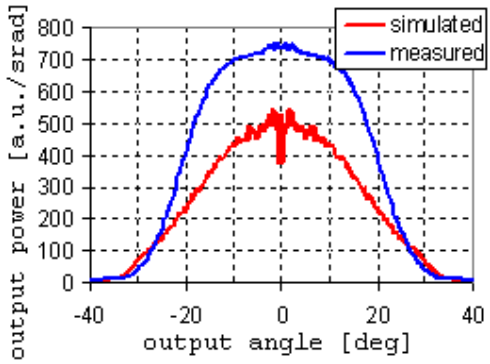

Fig. A3.13 *Measured and simulated* M-set5-3-15.

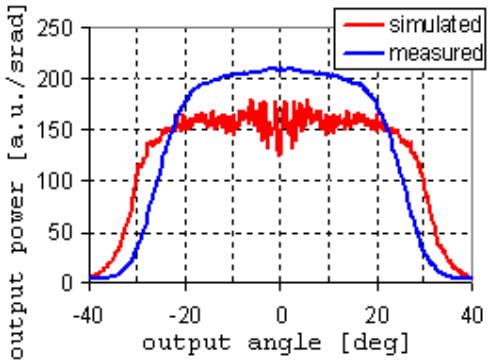

Fig. A3.14 *Measured and simulated* M-set5-1-24.

A3.2 PGU FB-1000 fibre

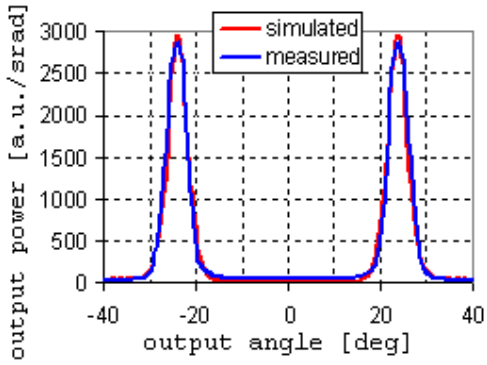

Fig. A3.15 *Measured and simulated* T-set0-1-24.

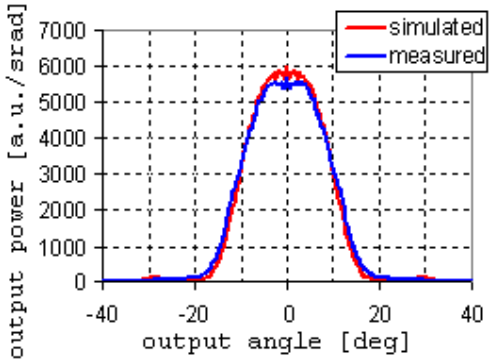

Fig. A3.16 *Measured and simulated* T-set0-2-06.

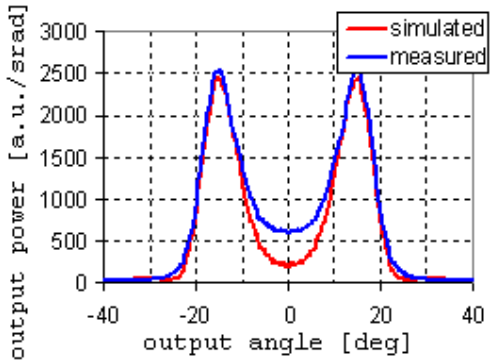

Fig. A3.17 *Measured and simulated* T-set0-2-15.

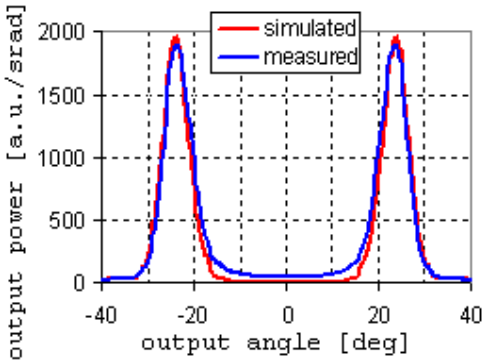

Fig. A3.18 *Measured and simulated* T-set0-2-24.

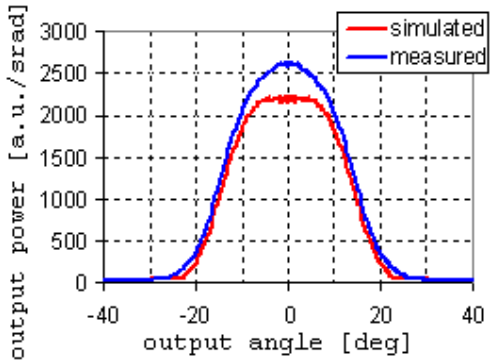

Fig. A3.19 *Measured and simulated* T-set0-3-06.

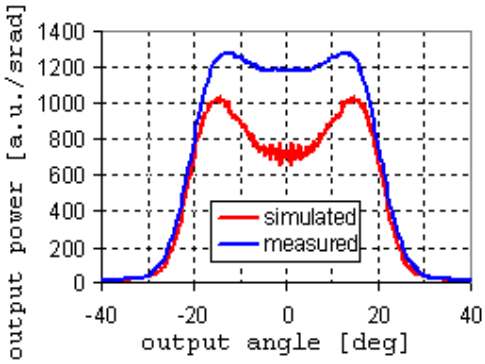

Fig. A3.20 *Measured and simulated* T-set0-3-15.

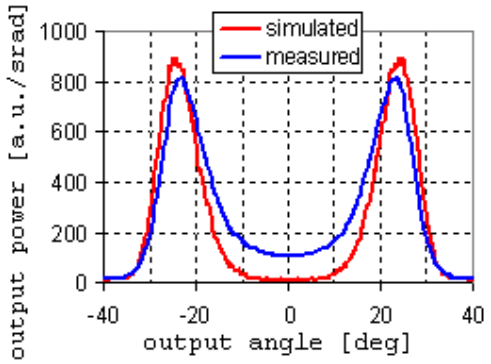

Fig. A3.21 *Measured and simulated* T-set0-3-24.

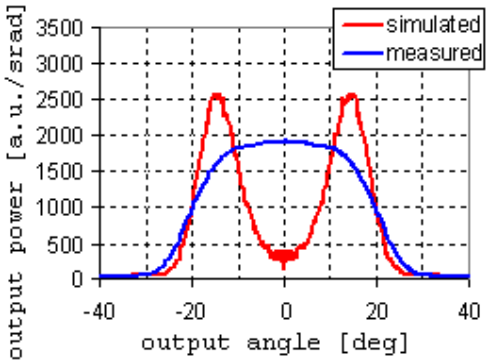

Fig. A3.22 *Measured and simulated* T-set5-1-15.

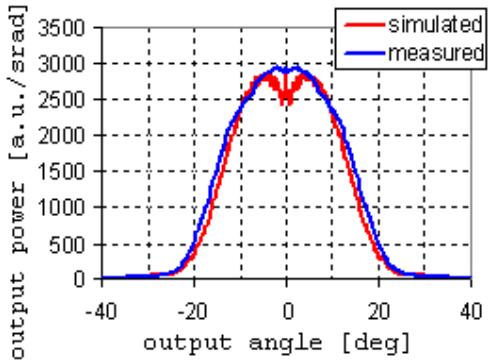

Fig. A3.23 *Measured and simulated* T-set5-2-06.

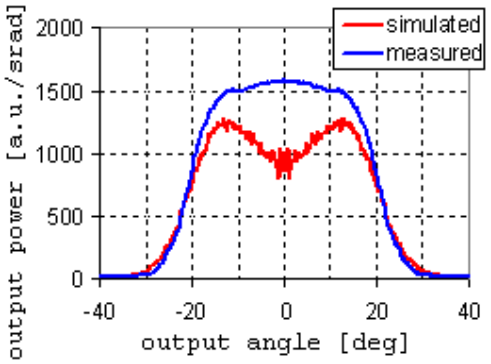

Fig. A3.24 *Measured and simulated* T-set5-2-15.

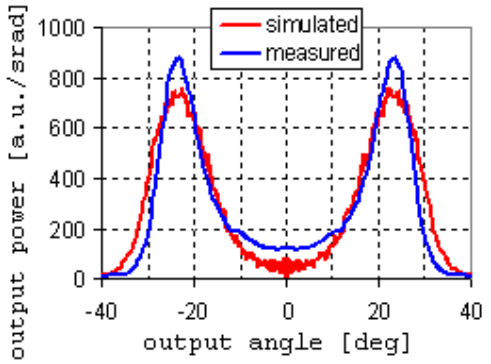

Fig. A3.25 *Measured and simulated* T-set5-2-24.

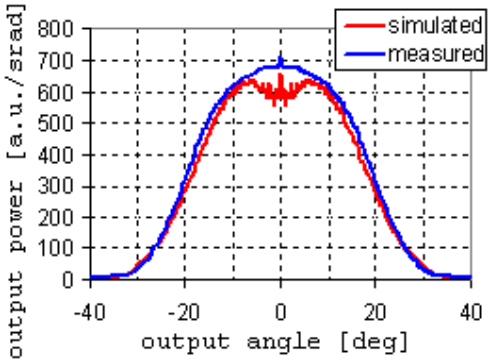

Fig. A3.26 *Measured and simulated* T-set5-3-06.

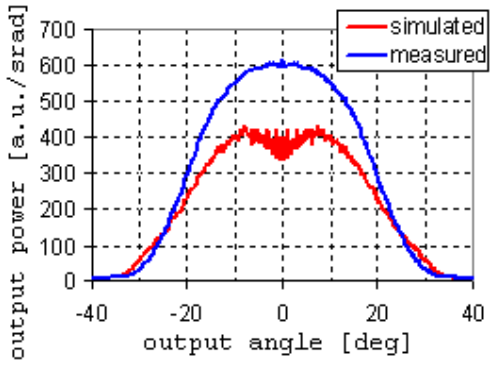

Fig. A3.27 *Measured and simulated* T-set5-3-15.

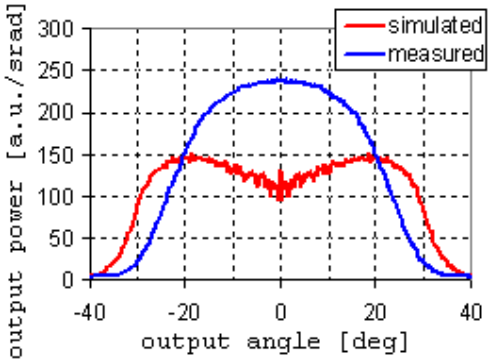

Fig. A3.28 *Measured and simulated* T-set5-3-24.

A3.3 LUMINOUS TB-1000 fibre

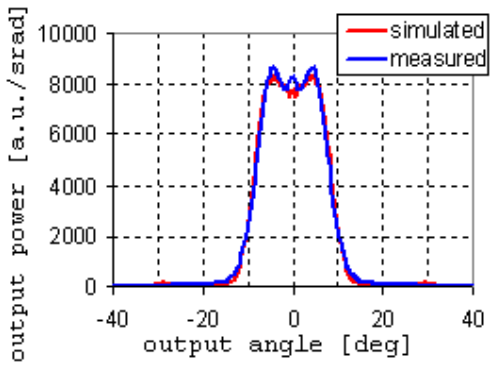

Fig. A3.29 *Measured and simulated* A-set0-2-06.

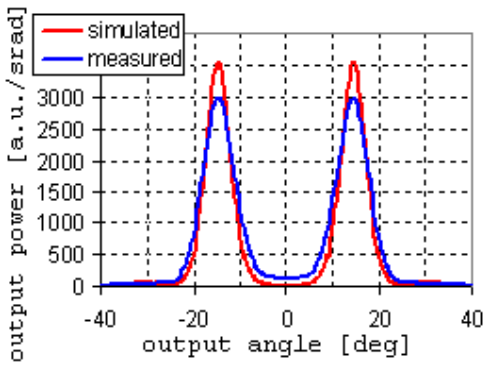

Fig. A3.30 *Measured and simulated* A-set0-2-15.

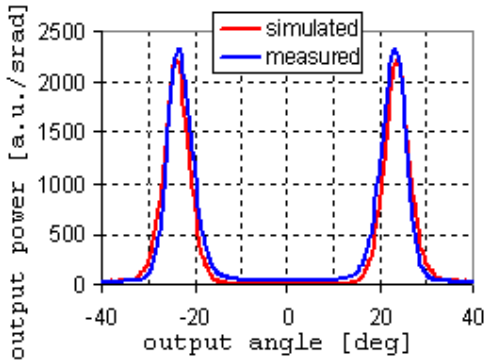

Fig. A3.31 *Measured and simulated* A-set0-2-24.

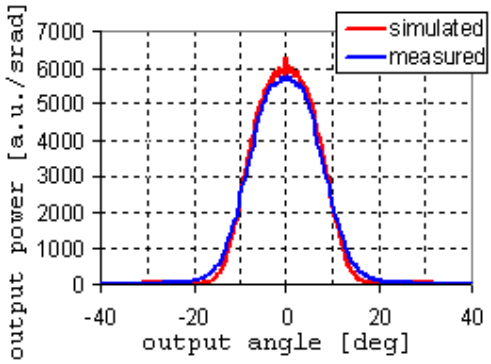

Fig. A3.32 *Measured and simulated* A-set0-3-06.

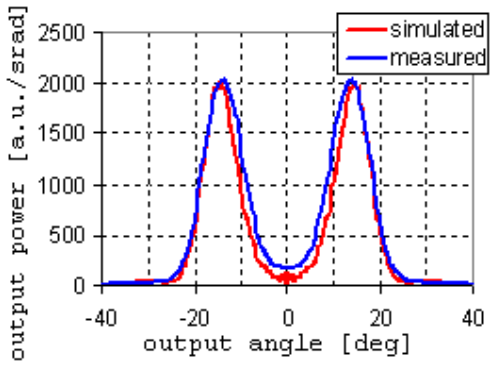

Fig. A3.33 *Measured and simulated* A-set0-3-15.

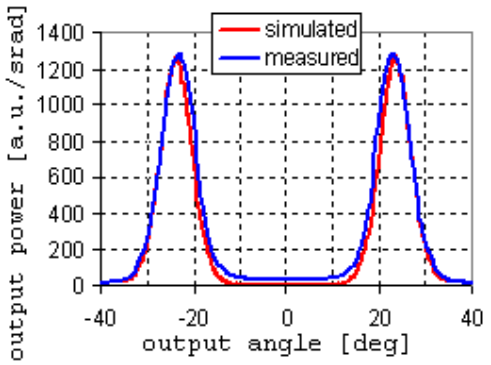

Fig. A3.34 *Measured and simulated* A-set0-3-24.

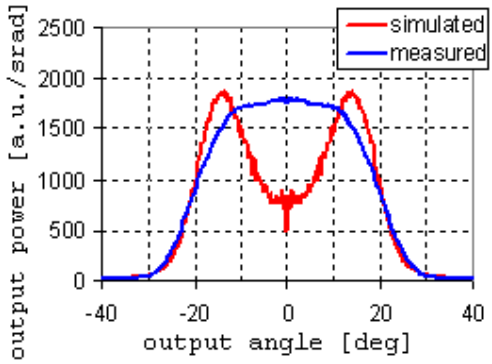

Fig. A3.35 *Measured and simulated* A-set5-1-15.

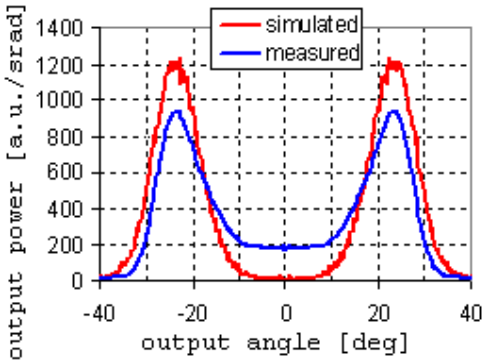

Fig. A3.36 *Measured and simulated* A-set5-1-24.

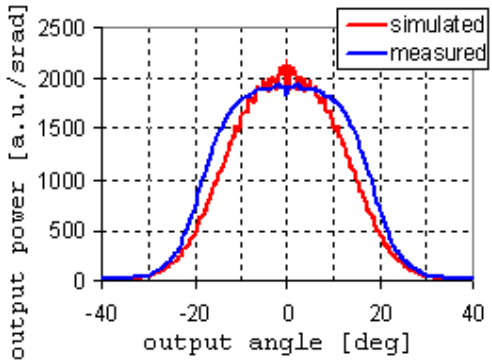

Fig. A3.37 *Measured and simulated* A-set5-2-06.

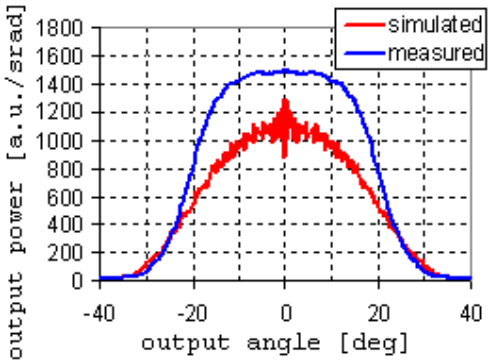

Fig. A3.38 *Measured and simulated* A-set5-2-15.

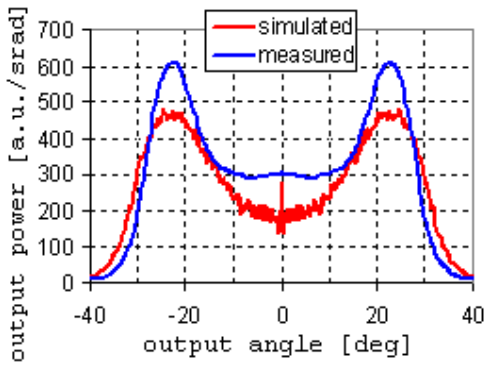

Fig. A3.39 *Measured and simulated* A-set5-2-24.

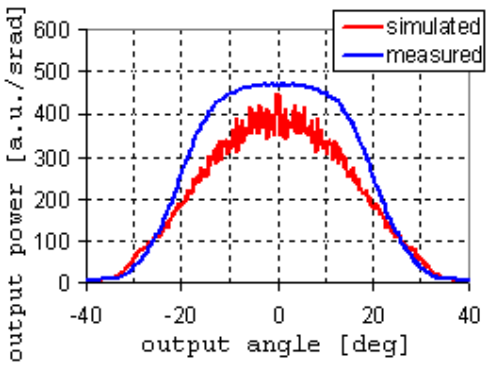

Fig. A3.40 *Measured and simulated* A-set5-3-06.

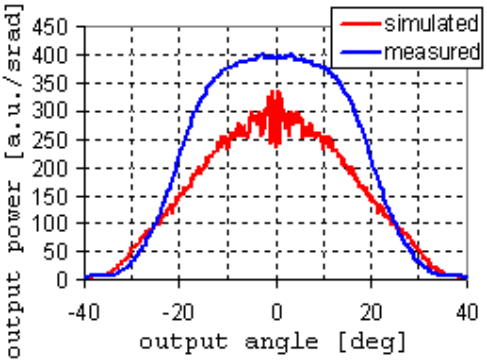

Fig. A3.41 *Measured and simulated* A-set5-3-15.

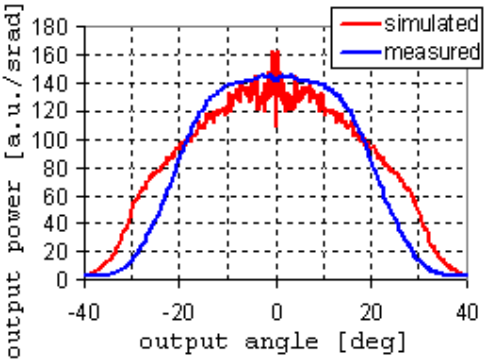

Fig. A3.42 *Measured and simulated* A-set5-3-24.

A4 Convergence of the von Neumann series

This appendix contains some considerations concerning the convergence of the von Neumann series Eq. (2.64) in the supremum norm. If brought to the end, the existence and continuity the series would be proved and the scattered field u_{scat} Eq. (2.64) would be under Hypothesis 1 the solution of the Helmholtz equation Eq. (2.57).

Due to Eq. (2.66)

$$|T(r,\varphi,z)| \le k^2 D_{\max} U_{\max} \int_{\Omega} |g(r,\varphi,z;\rho,\eta,\xi)|\, dV(\rho,\eta,\xi)\,, \tag{A4.1}$$

where

$$\begin{aligned} D_{\max} &= \sup d(r,\varphi,z), \\ U_{\max} &= \sup u(r,\varphi,z). \end{aligned} \tag{A4.2}$$

To prove the convergence of Eq. (2.64) in the supremum norm it would be enough to prove that $||T||$ is bounded (by a constant independent of r, φ, z), because then the perturbation size D_{max} could be always chosen small enough to make Eq. (A4.1) less than 1 and hence Eq. (2.64) converge.

Using Eq. (2.63)

$$\begin{aligned} &\int_{\Omega} |g(r,\varphi,z;\rho,\eta,\xi)|\, dV(\rho,\eta,\xi) \le \\ &\le \frac{1}{4\pi^2 k} \sum_{m\in\mathbf{Z}} \int_0^{z_0} \int_0^{2\pi R_0} \int_{-\infty}^{\infty} \frac{1}{|\beta|} \left| e^{i|z-\xi|k\beta} \right| \cdot |\rho \cdot j_m(r,\tau) j_m(\rho,\tau)|\, d\chi_m(\tau)\, d\rho\, d\eta\, d\xi\,, \end{aligned} \tag{A4.3}$$

where due to the representation of $d\chi_m(\tau)$ of Theorem 2.3 and Eq. (A1.6) the most inner integral can be majorised as follows:

$$\int_{-\infty}^{\infty}\frac{1}{|\beta|}\left|e^{i|z-\xi|k\beta}\right|\cdot\left|\rho\cdot j_m(r,\tau)j_m(\rho,\tau)\right|d\chi_m(\tau)=$$

$$=\sum_{k=0}^{P_m} r_k^m\,\frac{1}{\left|\beta_k^m\right|}\cdot\left|e^{i|z-\xi|k\beta}\right|\cdot\rho\cdot\left|j_m\left(r,\tau_k^m\right)\right|\cdot\left|j_m\left(\rho,\tau_k^m\right)\right|$$

$$+\frac{1}{2}\pi k^2\int_{-\infty}^{n_1^2}\frac{1}{|\beta|}\cdot\left|e^{i|z-\xi|k\beta}\right|\cdot\rho\cdot\frac{|j_m(r,\tau)|\cdot|j_m(\rho,\tau)|}{a_m^2(\tau)+b_m^2(\tau)}d\tau\le \tag{A4.4}$$

$$\le\rho\sum_{k=0}^{P_m}\frac{r_k^m}{\left|\beta_k^m\right|}+\frac{1}{4}\pi k^2\int_{-\infty}^{n_1^2}\frac{1}{|\beta|}\cdot\left|e^{i|z-\xi|k\beta}\right|\cdot\rho\cdot\frac{|j_m(r,\tau)|^2+|j_m(\rho,\tau)|^2}{a_m^2(\tau)+b_m^2(\tau)}d\tau\,.$$

Applying Eq. (A4.4) to Eq. (A4.3) and splitting the range of the integration with respect to τ:

$$\int_\Omega|g(r,\varphi,z;\rho,\eta,\xi)|\,dV(\rho,\eta,\xi)\;\le\;\frac{1}{4\pi}\frac{z_0R_0^2}{k}\sum_{m\in\mathbf{Z}}\sum_{k=0}^{P_m}\frac{r_k^m}{\left|\beta_k^m\right|}+$$

$$+\frac{k}{16\pi}\int_0^{z_0}\int_0^{2\pi}\int_0^{R_0}\int_{-\infty}^{n_1^2}\frac{\rho}{|\beta|}\cdot\left|e^{i|z-\xi|k\beta}\right|\cdot\sum_{m\in\mathbf{Z}}\frac{|j_m(r,\tau)|^2+|j_m(\rho,\tau)|^2}{a_m^2(\tau)+b_m^2(\tau)}\,d\tau\,d\rho\,d\eta\,d\xi\le$$

$$\le\frac{1}{4\pi}\frac{z_0R_0^2}{k}\sum_{m\in\mathbf{Z}}\sum_{k=0}^{P_m}\frac{r_k^m}{\left|\beta_k^m\right|}+\frac{1}{8}k\int_0^{z_0}\int_0^{R_0}\int_{-\infty}^{0}\frac{\rho}{|\beta|}e^{-|z-\xi|k|\beta|}\left[C(r,\tau)+C(\rho,\tau)\right]d\tau\,d\rho\,d\xi\;+$$

$$+\frac{1}{8}z_0k\int_0^{R_0}\int_0^{n_1^2}\frac{\rho}{|\beta|}\left[C(r,\tau)+C(\rho,\tau)\right]d\tau\,d\rho= \tag{A4.5}$$

$$=\frac{1}{4\pi}\frac{z_0R_0^2}{k}\sum_{m\in\mathbf{Z}}\sum_{k=0}^{P_m}\frac{r_k^m}{\left|\beta_k^m\right|}+\frac{1}{16}kR_0^2\int_0^{z_0}\int_{-\infty}^{0}\frac{e^{-|z-\xi|k|\beta|}}{|\beta|}C(r,\tau)\,d\tau\,d\xi+$$

$$+\frac{1}{8}k\int_0^{z_0}\int_0^{R_0}\rho\int_{-\infty}^{0}\frac{e^{-|z-\xi|k|\beta|}}{|\beta|}C(\rho,\tau)\,d\tau\,d\rho\,d\xi+$$

$$+\frac{1}{16}z_0kR_0^2\int_0^{n_1^2}\frac{C(r,\tau)}{|\beta|}\,d\tau+\frac{1}{8}z_0k\int_0^{R_0}\rho\int_0^{n_1^2}\frac{C(\rho,\tau)}{|\beta|}\,d\tau\,d\rho\,,$$

where

$$C(r,\tau):=\sum_{m\in\mathbf{Z}}\frac{|j_m(r,\tau)|^2}{a_m^2(\tau)+b_m^2(\tau)}\,. \tag{A4.6}$$

First summand in Eq. (A4.5) is finite, because there are only finitely many guided modes (Theorem 2.1). Therefore, T would be bounded and Eq. (2.64) would converge, if the other summands in Eq. (A4.5) were finite and bounded by constants independent of r and z. Thus

if the function $C(r,\tau)$ was not increasing too strong as $\tau \to n_1^2$, and was decreasing enough quick as $\tau \to -\infty$, so that both integrals

(A4.7) $$\int_0^{n_1^2} \frac{C(r,\tau)}{|\beta|}\, d\tau, \qquad \int_0^{z_0}\int_{-\infty}^{0} \frac{e^{-|z-\xi|k|\beta|}}{|\beta|} C(r,\tau)\, d\tau\, d\xi,$$

could not only converge, but also be bounded by a constant independent of r and z (note that the same would hold then for the other two integrals of Eq. (A4.5), too). The following parts of this appendix contain considerations potentially helpful in proving it. First, two auxiliary facts have to be formulated:

(A4.8) If $z \neq 0$ and $J_m(z) = 0$,
then $J'_m(z) = J_{m-1}(z) = -J_{m+1}(z) \neq 0$
and $J_{m-2}(z) \neq 0$, $J_{m-1}(z) \neq 0$, $J_{m+1}(z) \neq 0$ and $J_{m+2}(z) \neq 0$.

(A4.9) If $J_m(wR) = 0$ and $\tau < n_1^2$, then
$$J_m(w_0 R) = \frac{Rw_1^2}{w_0 + w} J_{m-1}(wR) + O(w_1^4) = \frac{-Rw_1^2}{w_0 + w} J_{m+1}(wR) + O(w_1^4) = O(w_1^2)$$
as $\tau \to n_1^2$ (which implies $w_0 \to w > 0$ and $w_1 \to 0$), where w_0 and w_1 are defined in Eq. (2.19) and depend on τ and w.

Eq. (A4.8) follows directly from Eq. (A1.6), Eq. (A1.7), Eq. (A1.8), the recurrence relation Eq. (A1.7) and Eq. (A1.12). If noted that due to Eq. (2.19)

$$w_0 - w = \frac{w_0^2 - w^2}{w_0 + w} = \frac{w_1^2}{w_0 + w},$$

then the expansion of J_m in power series around the point wR yields Eq. (A4.9):

$$J_m(w_0 R) = J_m(wR) + R(w_0 - w) J'_m(wR) + O\left((w_0 - w)^2\right) =$$

$$= \frac{Rw_1^2}{w_0 + w} J_{m-1}(wR) + O(w_1^4) = -\frac{Rw_1^2}{w_0 + w} J_{m+1}(wR) + O(w_1^4) = O(w_1^2).$$

A4.1 Coefficient $a_m(\tau)$

Coefficient $a_m(\tau)$ is defined in Eq. (2.28) as:

(A4.10) $$a_m(\tau) = \frac{1}{2}\pi R\left[w_0 J_{m+1}(w_0 R) Y_m(w_1 R) - w_1 J_m(w_0 R) Y_{m+1}(w_1 R)\right].$$

Functions w, w_0 and w_1 are defined in Eq. (2.19).

LEMMA A4.1

(1) $a_{-m}(\tau) = a_m(\tau)$.

(2) For each $m \in \mathbf{Z}$ $a_m(\tau) \to 1$ as $\tau \to -\infty$.

(3) As $\tau \to n_1^2$

(c) (*m=0*) If $J_1(wR)=0$, then $a_0(\tau) \to J_0(wR) \neq 0$ else $a_0(\tau) \to \pm\infty$.

(d) (*|m|=1*) If $J_0(wR)=0$, then $a_1(\tau) = O(w_1 \ln w_1) \to 0$, else $a_1(\tau) \to \pm\infty$.

(e) (*|m|=2*) If $J_1(wR)=0$, then $a_2(\tau) \to 2J_0(wR) \neq 0$, else $a_2(\tau) \to \pm\infty$.

For all other $|m| \in \mathbf{Z} \setminus \{0,1,2\}$ $a_m(\tau) \to \pm\infty$.

PROOF:

Proof of (1)

Follows by direct substitution of Eq. (A1.4), Eq. (A1.7) in the definition Eq. (A4.10) of $a_m(\tau)$. Thus while proving *(2)* and *(3)* it is enough to consider $m \in \mathbf{N}$ only.

Proof of (2)

Eq. (A1.2) implies that

$$\lim_{\tau \to -\infty} Y_m(z) = 0 \cdot$$

According to Eq. (2.19) $\tau \to -\infty$ implies $w_0, w_1 \to \infty$, thus

$$\lim_{\tau \to -\infty} (w_0 - w_1) = \lim_{\tau \to -\infty} \frac{w_0^2 - w_1^2}{w_0 + w_1} = \lim_{\tau \to -\infty} \frac{w^2}{w_0 + w_1} = 0$$

and

$$\lim_{\tau \to -\infty} \frac{w_0}{w_1} = \lim_{\tau \to -\infty} \frac{w_0 - w_1}{w_1} + 1 = 1.$$

Using asymptotic expansions Eq. (A1.2):

$$Rw_0 J_m(w_0 R)\left[Y_n(w_1 R) - Y_n(w_0 R)\right] \cong$$

$$\cong \frac{2}{\pi} Rw_0 (w_0 R)^{-\frac{1}{2}} \cos(w_0 R - \vartheta_m)\left[(w_1 R)^{-\frac{1}{2}} \sin(w_1 R - \vartheta_n) - (w_0 R)^{-\frac{1}{2}} \cos(w_0 R - \vartheta_n)\right] =$$

$$= \frac{2}{\pi} \cos(w_0 R - \vartheta_m)\left[\left(\frac{w_0}{w_1}\right)^{-\frac{1}{2}} \sin(w_1 R - \vartheta_n) - \sin(w_0 R - \vartheta_n)\right] =$$

$$= \frac{2}{\pi} \cos(w_0 R - \vartheta_m)\left[\left(\frac{w_0}{w_1}\right)^{-\frac{1}{2}} \left[\sin(w_1 R - \vartheta_n) - \sin(w_0 R - \vartheta_n)\right] + \right.$$

$$\left. + \left[\left(\frac{w_0}{w_1}\right)^{-\frac{1}{2}} - 1\right] \sin(w_0 R - \vartheta_n)\right] =$$

$$= \frac{2}{\pi}\cos(w_0 R - \vartheta_m)\left[\left(\frac{w_0}{w_1}\right)^{-\frac{1}{2}} 2\cos\left(\frac{R}{2}(w_0 + w_1) - \vartheta_n\right)\sin\left(\frac{R}{2}(w_1 - w_0)\right) + \right.$$

$$\left. + \left[\left(\frac{w_0}{w_1}\right)^{-\frac{1}{2}} - 1\right]\sin(w_0 R - \vartheta_n)\right] \underset{\tau\to\infty}{\to} 0$$

where $m,n \in \mathbf{N}$ and, for notational clarity, $\vartheta_k = -\frac{1}{2}k\pi - \frac{1}{4}\pi$. Finally, using Eq. (A1.1):

$$a_m(\tau) - 1 = \frac{1}{2}\pi R\left[w_0 J_{m+1}(w_0 R)Y_m(w_1 R) - w_1 J_m(w_0 R)Y_{m+1}(w_1 R)\right] +$$

$$-\frac{1}{2}\pi w_0 R\left[J_{m+1}(w_0 R)Y_m(w_0 R) - J_m(w_0 R)Y_{m+1}(w_0 R)\right] =$$

$$= \frac{1}{2}\pi R\left[R w_0 J_{m+1}(w_0 R)\left[Y_m(w_1 R) - Y_m(w_0 R)\right] + \right.$$

$$+ (w_0 - w_1)J_m(w_0 R)Y_{m+1}(w_1 R) +$$

$$\left. - R w_0 J_m(w_0 R)\left[Y_{m+1}(w_1 R) - Y_{m+1}(w_0 R)\right]\right] \underset{\tau\to-\infty}{\to} 0.$$

Proof of (3):

The Bessel functions $Y_m(w_1 R)$ and $Y_{m+1}(w_1 R)$ in the definition Eq. (A4.10) of $a_m(\tau)$ will be expanded to their power series Eq. (A1.9). Note that $\tau \to n_1^2$ implies $w_0 \to w > 0$ and $w_1 \to 0$. Thus the positive powers of z (i.e. of $w_1 R$ here) in Eq. (A1.9) can be substituted with $O(z)$ as $\tau \to n_1^2$. Therefore, the following forms will be used here:

$$Y_0(z) = \frac{2}{\pi}\left[J_0(z)\ln\frac{z}{2} - \psi(1) + O(z)\right],$$

$$Y_m(z) = \frac{2}{\pi}\left[J_m(z)\ln\frac{z}{2} - \frac{1}{2}\sum_{k=0}^{m-1}\frac{(m-k-1)!}{k!}\left(\frac{z}{2}\right)^{2k-m} + O(z)\right] \text{ for } |m|>0.$$

Two cases have to be considered:

- For m=0:

$$a_0(\tau) = \left[R w_0 J_1(w_0 R)J_0(w_1 R) - R w_1 J_0(w_0 R)J_1(w_1 R)\right]\ln\frac{w_1 R}{2} +$$

$$+ O(w_1)\left[R w_0 J_1(w_0 R) - R w_1 J_0(w_0 R)\right] + J_0(w_0 R) - \psi(1) R w_0 J_1(w_0 R).$$

There are two possible subcases:

- $J_1(wR)\neq 0$. Then $a_0(\tau)\cong C_1\ln(w_1R/2)+C_2\to\pm\infty$ as $\tau\to n_1^2$ for certain constants $C_1\neq 0$ and C_2.
- $J_1(wR)=0$. Then, according to Lemma A4.1,

$$J_1(w_0R)=O\left(w_1^2\right) \text{ as } \tau\to n_1^2 .$$

Thus, using Eq. (A1.11),

$$a_0(\tau)=\left[Rw_0J_0(w_1R)-J_0(w_0R)\right]\ln\frac{w_1R}{2}O\left(w_1^2\right)+O\left(w_1^2\right)+$$
$$+O\left(w_1^2\right)+J_0(w_0R)+O\left(w_1^2\right)\to J_0(w_0R)\neq 0 \text{ as } \tau\to n_1^2$$

and *(3a)* has been proved.

- For $m>0$, using the limiting forms of Eq. (A1.11):

$$a_m(\tau)=\left[Rw_0J_{m+1}(w_0R)J_m(w_1R)-Rw_1J_m(w_0R)J_{m+1}(w_1R)\right]\ln\frac{w_1R}{2}+$$
$$+O(w_1)\left[Rw_0J_{m+1}(w_0R)-Rw_1J_m(w_0R)\right]+$$
$$+\frac{1}{2}Rw_1J_m(w_0R)\sum_{k=0}^{m}\frac{(m-k)!}{k!}\left(\frac{w_1R}{2}\right)^{2k-m-1}+$$
$$-\frac{1}{2}Rw_0J_{m+1}(w_0R)\sum_{k=0}^{m-1}\frac{(m-k-1)!}{k!}\left(\frac{w_1R}{2}\right)^{2k-m}=$$
$$=\left[J_{m+1}(w_0R)O\left(w_1^m\right)-J_m(w_0R)O\left(w_1^{m+2}\right)\right]\ln\frac{w_1R}{2}+$$
$$+O(w_1)\left[Rw_0J_{m+1}(w_0R)-Rw_1J_m(w_0R)\right]+\frac{1}{m!}J_m(w_0R)\left(\frac{w_1R}{2}\right)^m+$$
$$+\sum_{k=0}^{m-1}\frac{(m-k-1)!}{k!}\left(\frac{w_1R}{2}\right)^{2k-m}\left[(m-k)J_m(w_0R)-\frac{1}{2}Rw_0J_{m+1}(w_0R)\right]$$

as $\tau\to n_1^2$. Estimating further and using the recurrence relation Eq. (A1.7) one can obtain

(A4.11)

$$a_m(\tau)=\left[J_{m+1}(w_0R)-J_m(w_0R)O\left(w_1^2\right)\right]\ln\frac{w_1R}{2}O\left(w_1^m\right)+$$
$$+O(w_1)\left[Rw_0J_{m+1}(w_0R)-Rw_1J_m(w_0R)\right]+J_m(w_0R)O\left(w_1^m\right)+$$
$$+\sum_{k=0}^{m-1}\frac{(m-k-1)!}{k!}\left(\frac{w_1R}{2}\right)^{2k-m}\left[\frac{1}{2}Rw_0J_{m-1}(w_0R)-kJ_m(w_0R)\right]$$

as $\tau \to n_1^2$. Consider even m and odd m separately:

- (*odd* m) Let $m{:=}2n{+}1$, $n{\in}\mathbf{N}$ ($n{\geq}0$). Substituting the positive powers of w_1R with $O(w_1)$ in the series Eq. (A4.11):

$$a_{2n+1}(\tau) = \left[J_{2n+2}(w_0R) - J_{2n+1}(w_0R)O\left(w_1^2\right)\right]\ln\frac{w_1R}{2}O\left(w_1^{2n+1}\right) +$$

$$+ O(w_1)\left[Rw_0J_{2n+2}(w_0R) - Rw_1J_{2n+1}(w_0R)\right] + J_{2n+1}(w_0R)O\left(w_1^{2n+1}\right) +$$

$$+ \sum_{k=0}^{n}\frac{(2n-k)!}{k!}\left(\frac{w_1R}{2}\right)^{2k-2n-1}\left[\frac{1}{2}Rw_0J_{2n}(w_0R) - kJ_{2n+1}(w_0R)\right] + O(w_1)$$

as $\tau \to n_1^2$. Assume that there exists a finite limit of $a_{2n+1}(\tau)$ as $\tau \to n_1^2$. Then all coefficients in the square brackets of the power series, as corresponding to the negative powers of w_1, have to be $O\left(w_1^{-2k+2n+1}\right)$ as $\tau \to n_1^2$, which implies they have to equal zero for $\tau = n_1^2$ ($w_0 = w$), i.e.:

$$RwJ_{2n}(wR) = 0 \text{ (for } k = 0\text{) and}$$

$$RwJ_{2n}(wR) - 2kJ_{2n+1}(wR) = 0 \text{ (for } k = 1, \ldots, n \text{ and } n \geq 1\text{).}$$

The first condition can hold only if $J_{2n}(wR) = 0$. For all $n \geq 1$ the second condition would have to hold, too. But then it would imply $J_{2n+1}(wR) = J_{2n}(wR) = 0$, a contradiction to Eq. (A4.8). Thus, if $n \geq 1$, then $a_{2n+1}(\tau) \to \pm\infty$ as $\tau \to n_1^2$. Therefore, a finite limit of $a_{2n+1}(\tau)$ as $\tau \to n_1^2$ is potentially possible only for $n = 0$, i.e. $m = 1$ and $J_{2n}(wR) = J_0(wR) = 0$. In this case, due to Eq. (A4.9),

$$J_{2n}(w_0R) = J_0(w_0R) = O\left(w_1^2\right) \text{ as } \tau \to n_1^2.$$

Substituting it into the formula for $a_{2n+1}(\tau) = a_1(\tau)$:

$$a_{2n+1}(\tau) = a_1(\tau) = \left[J_2(w_0R) - J_1(w_0R)O\left(w_1^2\right)\right]\ln\frac{w_1R}{2}O(w_1) +$$

$$+ O(w_1)\left[Rw_0J_2(w_0R) - Rw_1J_1(w_0R)\right] + J_1(w_0R)O(w_1) + O(w_1)$$

as $\tau \to n_1^2$. Due to Eq. (A4.8) $J_2(wR) \neq 0$. Hence, if $J_0(wR) = 0$, then

$$a_1(\tau) = O(w_1 \ln w_1) \to 0 \text{ as } \tau \to n_1^2.$$

In all other cases $a_{2n+1}(\tau) \to \pm\infty$ as $\tau \to n_1^2$ and *(3b)* has been proved.

- (*even* m) Let $m{:=}2n$, $n{\in}\mathbf{N}_+$ ($n{\geq}1$). Substituting the positive powers of w_1R with $O(w_1)$ in the series Eq. (A4.11):

$$a_{2n}(\tau) = \left[J_{2n+1}(w_0R) - J_{2n}(w_0R)O\left(w_1^2\right)\right]\ln\frac{w_1R}{2}O\left(w_1^{2n}\right) +$$

$$+ O(w_1)\left[Rw_0J_{2n+1}(w_0R) - Rw_1J_{2n}(w_0R)\right] + J_{2n}(w_0R)O\left(w_1^{2n}\right) +$$

$$+\sum_{k=0}^{n-1}\frac{(2n-k-1)!}{k!}\left(\frac{w_1R}{2}\right)^{2k-2n}\left[\frac{1}{2}Rw_0J_{2n-1}(w_0R)-kJ_{2n}(w_0R)\right]+$$

$$+\frac{1}{2n}Rw_0J_{2n-1}(w_0R)-J_{2n}(w_0R)+O(w_1^2)$$

as $\tau \to n_1^2$. Assume again that there exists a finite limit of $a_{2n}(\tau)$ as $\tau \to n_1^2$. Then, as in the previous case of odd m, all coefficients in the square brackets of the power series, as corresponding to the negative powers of w_1, have to be $O\left(w_1^{-2k+2n}\right)$ as $\tau \to n_1^2$, which implies that they all have to be equal to zero for $\tau = n_1^2$ ($w_0 = w$), i.e.:

$$RwJ_{2n-1}(wR)=0 \text{ (for } k=0\text{) and}$$

$$RwJ_{2n-1}(wR)-2kJ_{2n}(wR)=0 \text{ (for } k=1,\ \ldots,\ n\text{-}1 \text{ and } n>1\text{).}$$

The first condition can hold only if $J_{2n\text{-}1}(wR) = 0$. For all $n > 1$ the second condition would have to hold, too. But then it would imply $J_{2n\text{-}1}(wR) = J_{2n}(wR) = 0$, a contradiction to Eq. (A4.8). Thus, if $n > 1$, then $a_{2n}(\tau) \to \pm\infty$ as $\tau \to n_1^2$. Therefore, a finite limit of $a_{2n}(\tau)$ as $\tau \to n_1^2$ is potentially possible only for $n = 1$, $m = 2$ and $J_{2n\text{-}1}(wR) = J_1(wR) = 0$. In this case, due to Eq. (A4.9),

$$J_{2n-1}(w_0R)=J_1(w_0R)=-\frac{Rw_1^2}{w+w_0}J_2(wR)+O(w_1^4)=O(w_1^2)$$

as $\tau \to n_1^2$. Substituting it into the formula for $a_{2n}(\tau) = a_2(\tau)$:

$$a_{2n}(\tau)=a_2(\tau)=\left[J_3(w_0R)-J_2(w_0R)O(w_1^2)\right]\ln\frac{w_1R}{2}O(w_1^2)+$$

$$+O(w_1)\left[Rw_0J_3(w_0R)-Rw_1J_2(w_0R)\right]+J_2(w_0R)O(w_1^2)+$$

$$+\left(\frac{w_1R}{2}\right)^{-2}\frac{1}{2}Rw_0\left[-\frac{Rw_1^2}{w+w_0}J_2(wR)+O(w_1^4)\right]+$$

$$+O(w_1^2)-J_2(w_0R)+O(w_1^2)$$

as $\tau \to n_1^2$. Due to Eq. (A4.8) $J_2(wR) = -J_0(wR) \neq 0$ and $J_3(wR) \neq 0$. Hence, if $J_1(wR) = 0$, then

$$a_2(\tau)=-\frac{2w_0}{w+w_0}J_2(wR)-J_2(wR)+O(w_1)\to -2J_2(wR)=2J_0(wR)$$

as $\tau \to n_1^2$. In all other cases $a_{2n}(\tau) \to \pm\infty$ as $\tau \to n_1^2$ and *(3c)* has been proved.

Combining the results for even and odd m proves *(3d)*. ■

A4.2 Coefficient $b_m(\tau)$

Coefficient $b_m(\tau)$ is defined in Eq. (2.28) as:

(A4.12) $$b_m(\tau)=\frac{1}{2}R\pi\left[w_1 J_{m+1}(w_1R)J_m(w_0R)-w_0 J_m(w_1R)J_{m+1}(w_0R)\right].$$

Functions w, w_0 and w_1 are defined in Eq. (2.19).

LEMMA A4.2.

(1) $b_{-m}(\tau)=b_m(\tau)$.

(2) For each $m\in\mathbf{Z}$ $b_m(\tau)\to 0$ as $\tau\to-\infty$.

(3) As $\tau\to n_1^2$

(c) ($m=0$) If $J_1(wR)=0$, then $b_0(\tau)=O\left(w_1^2\right)\to 0$ else $b_0(\tau)\to-\pi wRJ_1(wR)/2$.

(d) ($|m|>0$) If $J_{m+1}(wR)=0$, then $b_m(\tau)=O\left(w_1^{m+2}\right)\to 0$,

(e) else $b_m(\tau)=O\left(w_1^m\right)\to 0$.

(4) For each $\tau\in\left(-\infty,n_1^2\right]$ $b_m(\tau)\to 0$ as $|m|\to\infty$.

PROOF:

Proof of (1)

Follows by direct substitution of Eq. (A1.4), Eq. (A1.7) in the definition Eq. (A4.12) of $b_m(\tau)$. Thus while proving *(2)*, *(3)* and *(4)* it is enough to consider $m\in\mathbf{N}$ only.

Proof of (2)

$$b_m(\tau)=\frac{1}{2}R\pi\left[w_1 J_{m+1}(w_1R)J_m(w_0R)-w_0 J_m(w_1R)J_{m+1}(w_0R)\right]=$$

$$=\frac{1}{2}R\pi w_1\left[J_{m+1}(w_1R)J_m(w_0R)-J_m(w_1R)J_{m+1}(w_0R)\right]+$$

$$+\frac{1}{2}R\pi(w_1-w_0)J_m(w_1R)J_{m+1}(w_0R)$$

The second term clearly converges to zero as $\tau\to-\infty$ (see Eq. (A1.2) and the proof of Lemma A4.1(2)). Thus considering the limiting value the second term can be dropped. Further estimating and using asymptotic expansions Eq. (A1.2):

$$b_m(\tau)\cong\frac{1}{2}R\pi w_1\left[J_{m+1}(w_1R)J_m(w_0R)-J_m(w_1R)J_{m+1}(w_0R)\right]\cong$$

$$\cong\left(\frac{w_1}{w_0}\right)^{\frac{1}{2}}\left[\cos\left(w_1R-\frac{m+1}{2}\pi-\frac{\pi}{4}\right)\cos\left(w_0R-\frac{m}{2}\pi-\frac{\pi}{4}\right)+\right.$$

$$\left.-\cos\left(w_1R-\frac{m}{2}\pi-\frac{\pi}{4}\right)\cos\left(w_0R-\frac{m+1}{2}\pi-\frac{\pi}{4}\right)\right]=$$

$$= \left(\frac{w_1}{w_0}\right)^{\frac{1}{2}} \left[\sin\left(w_1 R - \frac{m}{2}\pi - \frac{\pi}{4}\right)\cos\left(w_0 R - \frac{m}{2}\pi - \frac{\pi}{4}\right) + \right.$$

$$\left. - \cos\left(w_1 R - \frac{m}{2}\pi - \frac{\pi}{4}\right)\sin\left(w_0 R - \frac{m}{2}\pi - \frac{\pi}{4}\right)\right] =$$

$$= \frac{1}{2}\left(\frac{w_1}{w_0}\right)^{\frac{1}{2}} \left[\sin\left((w_0 + w_1)R - m\pi - \frac{\pi}{2}\right) - \sin((w_0 - w_1)R) + \right.$$

$$\left. - \sin\left((w_0 + w_1)R - m\pi - \frac{\pi}{2}\right) - \sin((w_0 - w_1)R)\right] =$$

$$= -\left(\frac{w_1}{w_0}\right)^{\frac{1}{2}} \sin((w_0 - w_1)R) \to 0$$

as $\tau \to -\infty$.

Proof of (3a):

Using Eq. (A1.11)

$$b_0(\tau) = \frac{1}{2} R\pi\left[w_1 O(w_1) J_0(w_0 R) - w_0 J_1(w_0 R)\left[1 + O\left(w_1^2\right)\right]\right]$$

If $J_1(wR) = 0$, then according to Eq. (A4.9)

$$J_1(w_0 R) = O\left(w_1^2\right) \text{ as } \tau \to n_1^2,$$

thus in this case

$$b_0(\tau) = \frac{1}{2} R\pi\left[O\left(w_1^2\right) - O\left(w_1^2\right)\left[1 + O\left(w_1^2\right)\right]\right] = O\left(w_1^2\right) \to 0 \text{ as } \tau \to n_1^2.$$

If $J_1(wR) \neq 0$, then simply

$$b_0(\tau) = \frac{1}{2} R\pi\left[O\left(w_1^2\right) J_0(w_0 R) - w_0 J_1(w_0 R)\left[1 + O\left(w_1^2\right)\right]\right] =$$

$$= -\frac{1}{2} R\pi w_0 J_1(w_0 R) + O\left(w_1^2\right) \to -\frac{1}{2} R\pi w J_1(wR) \text{ as } \tau \to n_1^2.$$

Proof of (3b):

Using Eq. (A1.11).

$$b_m(\tau) = \frac{1}{2} R\pi\left[w_1 J_m(w_0 R) O\left(w_1^{m+1}\right) - w_0 J_{m+1}(w_0 R) O\left(w_1^m\right)\right] =$$

$$= \frac{1}{2} R\pi\left[J_m(w_0 R) O\left(w_1^2\right) - w_0 J_{m+1}(w_0 R)\right] O\left(w_1^m\right) \text{ as } \tau \to n_1^2.$$

Hence if $J_{m+1}(wR) \neq 0$, then

$$b_m(\tau) = O\left(w_1^m\right) \to 0 \text{ as } \tau \to n_1^2.$$

If $J_{m+1}(wR) = 0$, then according to Eq. (A4.9)

$$J_{m+1}(w_0 R) = O\left(w_1^2\right) \text{ as } \tau \to n_1^2,$$

and in this case

$$b_m(\tau) = O\left(w_1^{m+2}\right) \to 0 \text{ as } \tau \to n_1^2.$$

Proof of (4):

Follows directly from Eq. (A1.15). ■

A4.3 Term $a_m^2(\tau) + b_m^2(\tau)$

Respective parts of Lemma A4.1 and Lemma A4.2 can be combined to obtain:

LEMMA A4.3.

(1) $a_{-m}^2(\tau) + b_{-m}^2(\tau) = a_m^2(\tau) + b_m^2(\tau)$.

(2) For each $m \in Z$ $a_m^2(\tau) + b_m^2(\tau) \to 1$ as $\tau \to -\infty$.

(3) As $\tau \to n_1^2$

(c) ($|m|=0$) If $J_1(wR)=0$, then $a_0^2(\tau) + b_0^2(\tau) \to J_0^2(wR) \neq 0$, else $a_0^2(\tau) + b_0^2(\tau) \to \infty$.

(d) ($|m|=1$) If $J_0(wR)=0$, then $a_1^2(\tau) + b_1^2(\tau) = O\left(w_1^2 \ln^2 w_1\right) \to 0$, else $a_1^2(\tau) + b_1^2(\tau) \to \infty$.

(e) ($|m|=2$) If $J_1(wR)=0$, then $a_2^2(\tau) + b_2^2(\tau) \to 4J_0^2(wR) \neq 0$, else $a_2^2(\tau) + b_2^2(\tau) \to \infty$.

(f) In all other cases $a_m^2(\tau) + b_m^2(\tau) \to \infty$. ■

LEMMA A4.4 Let

$$\varepsilon_m := \inf_{\tau \in \left(-\infty, n_1^2\right)} \left[a_m^2(\tau) + b_m^2(\tau)\right]$$

Then

(1) $\varepsilon_m \geq 0$

(2) $\varepsilon_m = 0$ iff $|m|=1$ and $J_0(wR)=0$.

Proof:

Part *(1)* is obvious from the definition of ε_m. The proof of *(2)* will be given in three steps:

Step 1: $a_m^2(\tau) + b_m^2(\tau) > 0$ for each $m \in \mathbf{Z}$ and $\tau \in \left(-\infty, n_1^2\right)$.

Proof of Step 1: Assume the opposite, i.e. that there exist such $m_0 \in \mathbf{Z}$ and $\tau_0 \in \left(-\infty, n_1^2\right)$ that $a_{m_0}^2(\tau_0) + b_{m_0}^2(\tau_0) = 0$. Then $a_{m_0}(\tau_0) = b_{m_0}(\tau_0) = 0$ and thus also each their linear combination:

$$0 = J_{m_0}(w_1 R) a_{m_0}(\tau_0) + Y_{m_0}(w_1 R) b_{m_0}(\tau_0) =$$

$$= \frac{1}{2} \pi R w_1 J_{m_0}(w_0 R) \left[J_{m_0+1}(w_1 R) Y_{m_0}(w_1 R) - J_{m_0}(w_1 R) Y_{m_0+1}(w_1 R) \right] =$$

$$= J_{m_0}(w_0 R),$$

due to Eq. (A1.1). In a similar way

$$0 = J_{m_0+1}(w_1 R) a_{m_0}(\tau_0) + Y_{m_0+1}(w_1 R) b_{m_0}(\tau_0) =$$

$$= \frac{1}{2} \pi R w_0 J_{m_0+1}(w_0 R) \left[J_{m_0+1}(w_1 R) Y_{m_0}(w_1 R) - J_{m_0}(w_1 R) Y_{m_0+1}(w_1 R) \right] =$$

$$= \frac{w_0}{w_1} J_{m_0+1}(w_0 R) \cdot$$

Therefore $J_{m_0}(w_0 R) = J_{m_0+1}(w_0 R) = 0$, a contradiction to Eq. (A4.8). Thus, $a_m^2(\tau) + b_m^2(\tau)$ is positive for each $m \in \mathbf{Z}$ and $\tau \in \left(-\infty, n_1^2\right)$.

Step 2: Implication "$\Leftarrow$" in *(2)* holds.

Proof of Step 2: Follows from Lemma A4.3*(3b)*.

Step 3: Implication "$\Rightarrow$" in *(2)* holds.

Proof of Step 3: Assume the opposite, i.e. that there exist $m_0 \in \mathbf{Z}$ and a sequence $\left\{\tau_k \middle| k \in \mathbf{N}\right\} \subset \left(-\infty, n_1^2\right)$ such that

$$a_{m_0}^2(\tau_k) + b_{m_0}^2(\tau_k) \to 0 \text{ as } k \to \infty$$

and ($|m_0| \neq 1$ or $J_0(wR) \neq 0$). Due to the Bolzano-Weierstrass lemma [27], there exists such a subsequence $\left\{\tau_{k_n} \middle| n \in \mathbf{N}\right\} \subseteq \left\{\tau_k\right\}$ that as $n \to \infty$ either:

$$\tau_{k_n} \to -\infty$$

or $\tau_{k_n} \to \tau'$ for a given finite $\tau' \in \left(-\infty, n_1^2\right)$

or $\tau_{k_n} \to n_1^2$.

First possibility contradicts Lemma A4.3*(2)*, the second contradicts *Step 1* of this lemma and the third (with the condition ($|m_0| \neq 1$ or $J_0(wR) \neq 0$)) contradicts Lemma A4.3*(3)*. ■

References

[1] A. W. Snyder, J. D. Love, *Optical Waveguide Theory*, Chapman and Hall, London New York 1983.

[2] O. Alexandrov, G. Ciraolo, *Wave propagation in a 3-D optical waveguide*, Mathematical Models and Methods in Applied Sciences (M3AS), Vol. 14(6), 2004, pp. 819-852.

[3] M. Abramowitz, I. Stegun, *Handbook of mathematical functions*, Dover Publications, New York, 1972.

[4] M. Born, E. Wolf, *Principles of optics*, Pergamon Press, 4th ed., 1970.

[5] D. Gloge, *Weakly guiding fibers*, Appl. Optics, Vol. 10, pp. 2252-2258, 1971.

[6] E. Snitzer, *Cylindrical dielectric waveguide modes*, J. of the Optical Society of America, Vol. 51, pp. 491 – 498, 1961.

[7] O. Alexandrov, G. Ciraolo, *Wave propagation in a 3-D optical waveguide II: numerical examples*, *http://www.math.umn.edu/~aoleg/research/coaxial.pdf*.

[8] R. Magnanini, F. Santosa, *Scattering in a 2-D optical waveguide*, in: *Analytical and Computational Methods in Scattering and Applied Mathematics*, ed. F. Santosa, I. Stakgold, CRC Press, London 1999.

[9] A. Sommerfeld, *Vorlesungen über Theoretische Physik*, *Band VI*: *Partielle Differentialgleichungen der Physik*, Verlag Harri Deutsch, Thun, Frankfurt/M., 1978.

[10] W. Daum, J. Krauser, P. E. Zamzow, O. Ziemann, *POF – Polymer Optical Fibers for Data Communication*, Springer, Berlin 2002.

[11] J. Arrue, J. Zubia, G. Durana, J. Mateo, M. Lopez-Amo, *Model for the propagation of pulses and mode scrambling in a real POF with structural imperfections*, Proceedings of the 10th International Conference on Plastic Optical Fibres, p. 301, Amsterdam 2001.

[12] The Wolfram Functions Site, *http://functions.wolfram.com*.

[13] A. D. Polyanin, A. V. Manzhirov, *Handbuch der Integralgleichungen*, Spektrum Akademischer Verlag; Heidelberg, Berlin 1999.

[14] L. Jankowski, *Calibration procedure for low-end CCD cameras*, Proceedings of the TEST-IC, Nuremberg 2003, pp. 255-260.

[15] L. Jankowski, A. Appajaiah, C.-A. Bunge, J. Zubia, *Modelling of Light Propagation Through Aged and Non-Aged POFs*, Proceedings of the 12th POF-IC, Seattle 2003.

[16] J. Zubia, H. Poisel, C.-A. Bunge, G. Aldabaldetreku, J. Arrue, *POF modelling*, Proceedings of the 11th POF-IC, Tokyo 2002, pp. 221-224.

[17] A. Appajaiah, L. Jankowski, *A review on aging or degradation of polymer optical fibres – Polymer chemistry and mathematical approach*, Proceedings of the 10th International Conference on Plastic Optical Fibres, pp. 317–324, Amsterdam 2001.

[18] B. Günther, W. Czepluch, K. Mäder, S. Zedler, *Multiplexer for Attenuation Measurements during POF Durability Testing*, Proceedings of the 9th International Conference on Plastic Optical Fibres, Boston 2000.

[19] B. Günther, W. Czepluch, W. Daum, K. Mäder, S. Zedler, *Multiplexer for Long Time Transmission Measurements of Plastic Optical Fibres (POF)*, Proceedings of the SENSOR/TEST-IC, Nuremberg 2001.

[20] G. Durana, J. Zubia, J. Arrue, M. Lomer, J. M. Lopez Higuera, *Cladding thickness dependence of bending losses*, Proceedings of the 10th International Conference on Plastic Optical Fibres, Amsterdam, 2001, pp. 117–120.

[21] Wolfram Research, Optica application package: *http://www.wolfram.com/products/applications/optica/*

[22] Optical Research Associates, CODE V: *http://www.opticalres.com/products_f.html#codev*

[23] Breault Research Organization, ASAP: *http://www.breault.com/html/soft_asap.html*

[24] Borland Software Corporation, Delphi: *http://www.borland.com/delphi/*

[25] F. Rellich, *Über das asymptotische Verhalten der Lösungen von Δu+λu=0 in unendlichen Gebieten*, Jahresber. Deutch. Math. Verein., Vol. 53, pp. 57-65, 1943.

[26] W. Daum, M. Scholl, *VDI/VDE Guidline 5570 – The First Comprehensive Standard on Characterisation and Testing of POF*, Proceedings of the 11th International Conference on Plastic Optical Fibres, pp. 243–246, Tokyo, 2002.

[27] G. Fichtenholz, *Differentialrechnung und Integralrechnung*, Verlag Harri Deutsch, 1997.

[28] K. Kawano, T. Kitoh, *Introduce to Optical Waveguide Analysis: Solving Maxwell's Equations and the Schrödinger Equation*, John Wiley & Sons, 2001.

[29] D. Marcuse, *Theory of dielectric optical waveguides*, Academic Press, 1974.

[30] N. S. Kapany, *Fiber Optics*, Academic Press, New York, 1967.

[31] C. Hahn, H. Poisel, H. Karl, *Modelling and Simulating Transmission Characteristics of Polymer Optical Fibres*, Proceedings of the 10th International Conference on Plastic Optical Fibres, pp. 113–116, Amsterdam 2001.

[32] W. Daum, M. Hein, O. Ziemann, *The new VDI/VDE guideline on testing plastic optical fibres*, Proceedings of the 10th International Conference on Plastic Optical Fibres, pp. 31-38, Amsterdam 2001.

[33] A. Appajaiah, H.-J. Kretzschmar, *Climatic aging or degradation of plastic optical fibers (POFs): Chemical analyses*, Proceedings of the 11th International Conference on Plastic Optical Fibres, Tokyo, 2002.

[34] A. Appajaiah, V. Wachtendorf, L. Jankowski, *Chemiluminescence investigation of high temperature and humidity aging of PMMA Based polymer optical fibres (POF)*, Proceedings of the 12th International Conference on Plastic Optical Fibres, Seattle 2003, pp. 152-155.

[35] A. Appajaiah, H.-J. Kretzschmar, *Climatic aging of PMMA based polymer optical fibers (POF): Analysis of polymer degradation*, 3rd International IEEE Conference on Polymers and Adhesives in Microelectronics and Photonics, Polytronic 2003, Montreux, Switzerland, 2003.

[36] A. Appajaiah, V. Wachtendorf, *Ageing behavior of polymer optical fibers: Characterization of thermo-oxidative stability by chemiluminescence*, to appear in: Proceedings of the 13th International Conference on Plastic Optical Fibres, Nuremberg, 2004.

[37] S2000 Miniature Spectrometer with a Sensitive CCD Detector, Sentronic, specification available at: *http://www.getspec.com/sentronic/Sentronic.NSF/main.html?open&id=S2000_EN*.

[38] K. Suzuki, T. Nakano, K. Shirakawa, Y. Yada, *Basic characteristic measurement of a POF*, Proceedings of the 11th International Conference on Plastic Optical Fibres, pp. 173–175, Tokyo, 2002.

[39] K.-F. Klein, A. Bachmann, M. Bloos, O. Ziemann, *Comparison of different far field measurement setups*, Proceedings of the 11th International Conference on Plastic Optical Fibres, pp. 259–262, Tokyo, 2002.

[40] B. Lohmüller, A. Bachmann, O. Ziemann, A. Sawaki, H. Shirai, K. Suzuki, *The use of LEPAS system for POF characterisation*, Proceedings of the 11th International Conference on Plastic Optical Fibres, pp. 263–266, Tokyo, 2002.

[41] R. Olshansky, *Mode coupling effects in graded-index optical fibers*, Appl. Optics, Vol. 14(4), 1975, pp. 935–945.

[42] D. Gloge, *Optical power flow in multimode fibers*, Bell Syst. Tech. J., Vol. 51, 1972, pp. 1767–1783.

[43] L. Jeunhomme, M. Fraise, J. P. Pocholle, *Propagation model for long step-index optical fibers*, Appl. Optics, Vol. 15(2), 1976, pp. 3040–3046.

[44] W. A. Gambling, D. N. Payne, H. Matsumura, *Mode conversion coefficients in optical fibres*, Appl. Optics, Vol. 14(7), 1975, pp. 1583-1542.

[45] G. Durana, J. Zubia, M. Lopez-Amo, J. Arrue, Coupling coefficients in step index multimode fibers, Proceedings of the 9th International Conference on Plastic Optical Fibres, pp. 184–186, Boston, 2000.

[46] G. Durana, J. Zubia, J. Arrue, G. Aldabaldetreku, M. A. Losada, M. Lomer, *New method to calculate mode conversion coefficients in multimode optical fibres*, Proceedings of the 11th International Conference on Plastic Optical Fibres, pp. 209–212, Tokyo, 2002.

[47] J. Dugas, G. Maurel, *Mode-coupling processes in polymethyl methacrylate-core optical fibers*, Appl. Optics, Vol. 31(24), 1992, pp. 5069-5079.

[48] O. Ziemann, W. Daum, A. Bräuer, J. Schlick, W. Frank, *Results of a German 6.000 hours accelerated aging test of PMMA POF and consequences for the practical use of POF*, Proceedings of the 9th International Conference on Plastic Optical Fibres, Boston, 2000, pp. 173–177.

[49] W. Frank, A. Bräuer, W. Daum, H. J. Tessmann, A. Weinert, O. Ziemann, *Polymer optical fibres in Germany: reliability test for use in premise wiring*, Proceedings of the 7th International Conference on Plastic Optical Fibres, Berlin, 1998, pp. 287–289.

[50] M. Sato, T. Ishigure, E. Nihei, Y. Koike, *Thermal and humidity resistant GI POF*, Proceedings of the 7th International Conference on Plastic Optical Fibres, Berlin, 1998, pp. 108–109.

[51] W. Daum, W. Hammer, K. Mäder, *Spectral transmittance of polymer optical fibres before and after accelerated aging*, Proceedings of the 6th International Conference on Plastic Optical Fibres, Hawaii, 1997, pp. 14–15.

[52] J. Marcou, G. Boutinaud, P. Faugeras, K. Etorneau, G. Roblin, G. Roger, M. Dequenne, J. Dugas, P. Zimmermann, *Study of the POF behaviour under*

mechanical and thermal constraints, Proceedings of the 4th International Conference on Plastic Optical Fibres, Boston, 1995, pp. 105–110.

[53] W. Daum, A. Hoffman, U. Strecker, A. Brockmeyer, A. Weinert, *Influence of Chemicals on the Durability of Polymer Optical Fibres*, Proceedings of the 3rd International Conference on Plastic Optical Fibres, Yokohama, 1994, pp. 111–114.

[54] W. Daum, L. Goehlich, A. Brockmeyer, *Influence of environmental stress on transmission loss of polymer optical fibres*, Proceedings of the 2nd International Conference on Plastic Optical Fibres, The Hague, 1993, pp. 94–98.

[55] W. Daum, A. Brockmeyer, L. Goehlich, *Environmental qualification of polymer optical fibres for industrial applications*, Proceedings of the 1st International Conference on Plastic Optical Fibres, Paris, 1992, pp. 91–95.

[56] W. Daum, *Reliability Testing of Plastic Optical Fibres: State of the Art and Future Demands*, Proceedings of the 8th International Conference on Plastic Optical Fibres, Chiba, 1999,
pp. 14–17.

[57] C.-A. Bunge, C. Hahn, H. Poisel, O. Ziemann, K. Petermann, *Models of Transmission and Attenuation Characteristics of Step-Index Plastic Optical Fibres*, Proceedings of the 10th International Conference on Plastic Optical Fibres, Amsterdam, 2001, pp. 121–124.

[58] W. Baierl, *Evolution of Automotive Networks*, Proceedings of the 10th International Conference on Plastic Optical Fibres, Amsterdam, 2001, pp. 161–168.

[59] E. Zeeb, *Polymer based automotive data links*, Proceedings of the 10th International Conference on Plastic Optical Fibres, Amsterdam, 2001, pp. 169–176.

[60] M. A. Losada, I. Garcés, J. Mateo, I. Salinas, J. Zubia, *Mode coupling in plastic optical fibres of high and low numerical apertures*, Proceedings of the 10th International Conference on Plastic Optical Fibres, Amsterdam, 2001, pp. 109–112.

[61] C.-A. Bunge, O. Ziemann, J. Krauser, K. Petermann, *Effects of light propagation in step index polymer optical fibres*, Proceedings of the 8th International Conference on Plastic Optical Fibres, Chiba, 1999, pp. 136-139.

[62] D. Marcuse, *Coupled Mode Theory of Round Optical Fibres*, Bell Syst. Tech. J., Vol. 52, 1973, pp. 817-842.

[63] I. White, A. Snyder, *Radiation from dielectric optical waveguides: a comparison of techniques*, Appl. Optics, Vol. 16(6), 1977, pp. 1470-1472.

[64] A. Snyder, *Excitation and Scattering of Modes on a Dielectric or Optical Fiber*, IEEE Trans. Microwaves Theory Techn., Vol. 17(12), 1969, pp. 1138-1144.

[65] A. Snyder, *Radiation Losses Due to Variations of Radius on Dielectric or Optical Fibres*, IEEE Trans. Microwaves Theory Techn., Vol. 18(9), 1970, pp. 608-615.

[66] E. Rawson, *Analysis of Scattering from Fiber Waveguides with Irregular Core Surface*, Appl. Optics, Vol. 13(10), 1974, pp. 2370-2377.

[67] D. Marcuse, *Radiation losses of the HE_{11} mode of a fiber with sinusoidally perturbed core boundary*, Appl. Optics, Vol. 14(12), 1975, pp. 3021-3025.

[68] D. Gloge, *Bending Loss in Multimode Fibres with Graded and Ungraded Core Index*, Appl. Optics, Vol. 11(11), 1972, pp. 2506-2513.

[69] A. Snyder, D. Mitchell, *Bending losses of multimode optical fibres*, Electron. Lett., Vol. 10(1), 1974, pp. 11-12.

[70] R. Magnanini, F. Santosa, Wave propagation in a 2-D optical waveguide, SIAM J. Appl. Math., Vol. 61, 2000, pp. 1237-1252.